

---

# Study of a laser generated diamagnetic cavity and Alfvén waves in a large magnetized plasma

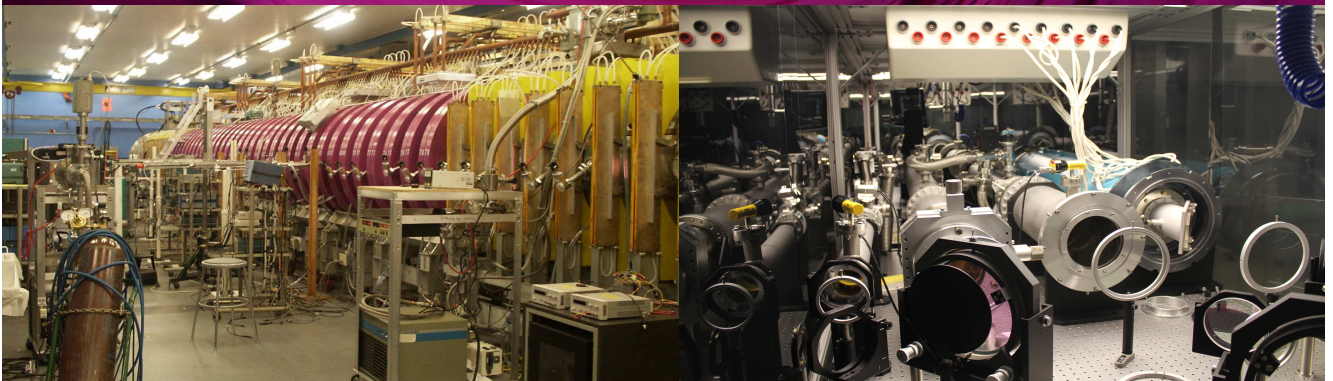
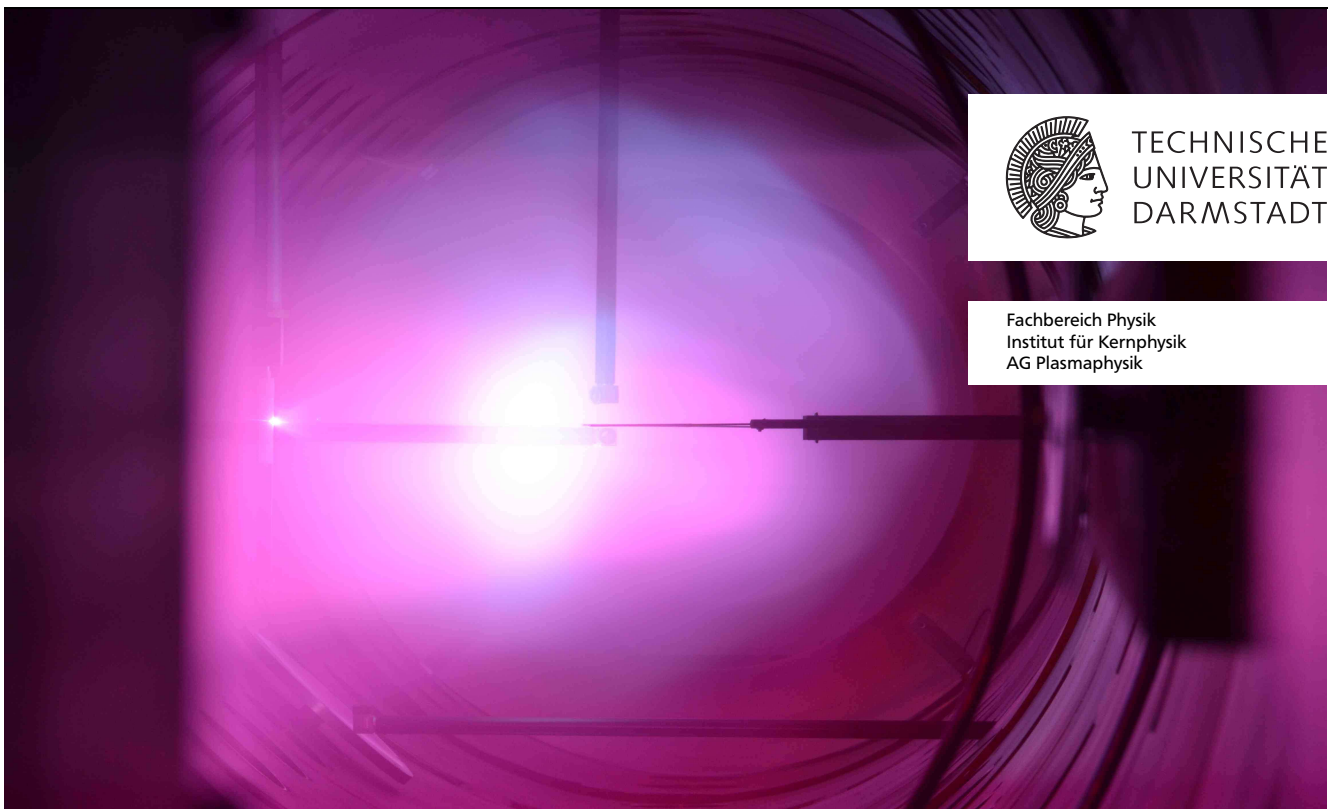
---

**Untersuchung eines laserproduzierten diamagnetischen Lochs und Alfvén-Wellen in einem großen magnetisierten Plasma**

Zur Erlangung des Grades eines Doktors der Naturwissenschaften (Dr. rer. nat.)

genehmigte Dissertation von Bo Ram Lee M.Sc. aus Seoul, Korea

Dezember 2015 — Darmstadt — D 17



Study of a laser generated diamagnetic cavity and Alfvén waves in a large magnetized plasma  
Untersuchung eines laserproduzierten diamagnetischen Lochs und Alfvén-Wellen in einem großen  
magnetisierten Plasma

Genehmigte Dissertation von Bo Ram Lee M.Sc. aus Seoul, Korea

1. Gutachten: Prof. Dr. Dr. h.c./RUS Dieter H.H. Hoffmann
2. Gutachten: Prof. Dr. Christoph Niemann

Tag der Einreichung: 14.10.2015

Tag der Prüfung: 16.12.2015

Darmstadt – D 17

---

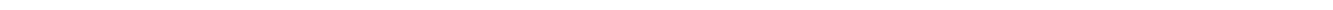
---

## Abstract

---

Dense plasma expansion into a tenuous magnetized background plasma is prevalent in space and astrophysical environments. In the interaction between plasmas with different densities under the influence of the magnetic field, various hydromagnetic waves are generated including the magnetized collisionless shocks which are believed to be the source of high energy particles, such as galactic cosmic rays from supernova remnants. Despite its importance in astrophysics and the study for longer than five decades, however, details of the shock physics, such as the formation process or the energy dissipation mechanisms are still not fully understood.

This work describes experiments carried out at the Large Plasma Device at University of California, Los Angeles, coupled to a kilojoule-laser. When a laser produced dense plasma interacts with a preformed, magnetized background plasma, a diamagnetic cavity is formed which can be pictured as a piston driving a collisionless shock. Understanding the micro-physics of generated diamagnetic cavities is crucial since it is observed in many magnetized plasmas with applied magnetic field and there are still a number of questions to be answered. In a series of experiments performed at different plasma parameters, magnetic flux probes and electron emissive probes are used to diagnose the structure of the diamagnetic cavity perpendicular to the magnetic field, especially at its edge where the collisionless coupling between the debris and ambient plasma takes place. In contrast to lower laser energy, a strong coupling to ambient ions could be observed depending on the background magnetic field although the energy conversion efficiency from the laser to the cavity stayed on the same order of magnitude. A rise of the radial electric field at the cavity edge was detected, which might be a direct evidence for the laminar coupling mechanism between debris and ambient plasmas without any collisional effects. Large fluctuations in the magnetic and electric field measurements in front of the cavity edge, which were also seen in the experimental observations, are assumed to be instabilities causing energy dissipation and the short cavity lifetime which is almost three orders of magnitude shorter than the theoretically derived classical diffusion time. Along the plasma column, soliton-like Alfvén waves were detected which might result from the nonlinear interaction between energetic electrons generated at the cavity edge and the surrounding magnetized plasma. Here, a better energy conversion efficiency from the laser to the Alfvén waves has been calculated. Finally, the experimental results are compared to two-dimensional hybrid simulations. The observed ion dynamics as well as large fluctuations in the electric field measurements at the cavity edge could be reproduced. An additional study was done on the effect of the polytropic coefficient in the electron temperature equation in the code and it showed that a nonadiabatic electron temperature increase affects the dynamics of the electric field as well as that of the diamagnetic cavity.





---

## Zusammenfassung

---

Die Expansion eines dichten Plasmas in ein magnetisiertes Plasma geringerer Dichte ist im Weltall und so auch im erdnahen Raum weit verbreitet. Bei der Wechselwirkung zwischen Plasmen unterschiedlicher Dichte im Magnetfeld werden verschiedene hydromagnetische Wellen erzeugt, z.B. die stoßfreien Stoßwellen, von denen man annimmt, dass sie die Quelle hochenergetischer Elektronen sind. Ein Beispiel hierfür ist die galaktische kosmische Strahlung von Supernovaüberresten. Trotz der Bedeutung für die Astrophysik und der bereits mehr als 50 Jahre andauernden Forschungstätigkeit ist die Physik von Stoßwellen heute aber immer noch nicht vollständig verstanden. So fehlen noch Erklärungen des eigentlichen Entstehungsprozesses der Stoßwellen und der Dissipation ihrer Energie.

Im Rahmen der vorliegenden Arbeit wird ein Experiment mit dem "Großen Plasmagerät" (Large Plasma Device - LAPD) an der University of California, Los Angeles, beschrieben, das an einen kJ-Laser gekoppelt ist. Wenn ein laserproduziertes dichtes Plasma mit einem vorgeformten, magnetisierten Plasma wechselwirkt, bildet sich ein diamagnetisches Loch, welches mit einem Kolben verglichen werden kann, der eine stoßfreie Stoßwelle generiert. Das Verständnis der Mikrophysik des entstandenen diamagnetischen Lochs ist sehr wesentlich, da derartige Löcher in vielen Plasmen beobachtet werden, die sich in einem Magnetfeld befinden, aber weiterhin bleiben viele Fragen unbeantwortet. In einer Serie von Experimenten werden bei unterschiedlichen Plasmaparametern Proben des Magnetfeldflusses und Elektronen emittierende Proben genommen, um die Struktur des diamagnetischen Lochs senkrecht zum Magnetfeld zu untersuchen, vor allem in der Randschicht, wo die stoßfreie Kopplung zwischen vom Target abgelösten Teilchen des Plasmas höherer Dichte und dem umgebenden Plasma niedriger Dichte stattfindet. Im Vergleich zu niedrigeren Laserenergiebereichen konnte ein besserer Energietransfer an das Hintergrundplasma beobachtet werden, welcher von der Stärke des angelegten Magnetfeldes abhängt. Dabei bleibt der Energieumwandlungswirkungsgrad vom Laser zum diamagnetischen Loch trotz der erhöhten Laserenergie in der gleichen Größenordnung. Der Anstieg des elektrischen Feldes an dem vorderen Rand von Stoßwellen wurde experimentell festgestellt, welcher ein direkter Beweis für den stoßfreien laminaren Kopplungsmechanismus zwischen dem laserproduzierten Plasma und den Umgebungsionen sein kann. Die vermessenen großen Fluktuationen der Magnetfelder und elektrischen Felder vor dem Rand, die auch durch schnelle Fotoaufnahmen beobachtet wurden, geben Hinweise auf die Anregung von Plasmastabilitäten, welche als Ursache sowohl für Energiedissipation als auch für die kurze Lebensdauer des diamagnetischen Lochs betrachtet wird. Dieser ist etwa drei Größenordnung kürzer als die theoretisch hergeleitete klassische Diffusionszeit. Entlang den Magnetfeldlinien wurden solitonen-ähnliche Alfvén-Wellen detektiert, welche aus der nichtlinearen Wechselwirkung zwischen energetischen Elektronen und dem umgebenden magnetisierten Plasma erzeugt werden können. Diese haben einen besseren Energieumwandlungswirkungsgrad im Vergleich zu den Alfvén-Wellen, die bei niedrigeren Laserenergien entstehen. Die experimentellen Ergebnisse der Arbeit werden mit zwei-dimensionalen Hybridsimulationen verglichen. Die im Experiment beobachtete Ionendynamik sowie große Fluktuationen in den Messungen von elektrischen Feldern konnten reproduziert werden. Weiterhin wurde auch der Einfluss des Polytropenkoefizienten auf die Lösung der mathematischen Gleichung für die Elektronentemperatur im Hybridcode erforscht. Dabei hatte ein nichtadiabatischer Anstieg der Elektronentemperatur zur

---

---

Folge, dass die elektrische Feldenergie zunahm und die Umgebungsionen in radialer Richtung schneller beschleunigt wurden.

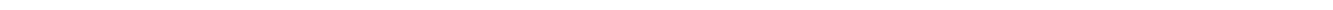
---

---

## Contents

---

<b>1</b>	<b>Introduction</b>	<b>1</b>
<b>2</b>	<b>Theory</b>	<b>5</b>
2.1	Laser-plasma interaction . . . . .	5
2.2	Coupling between debris-ambient plasmas . . . . .	6
2.3	Quasi-perpendicular shock formation . . . . .	10
2.4	Instabilities . . . . .	12
2.4.1	Micro-instabilities at the cavity edge . . . . .	13
2.4.2	Application of Energy Principle . . . . .	15
2.5	Generation of Alfvén waves . . . . .	18
<b>3</b>	<b>Experimental framework</b>	<b>21</b>
3.1	Large Plasma Device . . . . .	21
3.2	Phoenix Laser Facility . . . . .	22
3.3	Magnetic flux probe . . . . .	23
3.4	Electron emissive probe . . . . .	24
3.5	Fast photography . . . . .	25
3.6	Experimental setup . . . . .	26
<b>4</b>	<b>Experimental results</b>	<b>29</b>
4.1	Dynamics of the diamagnetic cavity . . . . .	29
4.1.1	Magnetic field measurements . . . . .	29
4.1.2	Electric field measurements . . . . .	39
4.1.3	Instabilities . . . . .	44
4.2	Excitation of shear Alfvén waves . . . . .	48
4.3	Summary . . . . .	55
<b>5</b>	<b>Two-dimensional hybrid simulation</b>	<b>59</b>
5.1	Effect of electron pressure $\gamma_e$ . . . . .	60
5.2	Simulation of the experiment . . . . .	65
5.3	Summary . . . . .	69
<b>6</b>	<b>Conclusions</b>	<b>71</b>
	<b>References</b>	<b>75</b>



---

## 1 Introduction

---

ITER (International Thermonuclear Experimental Reactor), a large reactor being built in South France [ITER, 2013], is one of the greatest scientific projects of mankind that has ever been initiated. Six countries are participating with the aim to produce energy yielded from the nuclear fusion reaction of two hydrogen isotopes, just like on the Sun, and part of the energy will be reused to activate another chemical reaction attaining the Q-value of 10, which is the ratio of fusion power produced in a nuclear fusion reactor to the power required to maintain the plasma in steady state. To make this reaction possible, a very hot plasma of a few hundred million Kelvin is necessary, which is contained in a large device, the tokamak. Magnetic fields in poloidal and toroidal direction, generated by the giant coils, keep the plasma in the container from touching the wall because the plasma will be cooled down, otherwise. With its large scale in size, that has never been reached so far, the physics will encounter a totally different dimension. However, a lot of questions should be answered to reach this goal. Especially, the plasma confinement is a very challenging issue. For example, in ITER, the required plasma duration to be maintained for fusion reaction is on the order of 1000 s whereas the maximum record of plasma stability -in a much smaller tokamak- was only about 20 s [NFRI, 2015]. The difficulties in sustaining longer plasma confinement time lie in generation of various waves which can cause disruptions leading the plasma into an unstable state. One of the examples is the pellet injection [Brueckner and Jorna, 1974]. It is a fueling mechanism where a pellet of frozen deuterium is accelerated to high speeds and injected into the hot plasma. When it evaporates, the dense plasma expands into a low-density plasma and induces hydromagnetic activities which can, in worst case, grow in large amplitude and endanger the plasma stability [Bodner, 1974, Abel et al., 1997, Taylor et al., 1999]. The questions such as how energy dissipates, what kind of waves are radiated, or what effect it has on the plasma confinement are still debated.

Dense plasma expansion in an ambient magnetized plasma is not only encountered in fusion devices, but also ubiquitous in space and astrophysical environments. These are, for example, coronal mass ejections near the Earth [Richardson et al., 2000], stellar outflows [Mundt et al., 1987], and supernova remnants in further distance [Drury, 1995]. In the 60s, artificial plasma expansion enabled to obtain a deeper knowledge in this area. The Starfish Prime project, a high-altitude nuclear test, was conducted and caused electromagnetic pulse resulting in damaging satellites, power outages in nearby towns, and occurrence of intense visible phenomena like bright aurora [Dyal, 2006]. The barium releases in the magnetotail during the Active Magnetospheric Particle Tracer Explorers (AMPTE) operation [Krimigis et al., 1982] and the chemical release project using the Combined Release and Radiation Effects Satellite (CRRES) [Vampola, 1992] were done to collect information of phenomena in space via spacecrafts with *in situ* measurements aboard. Although various significant findings could be made from the aforementioned projects, the key problem was that the plasma parameters in this regime could not be controlled. The micro-physics in the events were not clearly identified, the accurate measurement of the unstable modes was not possible, and their propagation direction and the frequency shifts due to the Doppler effects could not be estimated either [Wu97]. Therefore, the importance of the well-scaled laboratory experiments arose and gained even more interest

---

---

when the theta-pinch and tokamaks were invented. Since then, a number of experiments have been performed.

In the framework of the study presented in this dissertation, a series of experiments have been carried out at the University of California, Los Angeles (UCLA), in the Large Plasma Device (LAPD) [Gekelman et al., 1991] in combination with the Phoenix Laser Facility [Niemann et al., 2012]. Compared to the arc discharge with non-negligible neutral particle fill pressure [Tonks and Langmuir, 1929] and the tokamak providing a complex magnetic field structure [Stix, 1978], the LAPD creates a space-like environment with a simple axial magnetic field. The density is kept low so that a collisionless regime is achieved, in which the mean free path of particles is large compared to the system size. The energy and the momentum of the ions are mediated by the electromagnetic fields instead of collisional effects. The LAPD plasma is magnetized and large enough to support Alfvén waves<sup>1</sup>. Because of this distinct feature of the machine, various phenomena observed in the Earth's magnetosphere were reproduced and studied in detail over the years [Gekelman, 1999, Gekelman et al., 2003]. One of the main scientific missions at the LAPD was to generate Alfvén waves and study its generation mechanisms, the nature of the wave propagation, the spatial picture, and its capability of heating and acceleration of particles. In space, one of the difficulties encountered in the wave detection by space crafts is caused by the slow variations of the wave characteristics with its long wavelength. Numerous works have been done already on the Alfvén wave generation using different drivers [Gekelman et al., 1997b, Gekelman et al., 1997a, Leneman et al., 1999, Van Compernelle et al., 2005]. Recently, a new generation mechanism has been achieved in an experimental setting combining the LAPD with a laser system [VanZeeland and Gekelman, 2004, Collette and Gekelman, 2010].

When an intense laser beam irradiates a solid target, a rapidly expanding dense plasma which is embedded in a magnetized ambient plasma propagates creating a diamagnetic cavity [Wright, 1971, Grun et al., 1981, Kacenjari et al., 1986]. It is a similar process as those observed in the chemical release experiments near the Earth where the formation and relaxation of the plasma expansion process were studied [Lühr et al., 1986, Bernhardt et al., 1987]. When it expands perpendicularly to the magnetic field, the surrounding magnetic field lines are compressed and develop into a magnetosonic pulse. Under certain circumstances, this magnetosonic pulse exceeds the Alfvén speed  $v_A$  and could become a magnetized collisionless shock. The potential of a diamagnetic cavity as a shock driver has been already proposed in [Drake, 2000, Zakharov, 2003, Constantin et al., 2009] and recently, a quasi-perpendicular collisionless shock has been launched successfully [Niemann et al., 2014, Schaeffer et al., 2014]. Simultaneously, along the magnetic field lines, fast electrons escape from the diamagnetic cavity and radiate various waves in a large spectrum [Vincena et al., 2008] including Alfvén waves [VanZeeland et al., 2001]. This generation mechanism for the Alfvén waves is based on the Cherenkov radiation via high energetic pulses of field aligned electrons [Jackson, 1962, Van Compernelle et al., 2008].

In experiments at the UCLA, a diamagnetic cavity was created using a low-energy laser ( $\leq 30$  J) in conjunction with the LAPD to study its properties and the generated hydromagnetic wave

---

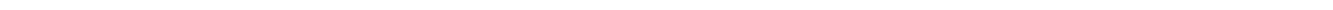
<sup>1</sup> The typical wavelength of the generated Alfvén waves in this experiment is on the order of a few meter so that the propagation of these waves along the magnetic field can be observed in the LAPD with its length of about 20 m while the wave source (the dense laser produced plasma or the generated diamagnetic cavity) is several tens of cms at most. It justifies the device as well as the plasma inside being called "large".

---

structures [Niemann et al., 2013]. This study follows up on the earlier work concerning the evolution of a diamagnetic cavity in a super-Alfvénic regime where the diamagnetic cavity expansion velocity exceeds  $v_A$  and at higher laser energies (up to 200 J). The overall development of the diamagnetic cavity looks similar to the low energy case, albeit its larger size. The production of various waves at the cavity edge and instabilities in fluctuating magnetic and electric fields were detected using magnetic flux probes [Everson et al., 2009] and electron emissive probes [Martin et al., 2015], respectively. In this regime, a stronger coupling between the background and the debris plasma was observed. Along the magnetic field, the diamagnetic cavity generated soliton-like kinetic Alfvén waves, which has not been previously observed. It might be a possible result of the nonlinear interaction between high-energy electrons and the background plasma. The experimental results were compared to numerical simulations using a two-dimensional hybrid code [Winske and Gary, 2007], in which the ions are treated as particles, while the electrons are treated as a fluid. Since the shortest time and length scales relevant to the electron dynamics are neglected, this simulation works well for the large-scale plasmas and in the low-frequency regime, similar to the presented experiment. The code has already proven successful in modeling high Mach number space and astrophysical phenomena [Winske and Gary, 2007], but also to simulate laboratory experiments [Hewett et al., 2011, Clark et al., 2013].

The outline of this dissertation is as follows: Chapter 2 describes the fundamental physics related to the laser plasma interactions, the generation of laser produced diamagnetic cavity, and its coupling to the ambient magnetized plasma. Additionally, its capability of quasi-perpendicular shock formation and Alfvén wave excitation parallel to the magnetic field are presented. It also includes the theory of the instabilities observed at the cavity edge and an introduction of the magneto-hydrodynamic (MHD) Energy Principle, a tool to predict theoretically the occurrence of instabilities. The experimental setup and the diagnostic tools applied in the experiment are introduced in Chapter 3. The experimental results in Chapter 4 are divided in two sections according to the diamagnetic cavity expansion geometry relative to the magnetic field. First, the coupling of the diamagnetic cavity to the ambient plasma and its features observed during its perpendicular expansion in magnetic and electric field are presented, followed by the instabilities detected at the cavity edge. Then the kinetic Alfvén wave radiation measured along the magnetic field lines and its different characteristics compared to those generated by the lower laser energy follow. The results from the numerical simulations using the two-dimensional hybrid code relevant to the experiment are shown in Chapter 5 and finally, in Chapter 6, the conclusions of this work and the future perspectives are presented.





---

## 2 Theory

---

The scope of this dissertation is to investigate a dense plasma produced by a laser beam, which expands into a low-density plasma region with a velocity exceeding the Alfvén velocity  $v_A = B/\sqrt{\mu_0 n_i m_i}$  where  $B$  is the magnetic field strength,  $\mu_0$  the magnetic permeability,  $n_i$  and  $m_i$  are the density and mass of the plasma ions  $i$ , respectively. This process occurs in a collisionless regime where the collisional effect between particles can be ignored because the density is low and the mean free path of ions is larger than the system size. The coupling mechanism and the energy and momentum transfer between the particles are carried out by the magnetic and electric field, and therefore, in the expansion process of the dense plasma, a variety of phenomena are observed in the perpendicular as well as in the parallel geometry. This chapter summarizes some of the theoretical works relevant to the experiment.

---

### 2.1 Laser-plasma interaction

---

Plasma is a denotation for an ionized gas containing not only neutral atoms, but also positive ions and negatively charged electrons. About 99 % of the visible matter in the universe is known to be in the plasma state while on Earth the plasma does not frequently occur naturally. The plasma is influenced by external electric and magnetic fields, but the particles themselves also generate electromagnetic fields or currents self-consistently, affecting even the movement of the charged particles in a far distance. Due to this "collective" character of the plasma, it is not straightforward to predict the behavior of single particles. Moreover, it is impossible to describe the behavior of each particle, for instance, in a typical plasma with  $10^{12}$  ion-electron pairs per  $\text{cm}^3$ . Therefore, a fluid element instead of the individual particles is assumed to describe the movement of plasma using magneto-hydrodynamic (MHD) equations. Fortunately, about 80 % of the observed plasma phenomena can be described by this crude model [Chen, 1984].

Light with intensity greater than  $10^9 \text{ W/cm}^2$  is able to create a plasma on the surface of a solid state sample [Dawson, 1964]. The electromagnetic field of the laser excites the free electrons of the solid surface to a vibrational motion and eventually accelerates them. This is an inverse bremsstrahlung process where a photon is captured by an electron [Meyer and Thiell, 1984] which results in heating or even evaporation of the target surface. In the initial phase shortly after the laser irradiation, the plasma is highly collisional and isothermal, and its temperature depends on the laser-target interaction [Singh et al., 1990]. As the laser intensity increases, the free electrons gain additional energy to generate secondary electrons via collisions with neutral atoms or ions. Hence, the most dense plasma area is situated on the target surface and its density decreases exponentially with distance [Dawson, 1964]. The laser continues heating the plasma until its density reaches the critical density

$$n_c = \frac{\omega_L^2 m_e \epsilon_0}{e^2} \quad (2.1)$$

where  $\omega_L$  is the laser frequency,  $m_e$  the electron mass,  $\epsilon_0$  the dielectric constant, and  $e$  the elementary charge. At this density, the electrons in the plasma oscillate with the electron plasma frequency,

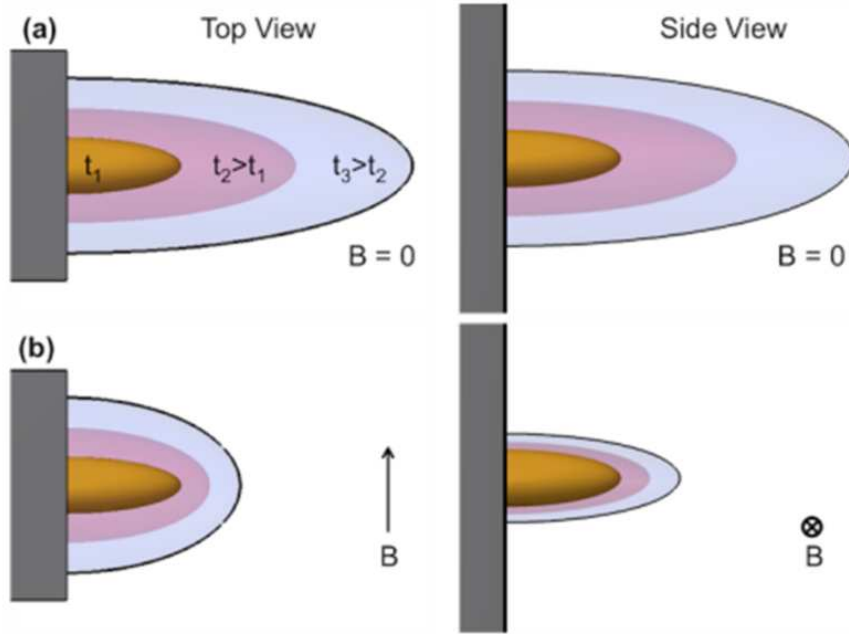


**Figure 2.1:** Schematic of laser produced plasma evolution a) without and b) with background magnetic field after laser irradiation on a solid target. Its ellipsoidal form is mainly caused by the pressure anisotropy and affected by the presence of the external magnetic field. Extracted from [Schaeffer, 2014].

$$\omega_e = \sqrt{\frac{n_e e^2}{m_e \epsilon_0}} \quad (2.2)$$

with  $n_e$  the electron density. For the density larger than  $n_c$ , the laser energy cannot be absorbed and the beam is reflected. But as the plasma region keeps increasing, the plasma density decreases dropping its frequency below the laser frequency. Then the beam penetrates the area of lower density so that the dense surface is again irradiated and heated. The process repeats for the duration of the laser pulse.

Due to the intensity non-uniformity on the target, a larger pressure and density gradient perpendicular to the target results in acceleration of the plasma much more quickly in the perpendicular direction. This anisotropic pressure causes an elongated football shape of the plasma (Figure 2.1 a). When an external magnetic field is applied, the shape of the laser produced plasma changes. In the early process, the plasma expands freely into the vacuum and the presence of the background magnetic field does not seem to affect its shape (Figure 2.1 b). However, as soon as the plasma pressure becomes comparable to the magnetic field pressure, the similarity between the two cases disappears because the magnetic field provides external pressure.

---

## 2.2 Coupling between debris-ambient plasmas

---

When the laser irradiates the target, the surface is ionized and electrons are ripped off from the target generating a strong electric field. On a time scale short compared to the ion gyroperiod, the ions are considered to be unmagnetized while the electrons are magnetized because they are

tied to the magnetic field due to their small mass. The ions overshoot the electrons and give rise to a radially inward directed ambipolar field (Figure 2.2 a). The magnetic field perpendicular to  $\vec{E}_r$  will generate an  $\vec{E} \times \vec{B}$  drift of the electrons and the pressure gradient of the laser plasma  $\nabla p_e$  in radial direction also contributes to the azimuthal current flow [Wright, 1971]. This so-called diamagnetic current at the plasma edge generates a magnetic field opposite to the applied external field. As the ambient magnetic field and background ions are expelled outward (toward the plasma edges), a diamagnetic cavity is formed (Figure 2.2 b). As a result, the magnetic field bends around the plasma enhancing the magnetic field outside of the cavity (Figure 2.2 c). The compressed magnetic field propagates as the laser produced plasma expands and eventually develops into a magnetosonic pulse. Considering the law of energy conservation and neglecting any kinds of energy loss for simplicity, the total expelled magnetic field energy is equal to the laser energy such that

$$E_{laser} = \frac{B^2}{2\mu_0} \frac{4\pi}{3} R_B^3 \quad (2.3)$$

if one assumes a spherical expansion of the plasma in vacuum. A diamagnetic cavity is created with the magnetic stopping radius  $R_B$ . Taking the background plasma into account, the laser produced plasma exchanges energy with the surroundings and the diamagnetism becomes complex because the background electrons can flow down the magnetic field lines. This reduces the self-consistent  $\vec{E} \times \vec{B}$  current in the laser produced plasma and the plasma diamagnetism. Considering the ambient plasma motion, the energy equation is modified accordingly,

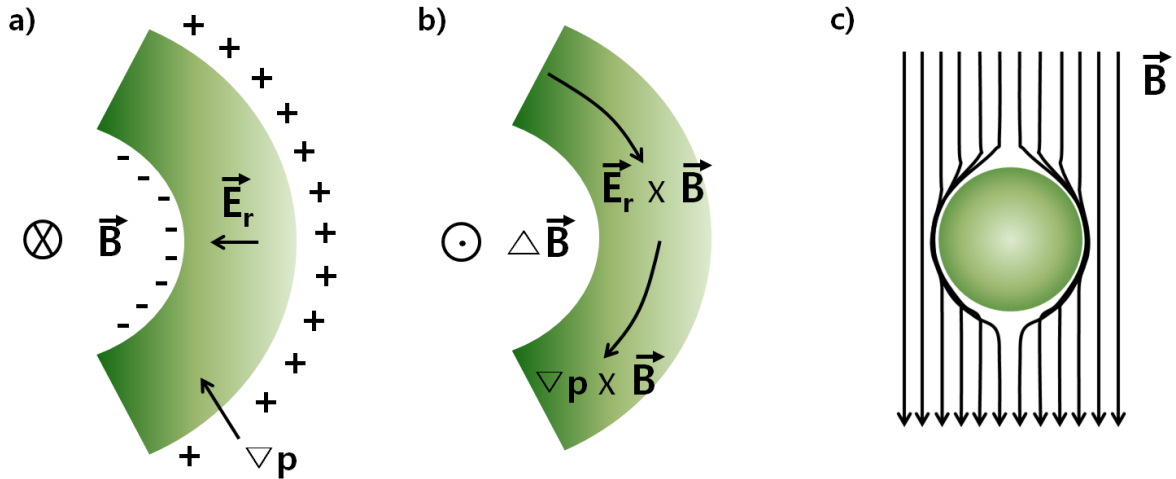


**Figure 2.2:** a) The charge separation of unmagnetized ions and magnetized electrons in the laser produced plasma gives rise to a radial electric field  $\vec{E}_r$ . b) Due to the radial field, the ions on the outer edge are slowed down while the ions inside catch up resulting in plasma compression into a thin shell. The radial electric field and the inward pointing pressure gradient at the plasma edge interact with the perpendicular magnetic field and generate azimuthal diamagnetic currents. c) The expelled magnetic field accumulates around the plasma (green sphere).

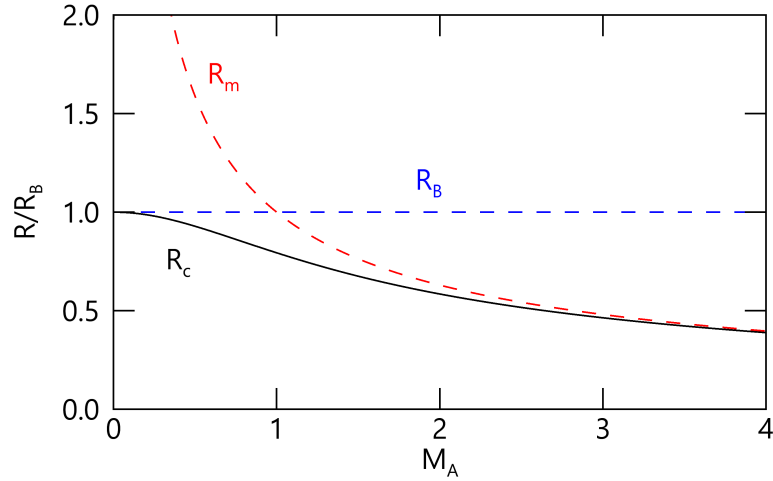


**Figure 2.3:** Relation between the cavity radius  $R_c$ , the magnetic stopping radius  $R_B$ , and the equal mass radius  $R_m$  as a function of expansion velocity in  $M_A$ . Adapted from [Clark et al., 2013].

$$E_{laser} = \left( \frac{B^2}{2\mu_0} + \frac{m_a n_a v_d^2}{2} \right) \frac{4\pi R_c^3}{3} \quad (2.4)$$

where  $v_d$  is the drift velocity of the surrounding ions,  $R_c$  the actual cavity radius, and  $m_a$  and  $n_a$  describe the ambient ion mass and density, respectively. Here, the laser energy is used partly to accelerate ions of the ambient plasma as described by the second term. If all the laser energy is used to accelerate ambient ions, the diamagnetic cavity will expand up to a sphere with the radius  $R_m = (3n_d m_d / 4\pi n_a m_a)^{1/3}$ , the equal mass radius, where  $d$  and  $a$  stand for debris and ambient ions, respectively. The magnetic stopping radius as well as the equal mass radius depend on the Alfvénic Mach number  $M_A = v_d / v_A$  so that [Clark et al., 2013]

$$\frac{R_c}{R_B} = (1 + M_A^2)^{-1/3}, \quad \frac{R_m}{R_B} = M_A^{-2/3}. \quad (2.5)$$

These equations are the requirements for energy transfer to the ambient plasma and mean that the interaction between the debris and ambient plasma is dominant only if the Mach number of the debris ions is greater than 1, i.e. super-Alfvénic [Bashurin et al., 1983]. One can see in Figure 2.3 that the cavity radius  $R_c$  never exceeds the magnetic stopping radius  $R_B$  and approaches the equal mass radius  $R_m$  asymptotically for large  $M_A$ . The real size of the diamagnetic cavity results in a value between  $R_c$  and  $R_B$  according to the coupling efficiency [Clark et al., 2013]. A change of the ion charge density of the ambient plasma and the pulse length of the expanding plasma are known to affect the degree of coupling. The efficient coupling between debris and ambient plasma occurs when the threshold  $\alpha$  is greater than 1,

$$\alpha \equiv \left( \frac{\pi}{2} - 1 \right) \frac{Z_d n_d}{Z_a n_a} \quad (2.6)$$

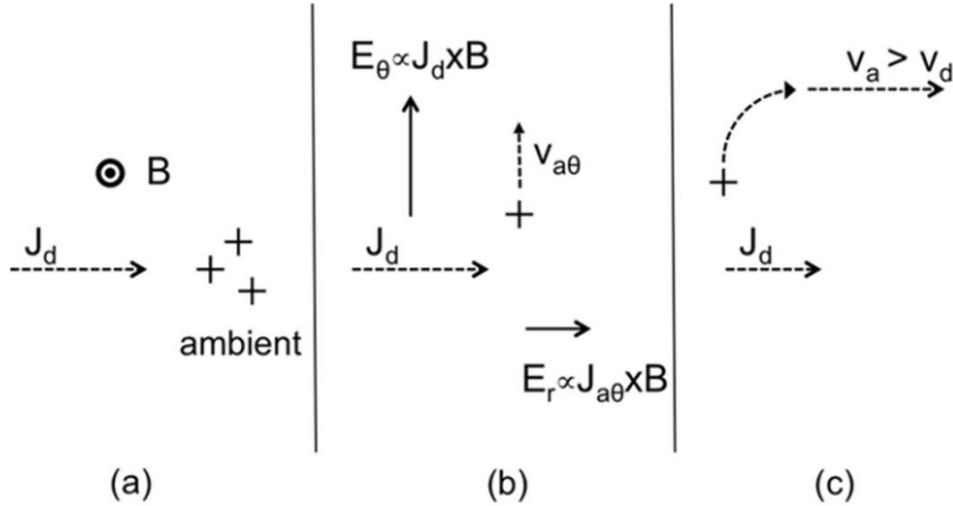


**Figure 2.4:** Schematic of Larmor coupling: a) The radially expanding ions from the laser produced plasma generate an azimuthal electric field in conjunction with the magnetic field. b) The stationary ambient ions are accelerated and induce an azimuthal current. c) The Lorentz force acts on this current and causes a gyrating movement of the ions into the radial direction after one quarter of the gyroperiod. The coupling between the debris and ambient ions occurs if the radial velocity of the ambient ions is comparable or greater than that of the debris ions. Extracted from [Schaeffer, 2014].

where  $Z$  is the charge state of the ions [Hewett et al., 2011]. If  $\alpha$  is greater than 1, the debris will couple to the background plasma. In case with a low background electron charge density, the azimuthal electric field is so large that the background ions will accelerate to more than the debris drift speed in  $1/4$  of the background ion gyroperiod. The background will be directed in the radial direction by the end of this period with an energy sufficient to move with or in front of the debris. The debris ions are "coupled" to the background plasma. It is also required that the background ions are immersed in a strong enough azimuthal electric field for a sufficient time so that they have enough speed to get in front of the debris pulse. Thus, a smaller gyroradius  $\rho_i = m_i v_\perp / Z_i e B$ , where  $v_\perp$  is the velocity component perpendicular to the magnetic field, associated with higher charge states in the background ions will enhance the coupling efficiency.

In the presented experiments, one must consider collisionless coupling of particles because the ion-ion collisional mean free path is larger than the system size. The energy and momentum transfer between particles are mediated via electromagnetic fields instead of collisions so that the collisional effects can be ignored. Berezin *et al.* proposed in their work [Berezin et al., 1998] that there are two different kinds of collisionless coupling processes: turbulent and laminar coupling. The turbulent coupling occurs via beam instabilities excited by the free energy inside the plasma. The modified two-stream instability [McBride et al., 1972] and the ion-ion two-stream instability [Papadopoulos et al., 1971] are the possible drivers of this mechanism and this coupling becomes interesting for low Mach number. In the laminar process, an electric field that couples the laser produced plasma to the ambient plasma is generated

$$\vec{E} = -\frac{\nabla p_e}{en_e} - \frac{\vec{B} \times (\nabla \times \vec{B})}{\mu_0 en_e} - \frac{\sum_i \vec{J}_i \times \vec{B}}{en_e} \quad (2.7)$$

where  $\vec{J}_i$  is the ion current of the species  $i$ . The first term is called the electron pressure gradient term which is negligible when the electron beta  $\beta_e = 2\mu_0 n_e k_B T_e / B^2$  is small. The second term is the magnetic pressure and curvature term. It is large compared to the first term, but for increasing  $M_A$ , the third term is known to dominate the other two components [Hewett et al., 2011]. This Larmor term is responsible for collisionless energy transfer between the dense laser produced plasma and the ambient plasma (Figure 2.4).

### 2.3 Quasi-perpendicular shock formation

Under certain circumstances, the magnetosonic pulse arisen from the magnetic compression at the diamagnetic cavity edge develops into a collisionless magnetized shock, which is one of the phenomena often observed in the Earth's magnetosphere [Greenstadt and Mellott, 1987, Wilkinson, 2003, Russell, 2005]. The main research goal of the presented experiment is launching a collisionless shock in a laboratory setting. In this section, a summary and the possibility of shock generation in the given experimental setting are presented.

The collisionless shocks have been predicted first theoretically in the 1950s [Sagdeev, 1966]. Its research gained large interest and importance since the discovery of the Earth's bow shock [Ness and Wilcox, 1964] and the development of the theta-pinch for fusion research [Rose and Clark, 1961]. Numerous experiments in space as well as theoretical studies have been done since then [Leroy, 1983, Russell, 2005, Dyal, 2006]. The collisionless shocks can

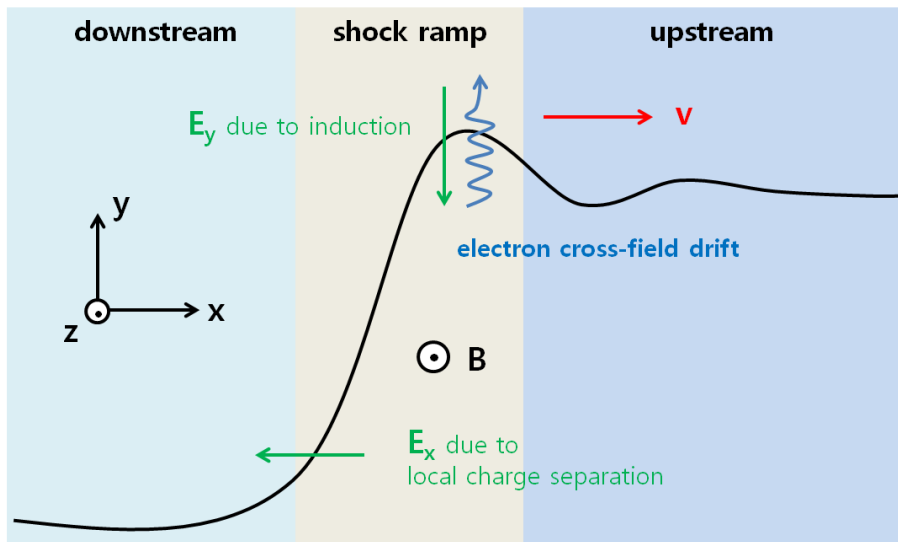


**Figure 2.5:** One-dimensional schematic of a subcritical shock propagating in x-direction, in one-dimension. The charge separation of the particles in the shock ramp due to the different ion magnetization generates a radial electric field which, in turn, induces  $\vec{E} \times \vec{B}$  drift. This azimuthal drift compresses the magnetic field which propagates as a magnetosonic pulse or a shock into the upstream region. Adapted from [Wu, 1982].



be divided in two different categories according to the shock normal angle  $\theta$  to the background magnetic field: the (quasi-) perpendicular and (quasi-) parallel shocks. In a quasi-parallel case,  $0^\circ \leq \theta \leq 45^\circ$ , the transition length of the shock is extending over a long distance making its detection difficult [Wilkinson, 2003]. In contrast, the (quasi-) perpendicular ones with  $45^\circ \leq \theta \leq 90^\circ$  are easier to detect due to their sharp transition from upstream (a region the shock has not reached yet) to downstream region (a region the shock has already passed by). And it is also often observed in a controlled thermonuclear fusion experiment when the plasma is heated by magnetic compression [Bobin, 1974].

A collisionless shock is formed when a plasma flowing at a super-Alfvénic velocity encounters a large obstacle. The obstacle reflects ions upstream and will create an ion-ion beam instability that generates magnetosonic waves into the upstream region. If the plasma flow velocity exceeds the wave group velocity, the wave steepens and the dispersion inside the wave generates a solitary wave with its thickness on the order of the ion inertial length  $c/\omega_{pi}$  with  $\omega_{pi} = \sqrt{n_i e^2/m_i \epsilon_0}$  the ion plasma frequency and  $c$  the speed of light. When the upstream ions hit the ramp of the soliton, the cross-shock potential is produced due to the different gyroradii of ions and electrons. If the potential is not strong enough to reflect the ambient ions, it produces a cross-field drift of the electrons driving current in the shock ramp along the shock. The magnetic field of this current causes a magnetic overshoot and the relative drift excites anomalous instabilities which will prevent large amplitude waves from indefinite steepening. The ions are retarded and thermalized providing the required dissipation of kinetic energy leading to shock formation. The magnetosonic speed of the shock depends on the wave propagation angle  $\theta$  with respect to the magnetic field [Treumann, 2009],

$$c_{ms}^2(\theta) = \frac{1}{2}c_{ms}^2 \pm \frac{1}{2} \left[ (v_A^2 - c_s^2)^2 + 4v_A^2 c_s^2 \sin^2 \theta \right]^{1/2} \quad (2.8)$$

where  $c_{ms}^2 = v_A^2 + c_s^2$  is the angle-independent expression with  $c_s = \sqrt{k_B T_e/m_i}$  the sound speed. If the oncoming flow is faster than the sound speed, the information about the obstacle cannot propagate quickly enough upstream to directly affect particles. To compensate, a region is established that acts to slow the incoming flow from  $M_A > 1$  to  $M_A < 1$  on the short distance at the expense of increased entropy. In this boundary region, the Rankine-Hugoniot conservation laws using the ideal MHD equations describe the flow across the discontinuity between upstream and downstream values of density  $n$ , velocity  $v$ , magnetic field  $B$ , and pressure  $p$  in the global transition [Burgess, 1995, Treumann, 2009, Schaeffer, 2014],

$$\frac{v_d}{v_u} = \frac{n_u}{n_d} = \frac{B_u}{B_d} = \frac{1}{8} \left[ 1 + \frac{1 + 2.5\beta_{e,u}}{M_A^2} + \left[ \left[ 1 + \frac{1 + 2.5\beta_{e,u}}{M_A^2} \right]^2 + \frac{2}{M_A^2} \right]^{1/2} \right] \quad (2.9)$$

where the subscripts  $u$  and  $d$  denote the upstream and downstream regions, respectively,  $\beta_{e,u} = 2\mu_0 n_u k_B T_u / B_u^2$  the plasma beta in the upstream region, and  $T$  the total temperature. For the marginal  $\beta_e$  and quasi-perpendicular low Mach number plasmas in the experiment, the above equation can be approximated to  $B_u/B_d \sim M_A^{-1}$ .

According to the shock velocity, collisionless shocks can be further classified into supercritical when the Mach number exceeds the critical value  $M_{A,crit} \sim 2.76$ , otherwise subcritical. The critical Mach number is either determined experimentally or via numerical calculation depending

on  $\beta_e$  and the shock normal angle  $\theta$  [Marshall, 1955]. For a supercritical shock, the electric potential in the shock ramp is large enough to reflect the ambient ions providing the additional dissipation. Any other anomalous dissipation mechanisms cannot explain how to get rid of the excess energy and micro-instabilities are not enough to provide sufficient dissipation [Treumann, 2009]. In a subcritical shock case, the cross-field drift from the relative gyroradii between ions and electrons in the shock transition layer can excite instabilities that provide anomalous resistivity. It is assumed that the relevant processes are based on wave-particle interaction between the shocked plasma population and the shock-excited turbulent wave field, but it is not identified fully yet. For subcritical shocks, the process by which the shock forms can be described well theoretically. The reviews to the corresponding topics can be found in [Sagdeev, 1966, Tidman and Krall, 1971, Scudder et al., 1986].

Laboratory experiments with laser produced plasmas to study astrophysical phenomena, such as the dynamics of supernovae remnants in interstellar uniform magnetic fields, were already suggested in the 1960s [Dawson, 1964]. The goal of laser driven shock experiments is to study particle acceleration, measure the turbulence they produce, and to diagnose the evolution of the particle distribution, which are difficult to measure in space where the plasma parameters cannot be controlled. In various works [Drake, 2000, Zakharov, 2003], the diamagnetic cavity is thought to be a good initiator to drive a shock and pictured as a piston. The methods by which the piston couples energy to the ambient ions must be understood in order to maximize the coupling efficiency. In [Drake, 2000], the experimental requirements for a successful shock formation in a laboratory setting are given:

- 1) the upstream ion flow must be super-Alfvénic,
- 2) the collisional mean free path between shocked ions must be larger than their gyroradii,
- 3) in order to setup a cross-ramp potential, the shocked ions must be sufficiently magnetized,
- 4) the system size should be large enough for a shock to propagate,
- 5)  $R_c/\rho_i$ , the ratio between the cavity radius and the ion Larmor-radius, should exceed 1 [Golubev et al., 1979, Bashurin et al., 1983].

$R_c/\rho_i$  is an important dynamical parameter which is known to influence the intensity of collisionless interactions between the expanding plasma and the surroundings [Dimonte and Wiley, 1991, Berezin et al., 1998].

---

## 2.4 Instabilities

---

Plasmas are in an equilibrium state when all forces are in balance and a time-independent solution is possible. When free energy is available, waves can be self-excited and the equilibrium then becomes an unstable one. An instability always decreases the free energy and brings the plasma closer to its true thermodynamic equilibrium. It is known to be a crucial factor for plasma confinement. However, not all instabilities are equally dangerous. For example, a high-frequency instability near the ion plasma frequency  $\omega_{pi}$  cannot affect the motion of heavy ions due to its inability of transporting particles across the magnetic field [Wu, 1982]. But in mirror machines, the particles might be lost by diffusion in velocity space into the loss cone affecting the plasma confinement [Davidson and Ogden, 1975]. In contrast, low-frequency instabilities can cause anomalous ambipolar losses via  $\vec{E} \times \vec{B}$  drifts which arise from the relative electron-ion drift in the magnetic compression shell. It is the free energy source for instabilities.

In the following section, the most probable candidates for a micro-instability at the cavity edge are presented. As there are similarities between the cross-field currents found in the shock ramp and the micro-instabilities at the edge of the diamagnetic cavity, the shock instabilities are assumed to be the micro-instabilities occurring in our experiment. The cross-field instabilities are classified into two categories according to their frequency regime: low-frequency (e.g., ion-ion streaming [Stringer, 1964], lower-hybrid-drift instability [Gary and Sgro, 1990]) and high frequency modes (e.g., electron cyclotron drift [Wong, 1970], electron whistler instabilities [Mikhailovskii, 1974]). In scope of this dissertation, the focus is only on the low-frequency modes. Subsequently, a brief introduction of the application of MHD Energy Principle is given. Since its theory has been covered in more detail in other works [Meister et al., 2014], only a few relevant aspects will be discussed.

---

### 2.4.1 Micro-instabilities at the cavity edge

---

In the absence of particle collisions, the plasma turbulence associated with anomalous heating in the shock front is known to give rise to the required dissipation resulting in entropy production and generation of instabilities in the shock transition regime [Tidman and Krall, 1971]. The types of waves and the characteristics of the heating depend on the sources of the free energy that drive the instabilities, which, in turn, are connected to the nature of the shock. Some works in the past [Petschek, 1958, Fishman et al., 1960] proposed that standing whistler waves or wave-wave interactions could be responsible for the dissipation mechanism. But later, it was found that the nonlinear wave-wave interaction process in general does not lead to a sufficiently rapid and effective plasma heating [Wu, 1982]. As the characteristic shock transition time is less than the ion gyroperiod, the interaction between the turbulence and the plasma should be very efficient. Nowadays, the possible candidate for the dissipation mechanism is the cross-field current in a magnetosonic pulse giving rise to dissipative wave-particle interactions. This current is the principal source of the instability which heats the electrons and ions. The difficulty in the identification of the individual wave modes from space data lies in the fact that only Doppler shifted frequencies are measured and the wave vectors cannot be resolved well.

One potential candidate for the unstable waves is the ion acoustic wave which becomes unstable at  $c_{ia} < v_{\parallel} < v_e$  where  $c_{ia}$  is the ion acoustic velocity [Bobin, 1978]. This wave is known to cause the anomalous collision frequency favored by high electron temperature, but the required velocities are high and it is not clear if these waves contribute to subcritical shocks. Moreover, in many laboratory experiments as well as at the bow shock, conditions for the excitation of the ion acoustic instability are not satisfied [Winske et al., 1985, Treumann, 2009]. The lower-hybrid mode waves are introduced as possible initiators for instabilities at the cavity edge, which arise when the shock transition length scale is comparable or shorter than the ion inertial length: the modified two-stream (MTSI) [McBride et al., 1972] and lower-hybrid-drift instability (LHDI) [Krall et al., 1971]. These two instabilities have much lower thresholds than the ion acoustic instability providing the required dissipation in subcritical shocks. They have frequency and growth rates in the lower-hybrid frequency range and wavelengths that are longer than the electron, but shorter than the ion gyroradius and propagate nearly perpendicular to the magnetic field.

**Modified two-stream instability (MTSI):** MTSI is excited when there exists -even if weak- currents flow perpendicular to the magnetic field and when the shock-normal electric field across

Type of instability	Growth rate	Frequency
Modified two-stream instability [Huba, 2004]	$0.5\omega_{LH}$	$0.9\omega_{LH}$
Lower-hybrid-drift instability [Wu et al., 1984]	$\gg \omega_{ci}$	$\omega_{LH}$

**Table 2.1:** Possible micro-instabilities generated at the cavity edge/subcritical shock ramps with the lower-hybrid gyrofrequency  $\omega_{LH} = \sqrt{\omega_{ci}\omega_{ce}}$  where  $\omega_{ci} = Z_i eB/m_i$  the gyrofrequency of ion and  $\omega_{ce} = eB/m_e$  that of electron.

the shock ramp transition is equal to or shorter than the length of the shock ramp in order to keep the ions unmagnetized. The electron-ion relative drift exceeds the Alfvén speed of the plasma. Once the wave quasi-linearly saturates, anomalous collisions scatter the electrons ambipolarly across the shock to shorten the length scale below the ion inertial length so that the ions are kept unmagnetized. The electron drift scale is too short to maintain the instability, but the joule heating of electrons and ions produces an entropy increase. The theory of MTSI is given in the fluid limit and the dispersion relation is very similar to that for the Buneman two-stream instability [Buneman, 1962], which is where the modified two-stream instability has its name from. The threshold velocity, which is the electron-ion relative drift velocity, is on the order of the ion thermal velocity or greater than that of the electron. The frequency and the growth rate are comparable to the lower-hybrid frequency [McBride et al., 1972].

**Lower-hybrid-drift instability (LHDI):** when unmagnetized ions and magnetized electrons drift azimuthally in a uniform magnetic field, the ion momentum equation for radial electric field can be written as follows [Winske et al., 1985],

$$eE = -m_i g - T_i \frac{1}{n} \frac{\partial n}{\partial x} \quad (2.10)$$

where  $g$  is the deceleration of the ions and  $T_i$  the ion temperature. Thus,  $v$  is

$$v = -\frac{E}{B} = \frac{m_i}{eB} g + \frac{T_i}{eB} \frac{1}{n} \frac{\partial n}{\partial x}. \quad (2.11)$$

The first term describes the unmagnetized ion Rayleigh-Taylor instability caused due to the decelerated plasma by the magnetic field and the second term is the lower-hybrid-drift instability driven by the ion pressure gradient. In their pure form, the first term grows with a longer wavelength and on a faster time scale than the second term [Huba et al., 1987]. Although these two terms have different characteristics, it is not easy to distinguish one from the other as both grow in a decelerated plasma since, in this regime, the pressure gradients always exist. LHDI is sometimes called a flute-like drift mode. Its name "flute" comes from the fluted Greek columns regarding the ripples on the surface, which result from the random thermal fluctuations. The drift of ions causes a charge to build up on the sides of the ripple and an electric field develops which changes sign as one goes from crest to trough in the perturbation. When the plasma interacts with the magnetic field which, in turn, compresses the plasma acting as a pseudogravity, gradients in pressure are produced and cause the electrons drift with the diamagnetic drift velocity  $v_{di}$  within the plasma,

$$v_{di} = -\frac{\nabla p \times \vec{B}}{qnB^2}. \quad (2.12)$$

This drift causes charge separation and generates a polarization electric field  $\vec{E}_p$ , which results in increasing of the perturbation due to  $\vec{E}_p \times \vec{B}$  drift. The electron-ion and electron-electron collisions are known to stabilize the instability.

---

## 2.4.2 Application of Energy Principle

---

The study of plasma instabilities in nuclear fusion systems is important as they cause interruption of the fusion process and affect the plasma confinement. At the same time, this is a complex problem because the inverse growth rates of MHD instabilities are known to be smaller than 5 % of the observation time [Freidberg, 1987]. The calculation of the kinetic growth rate is very difficult. The MHD Energy Principle is introduced as a tool to predict the occurrence of the instability without knowing its growth rate. It deals with a variational problem for the potential energy and makes use of the fact that a system is unstable if the potential energy of the plasma decreases for any small displacements  $\vec{\xi}$ . In this case, the negative square of an excited wave frequency is related to the potential energy decrease. It is only applicable if the forces on the plasma are self-adjoint, that is, the vectors  $\vec{\xi}$  and  $\vec{\eta}$  satisfy

$$\int_P \vec{\eta} \cdot \vec{F}(\vec{\xi}) d\vec{r} = \int_P \vec{\xi} \cdot \vec{F}(\vec{\eta}) d\vec{r} \quad (2.13)$$

with the force operator  $\vec{F}$  and the unperturbed plasma volume  $P$ . For the ideal MHD, where the electrical conductivity is infinite, the potential energy  $W$  can be given as follows [Bernstein et al., 1958, Freidberg, 1987],

$$W = W_F + W_S + W_V \quad \text{with} \quad \vec{Q} = \nabla \times (\vec{\xi} \times \vec{B}_0) \quad (2.14)$$

where  $\vec{B}_0$  is the magnetic field at  $t = 0$ ,  $W_F$ ,  $W_V$ , and  $W_S$  are the potential energy of the fluid, the vacuum, and the surface in the system, respectively, with

$$W_F = \frac{1}{2} \int_{V_p} \left[ \frac{\vec{Q}^2}{\mu_0} + \frac{1}{\mu_0} (\nabla \times \vec{B}_0) (\vec{\xi} \times \vec{Q}) + (\nabla \cdot \vec{\xi}) (\vec{\xi} \cdot \nabla) p_0 + \gamma p_0 (\nabla \cdot \vec{\xi})^2 \right] d\vec{r}, \quad (2.15)$$

$$W_V = \frac{1}{2\mu_0} \int_{V_v} (\delta \vec{B}_V)^2 d\vec{r}, \quad (2.16)$$

and

$$W_S = -\frac{1}{2} \int_S (\vec{\xi} \cdot \vec{n})^2 \vec{n} \cdot \nabla \left( p_0 + \frac{\vec{B}_0^2}{2\mu_0} - \frac{\vec{B}_V^2}{2\mu_0} \right) d\vec{S}. \quad (2.17)$$

After a tedious calculation and simplification of some terms, e.g. neglecting  $\nabla p$ -term or current-driven instability [Freidberg, 1987], one finds out that  $W_S$  is the only component which can

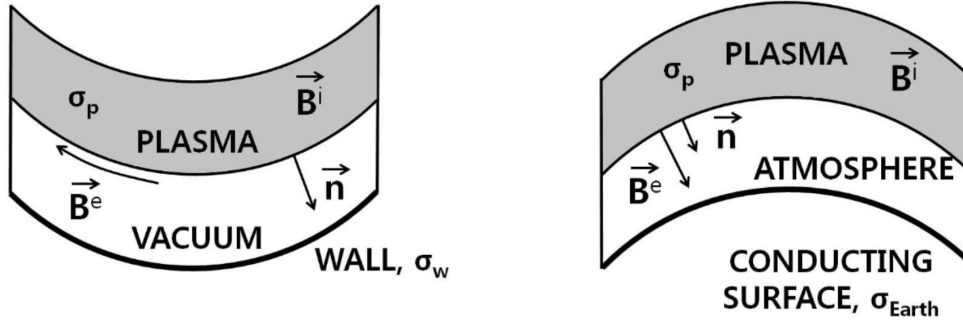


**Figure 2.6:** Boundary conditions of a laboratory plasma (left) and the magnetosphere of the Earth (right) are compared. The major difference in the simplified concept is that the magnetic field at the boundary  $\vec{B}^e$  is perpendicular to the laboratory plasma surface, but parallel to the normal axis of the magnetosphere. Extracted from [Meister et al., 2014].

have a negative value. It means that the instability is contributed by the plasma surface [Spatschek, 1990]. The ideal MHD Energy Principle is not only advantageous for laboratory fusion plasma [Bernstein et al., 1958, Freidberg, 1987], but it can be applied also to the Earth's magnetosphere due to their geometrical similarity [Miura, 2007, Miura, 2011, Miura, 2013]. As shown in the Figure 2.6, the laboratory plasma is contained in a vessel separated by a vacuum layer from the conducting wall while the magnetospheric plasma is segregated from the conducting Earth's surface by the atmosphere. The differences in these simple layouts are that the atmosphere of the Earth contains neutral atoms unlike the vacuum and that the magnetic field in the laboratory plasma is perpendicular and in the system of the magnetosphere parallel to the normal axis of the boundary. The instability in the Earth's magnetosphere is available if  $\eta_{\parallel} = 0$  or  $\nabla \cdot \vec{\xi} = 0$  and  $\eta_{\perp} = 0$  or  $(\vec{B} \cdot \nabla)\xi_{\perp} = 0$  at the unperturbed ionospheric boundaries assuming that the force operator of the Earth's atmosphere is self-adjoint [Miura, 2011].

A homogeneous plasma with an axial magnetic field and negligible electric current along the axis can be approximated according to  $\nabla \times \vec{B}_z = 0$  and  $\nabla p_0 \approx 0$  [Spatschek, 1990, Sturrock, 1996]. Then the equations of motion follow as

$$\vec{F}(\vec{\xi}) = \rho_0 \frac{\partial^2 \vec{\xi}}{\partial t^2}, \quad (2.18)$$

$$\begin{aligned} \vec{F}(\vec{\xi}) = & \nabla(\gamma p_0 \nabla \cdot \vec{\xi} + (\vec{\xi} \cdot \nabla)p_0) + \frac{1}{\mu_0} (\nabla \times \nabla \times (\vec{\xi} \times \vec{B}_0)) \times \vec{B}_0 + (\nabla \times \vec{B}_0) \times (\nabla \times (\vec{\xi} \times \vec{B}_0)) \\ & - \vec{g}((\vec{\xi} \cdot \nabla)\rho_0 + \rho_0 \nabla \cdot \vec{\xi}) \end{aligned} \quad (2.19)$$

which can be reduced to

$$-\omega^2 \rho_0 \vec{\xi}_r = \gamma p_0 \frac{\partial}{\partial r} \nabla \vec{\xi} + \frac{B_z^2}{\mu_0} \left[ \frac{\partial}{\partial r} \frac{1}{r} \frac{\partial \xi_{\varphi}}{\partial \varphi} + \frac{\partial^2 \xi_r}{\partial z^2} + \frac{\partial}{\partial r} \frac{1}{r} \frac{\partial}{\partial r} (r \xi_r) \right], \quad (2.20)$$



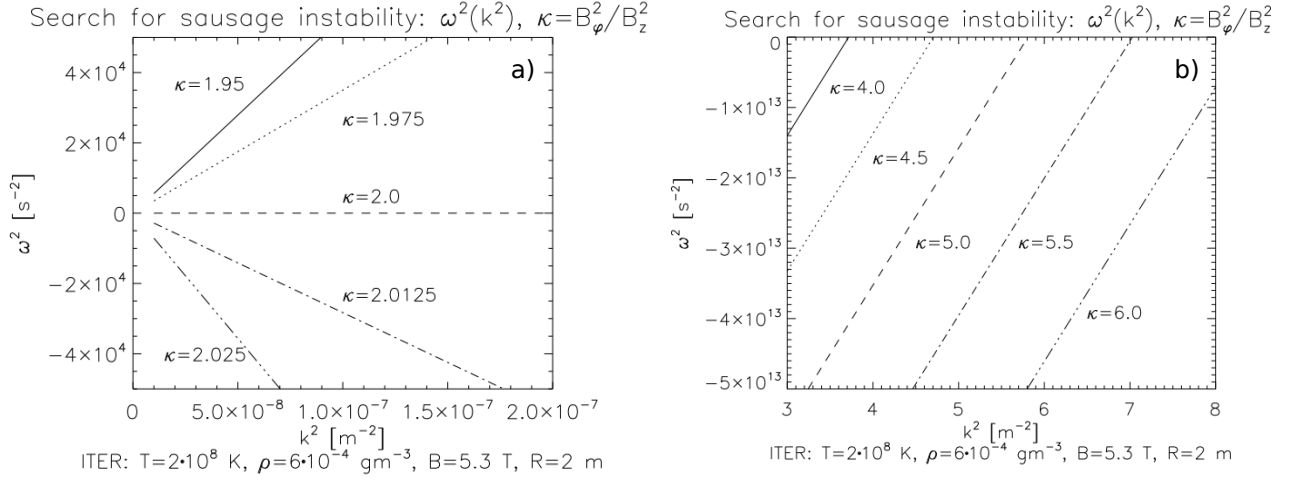


**Figure 2.7:** Dispersion relation of waves in an ITER-type of plasma at different  $B_\varphi/B_z$  for a)  $\alpha R < 1$  and b)  $\alpha R > 1$ . Instability occurs for  $\omega^2 < 0$ . Extracted from [Meister et al., 2014].

$$-\omega^2 \rho_0 \xi_\varphi = \frac{\gamma p_0}{r} \frac{\partial}{\partial \varphi} \nabla \vec{\xi} + \frac{B_z^2}{\mu_0} \left[ \frac{1}{r^2} \frac{\partial^2}{\partial \varphi \partial r} (r \xi_r) + \frac{\partial^2 \xi_\varphi}{\partial z^2} + \frac{1}{r^2} \frac{\partial^2 \xi_\varphi}{\partial \varphi^2} \right], \quad (2.21)$$

$$-\omega^2 \rho_0 \xi_z = \gamma p_0 \frac{\partial}{\partial z} (\nabla \cdot \vec{\xi}). \quad (2.22)$$

Assuming a cylindrical symmetry ( $\partial/\partial \varphi = 0$ ) neglecting  $\xi_\varphi$  and the locally constant magnetic field  $B_z$ , the components of  $\vec{\xi}(\vec{r}) = \vec{\xi}_0(\vec{r}) \exp(im\varphi + ik_z z)$  are given by

$$\xi_r = \frac{v_s^2 (v_A^2 k^2 - \omega^2) - v_A^2 \omega^2}{ik v_s^2 (k^2 v_A^2 - \omega^2)} \frac{\partial \xi_z}{\partial r} = -\frac{i \text{const} [v_s^2 (v_A^2 k^2 - \omega^2) - v_A^2 \omega^2]}{\alpha k} \frac{\partial I_0(\alpha r)}{\partial(\alpha r)}, \quad (2.23)$$

$$\xi_z(r) = \frac{\text{const}}{\alpha^2} I_0(\alpha r), \quad (2.24)$$

and

$$\omega^2 = \frac{B_z^2 k^2}{\mu_0 \rho_0} - \frac{B_\varphi^2}{\mu_0 \rho_0 R^2} \frac{\alpha R [\partial I_0(\alpha R)/\partial(\alpha R)]}{I_0(\alpha R)} \quad (2.25)$$

where  $I_0$  is the modified Bessel function of first kind of order zero and  $R$  the radius of the plasma-vacuum boundary. At  $\omega^2 = v_s^2 v_A^2 k^2 / (v_s^2 + v_A^2)$ ,  $\alpha^2$  diverges. In a regime where  $\alpha^2$  does not diverge, the plasma becomes unstable for a large value of  $\kappa = B_\varphi^2/B_z^2$ .

To show how the energy principle is used to study instabilities, it is applied to an ITER-type plasma system. It should deliver fusion power with its plasma parameters  $B = 5.3$  to  $11.8$  T, the mass density  $\rho = 6 \times 10^{-4}$  g/m<sup>3</sup>, the Alfvén and sound velocity of the plasma  $v_A = 6 \times 10^6$  m/s and  $v_s = 1.2 \times 10^6$  m/s, respectively. Here, the Bessel function of small  $\alpha R$  can be approximated to



$$I_0(\alpha R) \approx 1 + \frac{\alpha^2 R^2}{4}, \quad \frac{\partial I_0(\alpha R)}{\partial(\alpha R)} = \frac{\alpha R}{2} \quad (2.26)$$

and

$$\omega^2 - k^2 v_A^2 = -\kappa v_A^2 \frac{\alpha^2}{(2 + \alpha^2 R^2/2)}. \quad (2.27)$$

Two solutions are, therefore, given as

$$\omega_1^2 = k^2 v_A^2 \quad \text{and} \quad \omega_2^2 = \frac{v_s^2 v_A^2 k^2 (2 - \kappa)}{2v_s^2 + v_A^2 (2 - \kappa)}. \quad (2.28)$$

It can be followed from the above equation that the waves are instable for  $2 \leq \kappa \leq 2 + 2v_s^2/v_A^2$ . The Figure 2.7 a) shows the results for  $\omega_2^2$ . The wave numbers seem to be too small and not important for ITER in case of  $\alpha R < 1$ . But for  $\alpha R > 1$ , the instabilities occur at  $\lambda > 2\pi R/\kappa$ . In the Figure 2.7 b), the instabilities are seen for any  $\kappa$  at  $\alpha R > 1$ , but not for every  $k$ , in contrast to the case  $\alpha R < 1$ . A more detailed explanation to the results is given in [Meister et al., 2014].

---

## 2.5 Generation of Alfvén waves

---

The Alfvén waves, first predicted theoretically by Hannes Alfvén in 1942 [Alfvén, 1942], are fundamental electromagnetic signals and propagate through a perfect conductor along the magnetic field with their characteristic frequency below ion gyrofrequency  $\omega_{ci} = Z_i e B / m_i$ . They are also called shear (or torsional) Alfvén waves because their perturbed field is always transverse to the background magnetic field. In ideal MHD, they are highly anisotropic and propagate without dispersion at  $\omega/k = v_A$ . But when the kinetic effects of finite ion gyroradius and the parallel electron inertia, which are neglected in ideal MHD, are taken into account, the linear properties of the Alfvén waves are modified and their dispersive features become important. Thereby, parallel electric fields are produced, which are capable of accelerating particles, and energy can be transported in medium. Theoretically, two-fluid momentum equations are used to obtain solutions for dispersive Alfvén waves [Stasiewicz et al., 2000]. The dispersion relation holds

$$\frac{\omega^2}{k_{\parallel}^2} = \left[ 1 + k_{\perp}^2 \rho_s^2 - \frac{\omega^2}{\omega_{ci}^2} + k_{\perp}^2 \rho_i^2 \left( 1 - \frac{\omega^2}{\omega_{ci}^2} \right) \right] v_A^2 \quad (2.29)$$

where  $\rho_s$  is the ion gyroradius at electron temperature with  $\rho_s = \sqrt{k_B T_e / m_i} / \omega_{ci}$  and  $\rho_i = \sqrt{k_B T_i / m_i} / \omega_{ci}$  the ion thermal gyroradius. For low frequency case  $\omega^2 / \omega_{ci}^2 \ll 1$ , it can be reduced to

$$\frac{\omega^2}{k_{\parallel}^2} \approx (1 + k_{\perp}^2 \rho_s^2) v_A^2. \quad (2.30)$$

The properties of the dispersive waves become significant when the magnitude of perpendicular wavelength or characteristic scale of spatial inhomogeneities are comparable to  $\rho_s$ .

Despite the importance and frequent detection of Alfvén waves in space, the origin and the evolution processes are still unclear and a more in-depth research is necessary. These waves are also known to exist as background oscillations in laboratory plasmas [Cramer, 2011] and have the ability to affect the plasma confinement if grown to large amplitudes as a form of toroidal Alfvén modes (TAE), triggered by high energetic particles [Heidbrink, 2008]. In the LAPD, various drivers such as helical antennas [Gekelman et al., 1997a], disk exciter [Gekelman et al., 1997b, Leneman et al., 1999], or high power pulse at electron plasma frequency [Van Compernelle et al., 2005] were used to launch Alfvén waves. The excited Alfvén waves by a small source whose size was comparable to the electron skin depth length propagated not only along the magnetic field, but spread radially within Alfvén cones, thus the energy transport in transverse direction was possible. From these previous works, it could be concluded that the morphology of the Alfvén waves depends on the generation mechanism [Gekelman et al., 2011]. Recently, a new mechanism of Alfvén wave generation has been proposed [VanZeeland et al., 2001]. A laser produced plasma interacts with a low-density background plasma and creates a diamagnetic cavity when it expands into a magnetic field. In contrast to the vacuum, where the electrons are kept back by the strong ambipolar field and do not escape from the cavity, the electrons from the background plasma stream down the field lines into the cavity due to the charge neutralization and reduce the diamagnetic

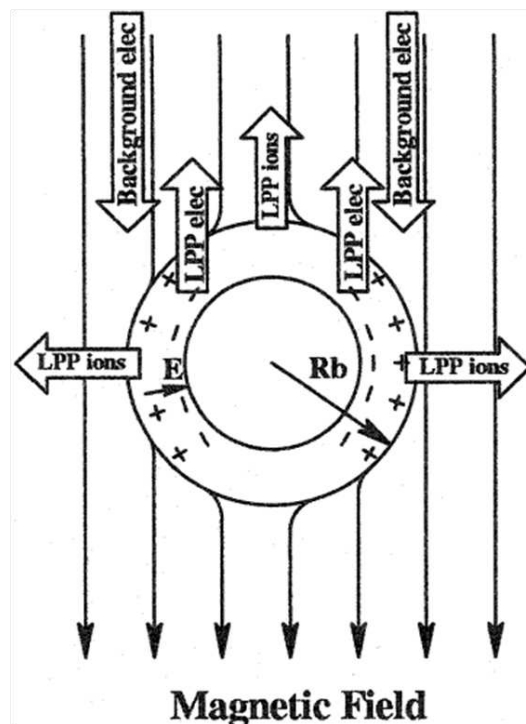


**Figure 2.8:** When a dense laser produced plasma is embedded in an ambient magnetized plasma, electrons (LPP elec) can move away from the diamagnetic cavity while the charge is neutralized by the incoming flow of drifting electrons (Background elec) along the magnetic field line from the ambient plasma. These electrons generate Alfvén waves via Cherenkov radiation. Extracted from [VanZeeland, 2003].

---

---

effect while the electrons from the diamagnetic cavity fly away from the cavity exciting various waves along the magnetic field including Alfvén waves (Figure 2.8). The wave generation by the laser produced plasma can be explained by the classic Cherenkov radiation [Jackson, 1962, Van Compernelle et al., 2008] excited by a pulse of field-aligned suprathermal electrons. High energetic electron pulses are ubiquitous in space, therefore, the similarities between the Alfvén wave generation mechanism via laser produced plasma and the observed astrophysical phenomena were also investigated [Gekelman et al., 2003]. In the given experimental setting, the thermal electron velocity is large compared to the Alfvén speed, being in a kinetic regime with  $v_{th,e} = \sqrt{2k_B T_e / m_e} \gg v_A$ . It corresponds to the surrounding of the Earth at high altitude over four times of the Earth's radius [Stasiewicz et al., 2000]. Here, electrons respond adiabatically to waves and the shear Alfvén wave number gains in transverse direction to the background magnetic field. The associated currents parallel to the magnetic field are carried by electrons while the ions carry currents transverse to the field through the polarization drift [Leneman et al., 1999].

When the dispersive wave becomes nonlinear and interacts with non-resonant very low-frequency perturbations, this interaction induces amplitude modulation and solitons can be formed [Mjølhus and Wyller, 1986, Shukla and Stenflo, 1995]. In theory, the existence of solitons is derived from the nonlinear wave equation and they are expected to have a structure scaled by the ion gyroradius in the perpendicular direction propagating almost in the parallel direction [Hasegawa and Mima, 1976]. The kinetic effects are known also to play a role [Stasiewicz et al., 2000]. In space, singular and localized waveforms with large magnetic perturbations were observed in the auroral processes at the altitude of 600 to 1750 km [Lundin et al., 1995] and named as the solitary kinetic Alfvén waves regarding their form as a strong pulse-like electromagnetic signal [Louarn et al., 1994, Wahlund et al., 1994]. A direct correlation between suprathermal electron fluxes or the generated Langmuir waves and/or whistler waves with the Alfvén wave intensity was detected [Stasiewicz et al., 1997].

---

### 3 Experimental framework

---

At the UCLA, the ongoing studies of collisionless shocks make use of a unique experimental platform that combines the LAPD and the high-energy lasers of the Phoenix Laser Facility. In this scheme, a kJ-class laser irradiates a solid polyethylene target ( $\text{CH}_2$ ) embedded in the LAPD plasma. The dense, energetic laser produced plasma expands in the low-density ambient plasma that fills the LAPD. In the interaction between these two plasmas with different densities, various kinds of waves are generated and cause fluctuations in magnetic and electric fields. The characterization of the perturbed magnetic field is determined by the differentially wound magnetic flux probe [Everson et al., 2009] while the electron emitting probe [Martin et al., 2015] serves as a diagnostic tool for electric field measurement. The LAPD and the Phoenix Laser Facility are introduced in Chapter 3.1 and 3.2, respectively, followed by the introduction of the magnetic flux probe (Chapter 3.3) and the electron emissive probe (Chapter 3.4). Finally in Chapter 3.6, the experimental setup is presented with the corresponding plasma parameters.

---

#### 3.1 Large Plasma Device

---

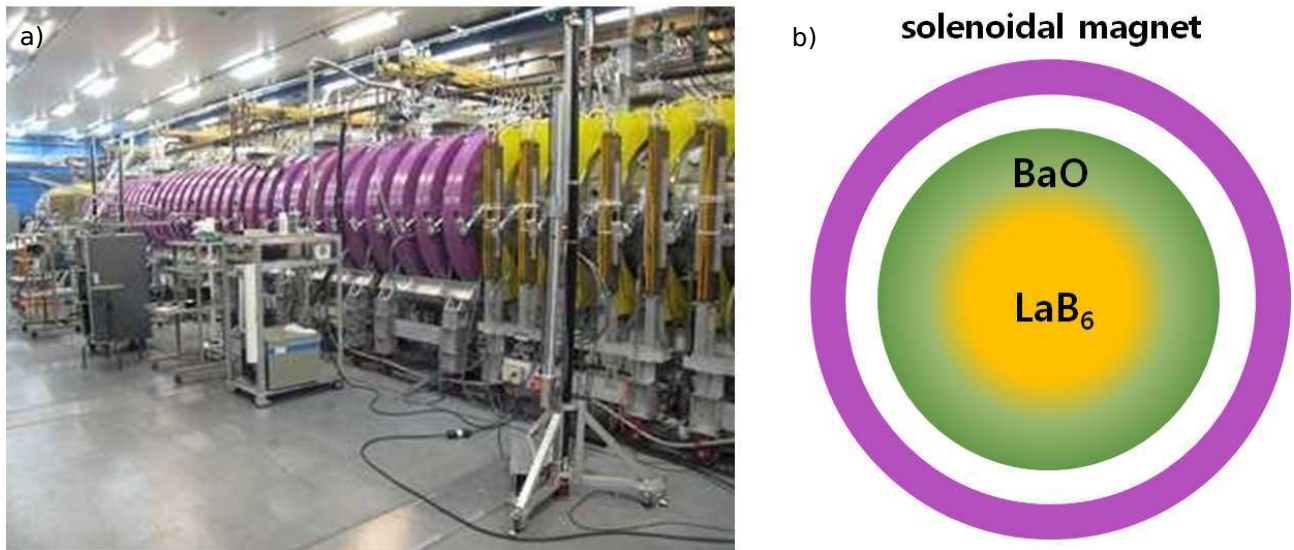


**Figure 3.1:** a) The Large Plasma Device of the Basic Plasma Science Facility at the UCLA constructed in 1991 and upgraded in 2001. The large solenoidal magnets generate an axial magnetic field and various probes can be mounted at radial ports of the vacuum chamber in different angles to measure plasma parameters. b) LAPD plasma density profile created by the  $\text{BaO}$  (green) and the  $\text{LaB}_6$  (yellow) cathode.

The Physics Department of the UCLA owns a very unique plasma device built in 1991 in order to do experiments in the fundamental research area [Gekelman et al., 1991]. The LAPD has an array of 90 solenoidal magnets producing an uniform axial magnetic field. The magnetic field strength can be varied over the range of  $200 \text{ G} \leq B \leq 2500 \text{ G}$  after its upgrade in 2001 [Leneman et al., 2006]. The plasma created in this cylindrical vacuum chamber has a diame-

ter of 60 cm with the total length of 18 m. The pulsed discharge between the barium oxide (BaO) coated nickel (Ni) cathode and a mesh anode at one end of the machine produces a plasma with a density of  $n_i \sim 10^{12} \text{ cm}^{-3}$ . The additional lanthanum hexaborid ( $\text{LaB}_6$ ) cathode [Cooper et al., 2010] with a diameter of  $\sim 20$  cm increases the peak density in the center of the BaO plasma up to one order higher (Figure 3.1). A variety of gases such as H, He, Ar, Ne creates the background plasma while in the presented work H or He was used. The gas is pumped into the LAPD with a typical fill pressure of  $\sim 10^{-5}$  torr. Once the voltage is applied, electrons are accelerated and start to ionize the neutral gas particles. When the plasma is formed, the thermal electrons are responsible for further ionization with the equilibrium duration of about 5 ms, then the plasma is kept steady for another 15 ms. In the end, the bias is removed. This process is repeated every second. The plasma does not carry a net current and the temperature of the ion is  $\leq 1$  eV and that of the electron  $\leq 10$  eV. The LAPD distinguishes itself through its uniform plasma parameters, magnetic field, and high reproducibility of its 1 Hz pulses, as well as its large size which makes it capable of supporting Alfvén waves. The access to the plasma is enabled by mounting the probes at the ports which are found on the surface of the solenoidal magnets in every  $45^\circ$  interval and in different distances from the target. Various probes can be installed to measure the varying plasma parameters.

### 3.2 Phoenix Laser Facility

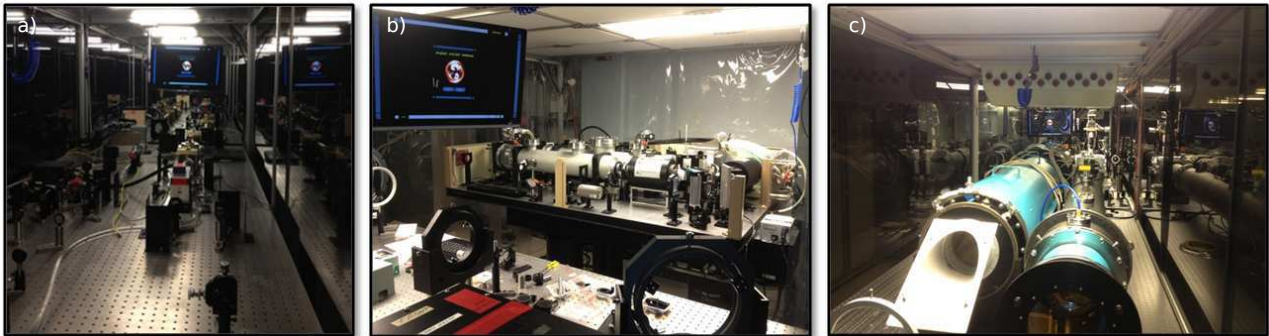


**Figure 3.2:** The Phoenix Laser Facility consisting of three laser systems: a) Phoenix Nd:glass laser with 1064 nm at 5 ns (FWHM) providing 35 J, b) Peening laser with 20 J per pulse, and c) Raptor kJ-class laser with 1053 nm at 25 ns.

In this section, only some important aspects of the lasers and the produced beam properties are listed. More detailed information can be obtained from [Niemann et al., 2012]. The Phoenix Laser Facility is located one floor above the LAPD and hosts three laser systems with the laser energy range from 20 J to 1 kJ: 1) Phoenix Nd:silicate rod laser system with 35 J energy output (5 ns at 1064 nm), 2) Peening, the high-average-power slab laser, with 25 J (25 ns at 1053 nm, repetition rate of 1-6 Hz), and 3) the high-energy laser, Raptor (1053 nm wavelength, in 25 ns pulses, and output energies up to 1 kJ) (Figure 3.2). For the presented experiments, Raptor laser was used at  $\leq 200$  J energy to produce a dense plasma by irradiating a target which is embedded in the LAPD [Niemann et al., 2014, Schaeffer et al., 2014]. The laser intensity on target varied between  $10^{11} - 10^{13} \text{ W/cm}^2$  and the diameter of the focused laser spot on the target can be changed from 1.5 to 3 mm. About 45 min is needed for active cooling so that



there is no energy loss due to the thermal wavefront distortions in the spatial filters, i.e. up to 15 shots can be fired per day.

### 3.3 Magnetic flux probe

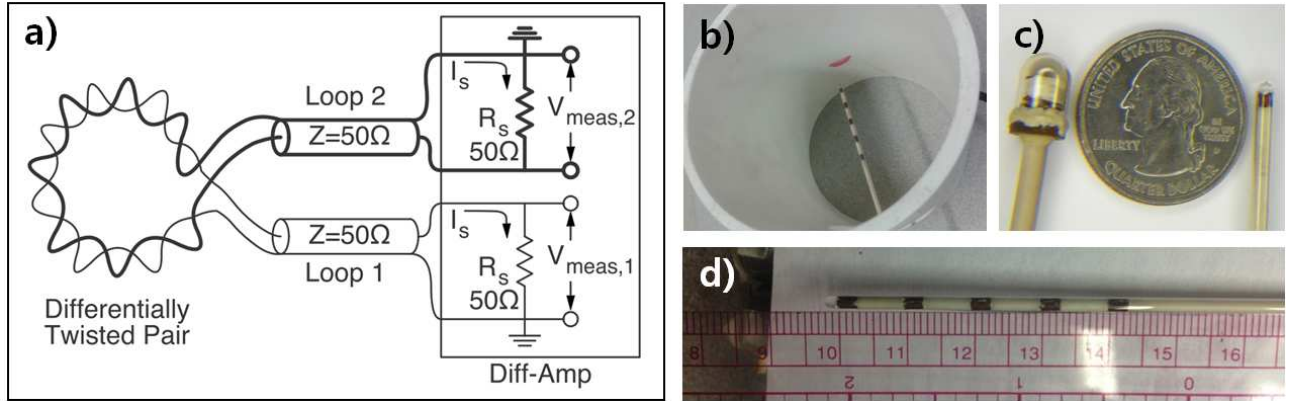


**Figure 3.3:** a) Schematic of the circuit containing a differentially wound twisted pair of loops [Everson et al., 2009]. Loop 1 and loop 2 are biased in opposite direction so that the electrostatic pickups in the signal are subtracted out in the differential amplifier. b) The probe can be calibrated, e.g. using a Helmholtz coil. c) Different-sized probes are used according to the signal power. d) In a 5-tip probe, the five cubes are integrated, which are separated 1 cm apart from each other to enable synchronous magnetic field measurement of a single axis at five different locations.

For our experiment, small probes are required, which are capable of detecting weak magnetic fluctuations (a few Gauss) of high frequency, if necessary along all three axes. In this section, the magnetic flux probe and its basic concept are introduced and the detailed design can be referred to [Everson et al., 2009].

The magnetic flux probe measures the temporal development of the magnetic field during plasma expansion. The principle of the Faraday's law, which means that the temporal change of the magnetic flux is proportional to the total voltage around a closed circuit, is applied to measure the magnetic field perturbation:

$$\oint_{\partial\Sigma} \vec{E} \cdot d\vec{l} = -\frac{d}{dt} \iint_{\Sigma} \vec{B} \cdot d\vec{S} \quad (3.1)$$

where  $\Sigma$  is any fixed open surface with boundary curve  $\partial\Sigma$ . For a small loop, the magnetic field is considered to be constant across the loop area  $S$  so that the measured total voltage is a product of  $S$  and  $dB/dt$ . This is the reason why this probe is also called B-dot probe. To get  $B$ , the measured signal  $dB/dt$  is integrated over time. Usually, a cube is located at the probe tip, around which the copper wires are wound five times along three different axes. In that way, the magnetic field can be measured along all of the three axes at the same time. Just to obtain the magnetic field components, one takes a twisted pair of wire so that the voltage of one wire is biased in opposite direction than the other (Figure 3.3 a). This differentially wound pair of the copper wire detects the induced magnetic field of opposite direction with an equal magnitude

and the electrostatic voltages with the same polarity. Subtracting the signals from each other, the electrostatic part cancels out and the result divided by two is the real magnetic flux. This kind of magnetic probes is made for experiments at frequencies up to about 100 MHz with their size of about 1.25 mm in radius. For measurements far away from the target where the signal becomes weak, a larger probe is deployed which works with the same principle (Figure 3.3 c). In addition to that, a so-called 5-tip probe was developed to ease and quicken the measurement process (Figure 3.3 d). It has in total five differentially wound cubes which are positioned in 1 cm increments. Other than the three-axis probe, the cubes are wound only around one single axis. In our experiment, the 5-tip probe is mainly used to measure the z component of the magnetic field along the x-axis, perpendicular to the axial magnetic field. Prior to every experimental campaign, probes are calibrated by a Helmholtz coil with a known magnetic field (Figure 3.3 b).

### 3.4 Electron emissive probe

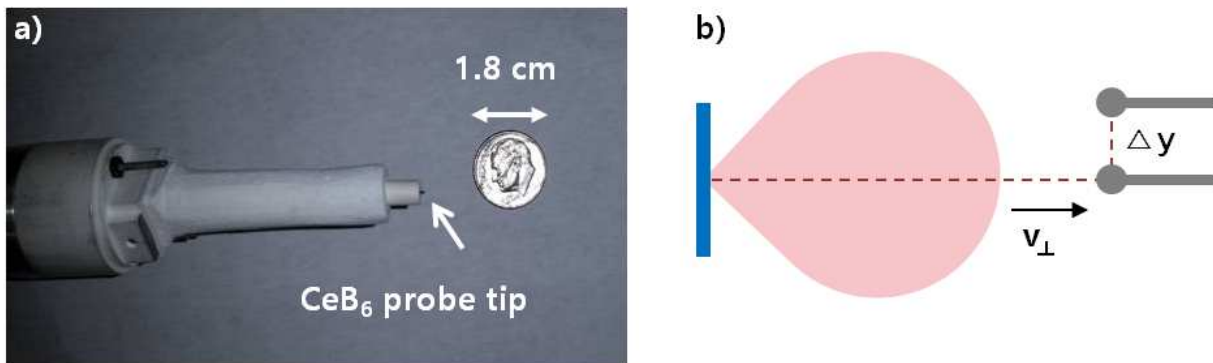


**Figure 3.4:** a) The electron emissive probe used in the experiment is placed next to a dime. The cerium hexaborid ( $\text{CeB}_6$ ) tip is heated and emits electrons until the surrounding potential is equal to the floating potential of the probe (Courtesy of J.Bonde and M.Martin). b) The radial electric field is measured with the electron emissive probe positioned along the blow-off axis while the azimuthal field is obtained from the potential difference along the y-axis at two positions at a distance of  $\Delta y$ .

The electrostatic field  $E$  is one of the essential parameters needed to define the plasma characteristics and can be obtained from the spatial gradient of the electric potential of the plasma  $\Phi_{pl}$ . In 1923, Irving Langmuir first introduced two methods of electric potential measurement using electron collecting and emitting probes [Langmuir, 1923]. Since then, these probes are widely implemented in many plasma physics areas. One of the practical limitations of the electron collecting probes in our experiment is that they do not respond effectively enough to the high frequency variation of the plasma parameters. The sheath formed around the probe tip carries out a capacitive effect and the response of the probe measurement becomes time-dependent because the ions react slower than the electrons during potential swings. In our experiment, a recently developed electron emitting probe is used [Martin et al., 2015]. This kind of electron emissive probe is known to deliver a more accurate electric potential and is already applied for direct potential measurement in different types of plasmas [Kemp and Sellen, 1966, Hershkowitz et al., 1983, Balan et al., 2003, Schrittwieser et al., 2008].



The electron emission is enabled by resistive heating of the probe tip made of cerium hexaboride  $\text{CeB}_6$  (Figure 3.4 a). It has a length of  $\sim 3/4$  mm with a radius of about half mm and is held firmly by carbon tweezers in a silica foam to be isolated from the plasma. For our measurement, the floating potential of the probe  $V_{fl}$  is used to overcome the limitation of slow tracking of the electric potential in case of the electron collecting probes. The relation between the plasma and probe potential is noted as follows,

$$\Phi_{pl} = V_{fl} + \alpha \frac{T_e}{e} \quad (3.2)$$

where  $T_e$  is the electron temperature,  $e$  the elementary charge, and  $\alpha$  a constant depending on the sheath characteristics.  $\alpha$  is determined either experimentally or using a theoretical model. In contrast to electron collecting probes, an emissive probe emits electrons generating current comparable to the electron saturation current and tries to reach the point where the electron flux of the probe equals the flux of the plasma,  $(n_e v_e)_{plasma} \approx (n_e v_e)_{probe}$ . When the potential of the probe equals the electric potential of its surroundings, the current through the probe falls to zero.

The radial and azimuthal electric fields can be obtained in two different ways (Figure 3.4 b). First, the radial field  $E_r$  is obtained from the following equation:

$$E_r \triangleq E_x = -\nabla \Phi_{pl} - \frac{\partial A_x}{\partial t} = -\frac{d\Phi_{pl}}{dt} \frac{1}{v_{\perp}} - \frac{\partial A_x}{\partial t} \quad \text{with} \quad \nabla^2 A_x = -\frac{\partial B}{\partial y} \quad (3.3)$$

where  $v_{\perp}$  is the perpendicular expansion velocity of the laser produced plasma and  $A_x$  the x component of the vector potential, also called the induced term. The azimuthal field is the difference between two electric potentials along the y-axis at a distance of  $\Delta y$ . Due to the limited number of possible laser shots during experimental campaigns,  $\Delta y$  was set to  $\gtrsim 2$  cm indicating a large error in the calculated azimuthal electric field.

The electron emissive probe works well at the plasma densities of the presented experiment. The benefit of using this probe instead of the collecting probe is that it is not affected as much by the density fluctuations or drift waves resulting from the density gradient [Schrittwieser et al., 2008, Martin et al., 2015]. The experimental results of the electric potential measurement using the presented emissive probe are provided in Chapter 4.1.2.

---

### 3.5 Fast photography

---

Using a fast photography, the kinetics of expanding plasmas can be studied, especially its cross-field expansion speed, spatial development, and its shape from particle self-emission, which are eventually compared to probe measurements. In this experiment, an image-intensified charge-coupled device (ICCD) camera (PI-Max from Princeton Instruments Acton) [Princeton\_Instruments, 2015] is used for a high resolution photography. It is an ideal tool for time-resolved imaging and spectroscopy with its gate widths in sub-nanoseconds and high sensitivity for the selected region of the spectrum. With the exposure time set to 25 ns, the pictures were taken at various time delays after the laser irradiation to follow the temporal plasma evolution and a spatial resolution of a few cm is possible. The spectral filters enable the unwanted plasmas segregated from the specific plasma species which is to be displayed. In our experiment,

a filter of the wavelength 494.4 nm is applied for the debris plasma ( $C^{+4}$ ) and that of 468.6 nm for the background ( $He^{+}$ ). The camera is installed a few meters away from the target location along the magnetic field.

---

### 3.6 Experimental setup

---

In several experimental campaigns, the plasma density, the species of the filling gas, the magnetic field strength, and the laser energy were varied to study their effect on the plasma expansion as well as the interaction with the surrounding magnetized plasma. The kJ-laser of the Phoenix Laser Facility focused onto a target into the LAPD plasma. The target is located at  $(x, y) = (30 \text{ cm}, 0 \text{ cm})$  in the LAPD coordinate system. The laser beam is at an angle of several degree relative to the target normal to avoid retro-reflections, but the blow-off direction of the expanding plasma is perpendicular to the magnetic field and the target normal is in the negative x-direction (Figure 3.5). The target motion is computer-controlled and programmed so that a fresh surface of the target is used after every shot via translation and rotation. Either a magnetic flux probe (e.g., the 5-tip probe) or an electron emissive probe is placed on the opposite side of the target to measure the field expulsion across the axial magnetic field. Additionally, an ICCD-camera is set a few meters away from the target to take pictures of plasma expansion in the x-y plane. To detect the generation of hydromagnetic waves, an array of magnetic flux probes is also mounted along the magnetic field. The location of the parallel probes differs in each experiment. The signals are recorded using custom-built 150 MHz differential amplifiers and 1.25 GHz 10-bit digitizers.

---

Density of LAPD plasma	$10^{12} \text{ cm}^{-3} \leq n_i \leq 2.5 \times 10^{13} \text{ cm}^{-3}$
Temperature	$T_i \sim 1 \text{ eV}, T_e \sim 5 \text{ eV}$
Magnetic field	$200 \text{ G} \leq B \leq 1500 \text{ G}$
Laser energy	$50 \text{ J} \leq E \leq 200 \text{ J}$
Diamagnetic cavity size	$30 \text{ cm} \leq L \leq 50 \text{ cm}$
Ambient plasma species	H, He

---

**Table 3.1:** Characteristic plasma parameters of the experiments

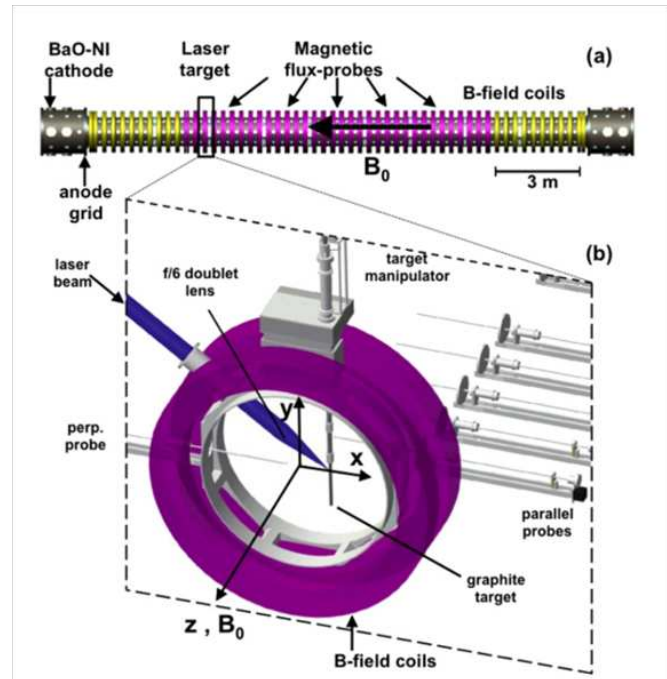
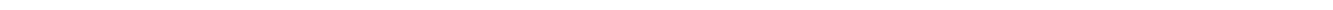


**Figure 3.5:** Left: The setup of the final focusing lens for Raptor laser beam injection into the LAPD. Right: Three-dimensional layout of the experiment performed inside of the LAPD. The laser beam irradiates the graphite or high-density polyethylene ( $C_2H_2$ ) target which is located 30 cm off the LAPD-coordinate center and creates a dense plasma that expands into the tenuous ambient plasma in the LAPD. Probes are placed either across (perpendicular probe) or along the field (parallel probes) and measure magnetic and electric field fluctuations. Extracted from [Niemann et al., 2013].



---

## 4 Experimental results

---

The laser experiments were carried out at the LAPD at the UCLA to investigate the diamagnetic cavity created by a laser produced plasma which expands into a ambient low-density plasma across the externally applied magnetic field. This diamagnetic cavity is capable of generating a magnetosonic pulse along the blow-off axis, which can develop into a shock, but also radiate Alfvén waves throughout the ambient plasma along the magnetic field. The presented results are obtained from four different experimental campaigns performed with varying plasma parameters. Hydrogen ( $m_i = 1$ ) and helium ( $m_i = 4$ ) were used as background plasma species, the background density was varied from  $10^{12}$  to  $2.5 \times 10^{13} \text{ cm}^{-3}$ , and the magnetic field between 200 and 1500 G. The laser was shot on target at energies starting from 50 J up to 200 J. The results can be compared to similar works in the past where  $E_{laser} \leq 30 \text{ J}$  [VanZeeland et al., 2001, VanZeeland et al., 2003, VanZeeland and Gekelman, 2004, Collette and Gekelman, 2010, Niemann et al., 2013]. The magnetic field data either across or along the magnetic field was acquired using magnetic flux probes while the electric field was only measured across the magnetic field via the electron emissive probe. Unless otherwise mentioned, the coordinate system is centered at the laser impact point on the target, which is  $(x, y) = (30 \text{ cm}, 0 \text{ cm})$  in LAPD-coordinates.

---

### 4.1 Dynamics of the diamagnetic cavity

---

A laser produced plasma expands into a magnetic field creating a diamagnetic cavity with a radius  $R_c$  and can subsequently launch a magnetosonic pulse across the magnetic field. To study the dynamics of the diamagnetic cavity as well as the pulse, a number of experimental runs were done on the LAPD. Under certain circumstances, the diamagnetic cavity acts as a piston driving a perpendicular shock. The detailed study of the shock formation in a laboratory setting can be found in [Schaeffer, 2014, Schaeffer et al., 2014, Niemann et al., 2014]. Here, the diamagnetic cavity structure, its expansion through the plasma, the dependence on the surrounding magnetic field and the laser energy are evaluated. Additional lines of data were taken at  $y = 0 \text{ cm}$  and  $z = 28 \text{ cm}$  using a 3-axis magnetic flux probe to investigate the expansion of the diamagnetic cavity along the magnetic field at different magnetic field magnitudes. Additionally, the electrostatic potential and the electric field were measured directly at the cavity edge with the electron emissive probe. The electric field measurement provides instability-like features at the cavity edge of the expanding plasma.

---

#### 4.1.1 Magnetic field measurements

---

Shown in Figure 4.1 a) is a contour plot of the magnetic field measurement at 275 G in a helium plasma along the x-axis. The laser energy was 130 J and the blow-off velocity of carbon ions was  $180 \text{ km/s} \approx 1.35 v_A$ , which is derived theoretically from  $v_{blow-off} = 250 \times \Phi_a^{0.2} \text{ km/s}$  where  $\Phi_a$  is the absorbed laser intensity in  $10^{12} \text{ W/cm}^2$  [Grun et al., 1981, Key et al., 1983, Meyer and Thiell, 1984]. This derived velocity is mostly consistent with the measured velocity of the magnetic pulse. Only the z component of the magnetic field was measured and shown

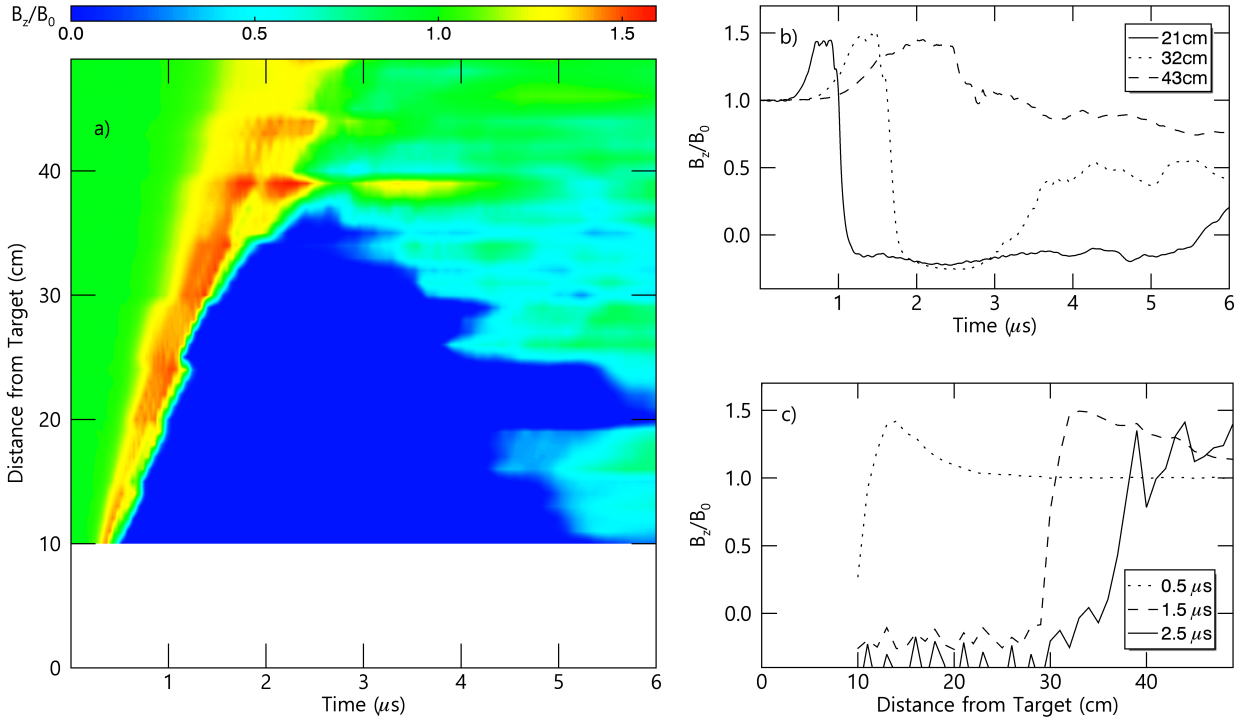


**Figure 4.1:** a) Contour plot of the  $z$  component of the magnetic field at 40 spatial locations along the  $x$ -axis, collected over eight laser shots ( $E_{laser} \sim 130$  J) using the 5-tip magnetic flux probe. The ambient plasma is helium and the external magnetic field is 275 G. The magnetic compression propagates at a velocity of about  $1.5 M_A$  with its maximum compression a factor of 1.5 higher than the initial value. It precedes the diamagnetic cavity which fully expels the inner magnetic field and reaches a diameter of about 37 cm. Near the target, the diamagnetic cavity begins to collapse as the background field diffuses in around  $t = 6 \mu s$  although the lifetime of the cavity is shorter farther away. b)  $B_z$  at three different positions. The magnetosonic pulse reaches the probe prior to the fully expelled magnetic cavity. Broadening of the magnetic pulse is apparent due to the velocity dispersion with increasing distance from the target and possibly by Landau damping. When the probe is placed at a position  $> 37$  cm, beyond the maximum size of the diamagnetic cavity, one only measures the magnetic field compression propagating across the field. c) Profile of the diamagnetic cavity at three different times after the laser irradiation. It expands until it reaches its peak diamagnetism with  $2R_c \approx 37$  cm at  $\tau_{peak} = 2.5 \mu s$ .

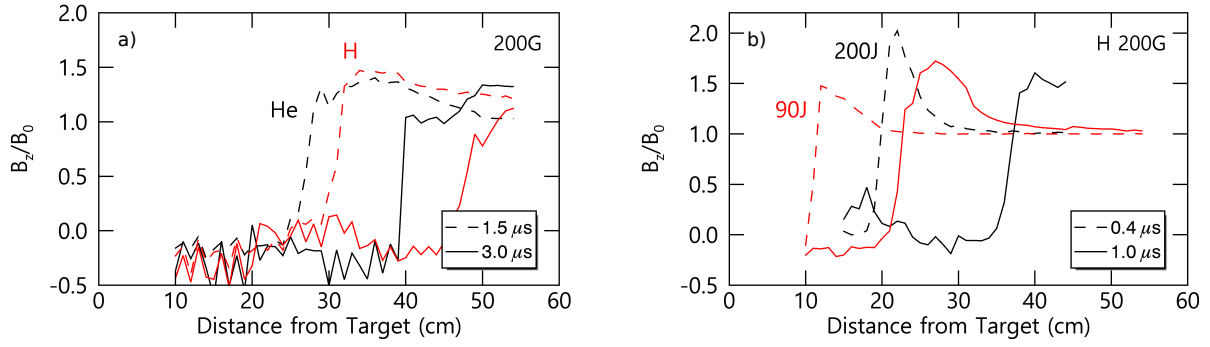


**Figure 4.2:** Comparison of diamagnetic cavity size in a) different background plasma: hydrogen (red) and helium (black), and b) different laser energy: 90 J (red) and 200 J (black) in a hydrogen plasma, both at 200 G.

because the magnitude of the transverse components,  $B_x$  and  $B_y$ , are small compared to  $B_z$  in the regime of interest. To obtain this plot, eight laser shots were needed and data were collected at 40 different locations along the blow-off axis from the target. The contour plot demonstrates the formation of the diamagnetic cavity which is preceded by the super-Alfvénic magnetosonic pulse with  $v \approx 200 \text{ km/s} \approx 1.5 v_A$  and whose maximum compression is a factor of about 1.5 above background. Although the ratio of the magnetic field and the velocity between the upstream and downstream region is on the same order fulfilling the Rankine-Hugoniot conditions according to the Equation 2.9 (only partly because the ion density ratio  $n_u/n_d$  is not known), the length of the pulse was below the ion inertial length ( $\sim 20 \text{ cm}$ ) and did not steepen or develop into a shock. Instead, as the pulse propagated away from the target, it dissipated and broadened due to the changing ambient plasma conditions. The diamagnetic cavity size reached its maximum size of  $2R_c \approx 37 \text{ cm}$  at  $t \approx 2.5 \mu\text{s}$ , which is defined as the time of peak diamagnetism  $\tau_{peak}$ . Then the background magnetic field started to diffuse back into the cavity. The cavity lifetime  $\tau_c$  depends on the parameters such as collisionality, the ion Larmor-radius, or the electron skin-depth [Kacenjar et al., 1986, Dimonte and Wiley, 1991] and is always small compared to the classical magnetic diffusion time

$$\tau_{md} = \mu_0 \sigma R_c^2 \quad \text{with} \quad \sigma = \frac{50 \epsilon_0^2 \sqrt{\pi (k_B T_e)^3}}{\sqrt{m_e} e^2 Z \ln \Lambda} \quad (4.1)$$

where  $\sigma$  is the Spitzer conductivity and  $\ln \Lambda$  the Coulomb logarithm.  $\tau_{md}$  is theoretically derived from pure resistivity of the magnetic field. With  $T_e = 5 \text{ eV}$  and the cavity radius of  $R_c = 18 \text{ cm}$ , the calculated value  $\tau_{md} \approx 740 \mu\text{s} \gg \tau_c = 6 \mu\text{s}$ . The discrepancy between these two values might be caused by the irregular and broad magnetic structure which is correlated with the plasma instability at the cavity edge [Dimonte and Wiley, 1991] or other various effects participating in the diamagnetic cavity generation process, such as magnetic field oscillations inside the cavity.

In earlier experiments with low laser energy of  $\sim 1 \text{ J}$ , the magnetic field inside the diamagnetic cavity was not fully expelled and the cavity depth decreased linearly with the increasing magnetic field [VanZeeland et al., 2003, Collette and Gekelman, 2010]. The laser energy of  $\sim 30 \text{ J}$



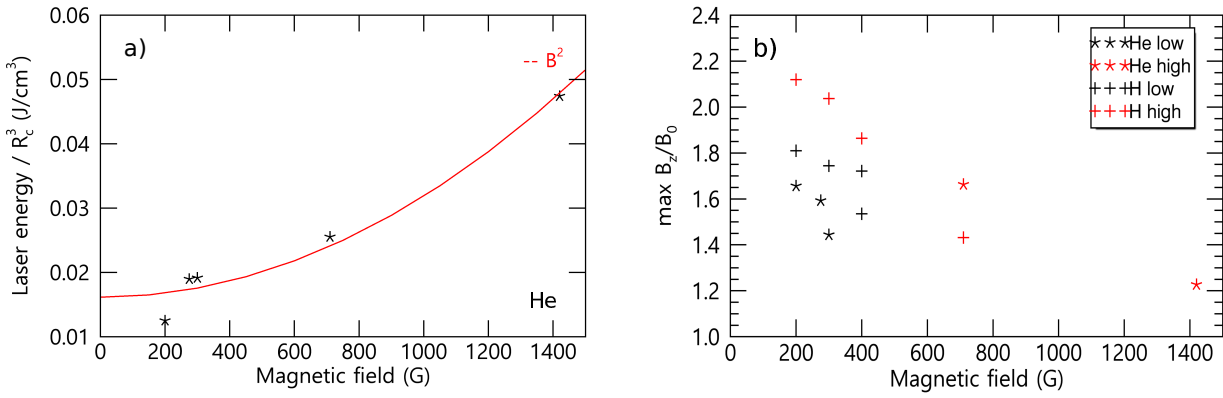


**Figure 4.3:** a) The relation between laser energy, diamagnetic cavity size, and magnetic field in a helium plasma. The red line is the quadratic scaling fit to the magnetic field, assuming a spherical expansion of the diamagnetic cavity. b) Experimentally derived magnetic field compression in helium (\*) and hydrogen plasma (+) in high ( $\sim 200$  J, red) and low ( $\sim 100$  J, black) laser energy regime as a function of the external magnetic field. A linear decrease of the magnetic compression is shown for rising magnetic field magnitude.

succeeded in full expulsion of the magnetic field out of the cavity [Niemann et al., 2013] and in the energy regime of  $\geq 50$  J, as performed in the scope of this work, every diamagnetic cavity expelled the magnetic field completely along the x-axis. Sometimes the field expulsion also reached below zero. This occurrence is not clearly understood, but the bulk of debris ions inside the cavity or its interaction with the background ions could be involved in this incident. It is also observed in the numerical simulation (Chapter 5.2).

The general behavior of the cavity expansion is the same for every laser shot although the presence of background plasma or varying laser energy affects the cross-field speed of the expanding plasma and the formation of micro-turbulence inside or at the edge of the cavity, and thus the diamagnetic cavity size. It is already known that a high external magnetic field inhibits the cavity size from growing. The expansion speed of the cavity, therefore, becomes slower because the high magnetic field not only decreases the ion gyroperiod, but also the transit time. In a background plasma of heavier species, here helium, the cavity did not only move slower than in lighter hydrogen plasma (Figure 4.2 a), but also the size of the cavity at the time of peak diamagnetism (both at  $\tau_{peak} \approx 3 \mu s$ ) is slightly smaller. Higher laser energy causes more particles to be ablated from the target and greater blow-off velocity. As more ions escape at an even faster velocity, the electric field and the cross-field current increase resulting in the enhancement of micro-instabilities at the cavity edge, the magnetic field amplitude, and the cavity expansion speed. A significant increase in the peak magnitude and the cavity size is visible (Figure 4.2 b).

In Figure 4.3 a), the relation between the laser energy, the cavity radius, and the external magnetic field is shown. For this purpose, the cavity size is defined as the distance from the target to the point where the magnetic field of the cavity edge is 80 % of its initial value at the time of the peak diamagnetism. The half of this distance is the cavity radius  $R_c$ . The magnetic field magnitude in experiments with an ambient helium plasma scales as  $B^2$ , consistent with the previous experiments [VanZeeland and Gekelman, 2004, Niemann et al., 2013].



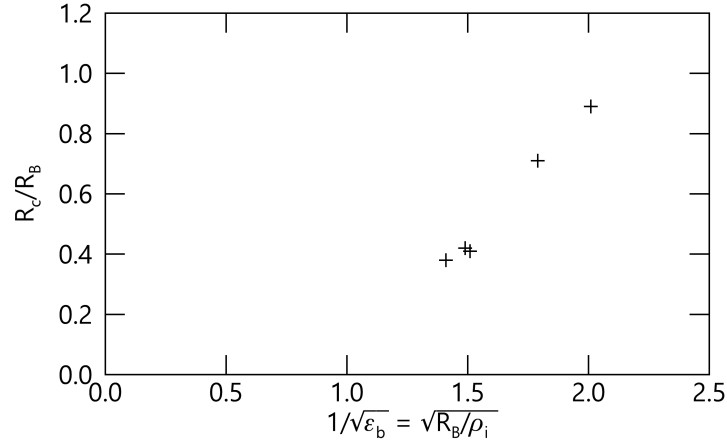


**Figure 4.4:** Dimensionless relationship between of the cavity radius  $R_c$  and the magnetic stopping radius  $R_B$  as a function of the ion magnetization  $1/\epsilon_b = R_B/\rho_i$ . If  $R_c \approx R_B$ , the cavity can be considered to be sufficiently decelerated by the magnetic field. The displayed results are from experiments performed in a helium plasma at different magnetic field magnitudes.

It is also expected from the energy conservation equation (Equation 2.4), where a spherical expansion of plasma is assumed. A number of experiments was also performed in the hydrogen background, but the cavity size sometimes exceeded the measurement range (up to about 50 cm from the target) so that the cavity edge could not be determined. The magnitude of the compressed magnetic field at the cavity edge can be also described as a function of the background magnetic field (Figure 4.3 b). To make a reasonable comparison, the experimental results were divided into four groups according to the background species and the laser energy. The low energy indicates laser energy of about 100 J and the high energy from 180 to 200 J. The maximum peak is normalized to the initial background field. For increasing field magnitude, the peak compression decreases linearly in all four cases. Despite the consistency in the linear decrease, however, one cannot attribute this tendency to a single parameter as the peak compression also depends on the blow-off speed [Niemann et al., 2013] or the density of the ambient plasma [Schaeffer et al., 2014]. The coupling efficiency is a complex parameter which cannot be determined by changing one or two plasma parameters. Moreover, a different result is achieved according to the way of the plasma is described. As from [Hewett et al., 2011], an expanding plasma dealt kinetically in a numerical simulation is poorly confined with increasing plasma density while, in MHD picture, the background ionization leads to more mass in the background that stops the debris more quickly leading to an efficient coupling. This cross-field dispersal of the debris ions is smaller in the MHD than in the kinetic regime. Besides, the slowing down of the cavity is mainly affected by the cavity-ambient plasma in the super-Alfvénic case while for low Mach number, the cavity loses energy due to jet or magnetic field deformation [Berezin et al., 1998]. For effective energy and momentum transfer from the debris to the ambient plasma, a plasma with density exceeding a certain threshold value is needed [Clark et al., 2013].

In experiments performed in vacuum [Zakharov, 2003], the coupling of the diamagnetic cavity to the background magnetic field is proved to be influenced by the ion magnetization

$B$	$R_c$	$E_c/E_{laser}$	
200 G	20 cm	5.3 J / 100 J	~ 5.3 %
275 G	11 cm	1.3 J / 26 J	~ 6.5 %
275 G	19 cm	8.7 J / 130 J	~ 6.7 %
300 G	17 cm	7.8 J / 100 J	~ 7.8 %
710 G	19 cm	57.7 J / 160 J	~ 36.0 %
1420 G	15 cm	113.7 J / 160 J	~ 70.8 %

**Table 4.1:** Energy conversion efficiency of diamagnetic cavity in a helium plasma at different background magnetic fields. High efficiency is apparent at higher magnetic field. The result in the second row is from [Niemann et al., 2013].

$\epsilon_b = \rho_i/R_B$ . The laser produced plasma is sufficiently decelerated by the magnetic field only for  $1/\epsilon_b \geq 1$  where  $R_c \approx R_B$ . Otherwise, the effectiveness of the interaction between the dense plasma and the background magnetic field reduces due to the lower-hybrid turbulence [Zakharov et al., 1986] or MHD Rayleigh-Taylor-flute instabilities [Zakharov et al., 2003]. In the presence of ambient plasma, the effectiveness of diamagnetism will further decrease. Figure 4.4 shows the dimensionless relationship between  $R_c$  and the level of ion magnetization  $\epsilon_b$  of different diamagnetic cavities generated in our experiments. As one needs to know the cavity size for this comparison, only those expanding in helium plasma are taken into consideration. Although the results have the tendency reaching  $R_c/R_B = 1$  for increasing magnetic field strength, the efficient coupling to the magnetic field occurs at about  $1/\epsilon_b \geq 2$ , higher than the results in vacuum (cf. Figure 1 in [Zakharov, 2003]). It indicates that the debris particles do not contribute to the diamagnetic cavity as much as in vacuum when an ambient plasma is present, but slip through the cavity without being coupled to the background magnetic field. The ambient plasma affects the diamagnetism.

Table 4.1 shows the energy coupling efficiency of diamagnetic cavities compared to the laser energy at different background field magnitudes. The efficiency displays a clear dependency on the background magnetic field. It is below 10 % under 300 G, but increases almost up to 70 % for higher magnetic field, consistent with the result shown in Figure 4.4. In higher magnetic field, the Larmor-radius of debris ions is larger, thus the most of the blow-off energy is used to expel the magnetic field instead of accelerating the ions in the ambient plasma. The energy conversion efficiency seems to be independent of the laser energy as is the case at 275 G for 26 J and 130 J. As already mentioned, the diamagnetic cavity expelled the inside magnetic field fully already at  $\sim 30$  J, apparently reaching the saturation point. A more accurate study of coupling efficiency, not provided in this work, could be done with, e.g. ambient ion velocity measurement, which can be compared to the plasma expansion in vacuum so that the energy given to the surrounding plasma can be determined.

In low magnetic field  $\leq 400$  G, the magnetic cavity diffused back once it had reached its peak diamagnetism (Figure 4.5 a and b). During the collapse of the cavity, variations in the field components were seen, sometimes comparable to the ambient field (Figure 4.5 a), probably caused by geometrical effects. When a higher laser energy was applied, the diamagnetic cavity lifetime was shorter. Experimentally, a full separation of the diamagnetic cavity from the target

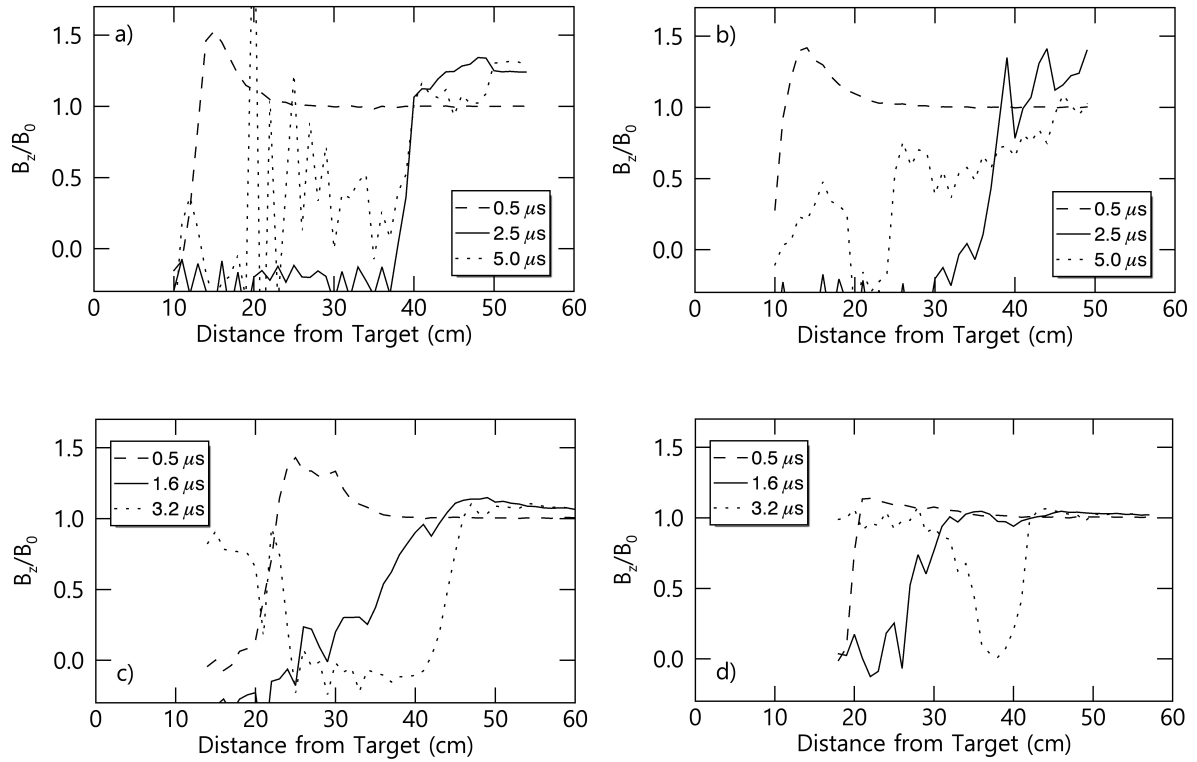


**Figure 4.5:** Spatial development of diamagnetic cavity at four different magnetic field magnitudes: a) 200 G, b) 275 G, c) 710 G, and d) 1420 G. These were all performed in a helium plasma and the laser energy was 100 J for a) and b), 160 J for c) and d). The maximum diamagnetic cavity reached at  $\tau_{peak}$  is demonstrated in straight line and compared to the cavity structure before (dashed) and after  $\tau_{peak}$  (dotted). The separation of the diamagnetic cavity from the target is only observed for high magnetic field experiments,  $B \geq 710$  G.

could be observed in higher magnetic fields, at 710 and 1420 G (Figure 4.5 c and d) with the laser energy of  $\sim 160$  J. The rear cavity edge close to the target propagated across the field in both cases while for 1420 G, the cavity lifetime was about half of that at 710 G. Both cavities travelled a distance of about 50 cm from the target. The high magnetic field experiments were performed, however, in slightly different background conditions than other experiments. The difference was not only the higher range of the magnetic field, but also the plasma density in the surrounding. The BaO cathode was turned off and the plasma in the LAPD was only created by the LaB<sub>6</sub> cathode producing a smaller plasma. The target was outside the plasma and the diamagnetic cavity initially produced in vacuum travelled into the plasma region. The observed trailing separation might have been caused by this fact.

Regardless of the applied magnetic field strength, the ambient plasma species, or the laser energy, the frequency spectrum could be divided into four groups for every measurement (Figure 4.6):

- I)  $f \leq \sim 300$  kHz existed even longer than the cavity lifetime,
- II)  $\sim 300$  kHz  $\leq f \leq \sim 1$  MHz disappeared with the cavity,

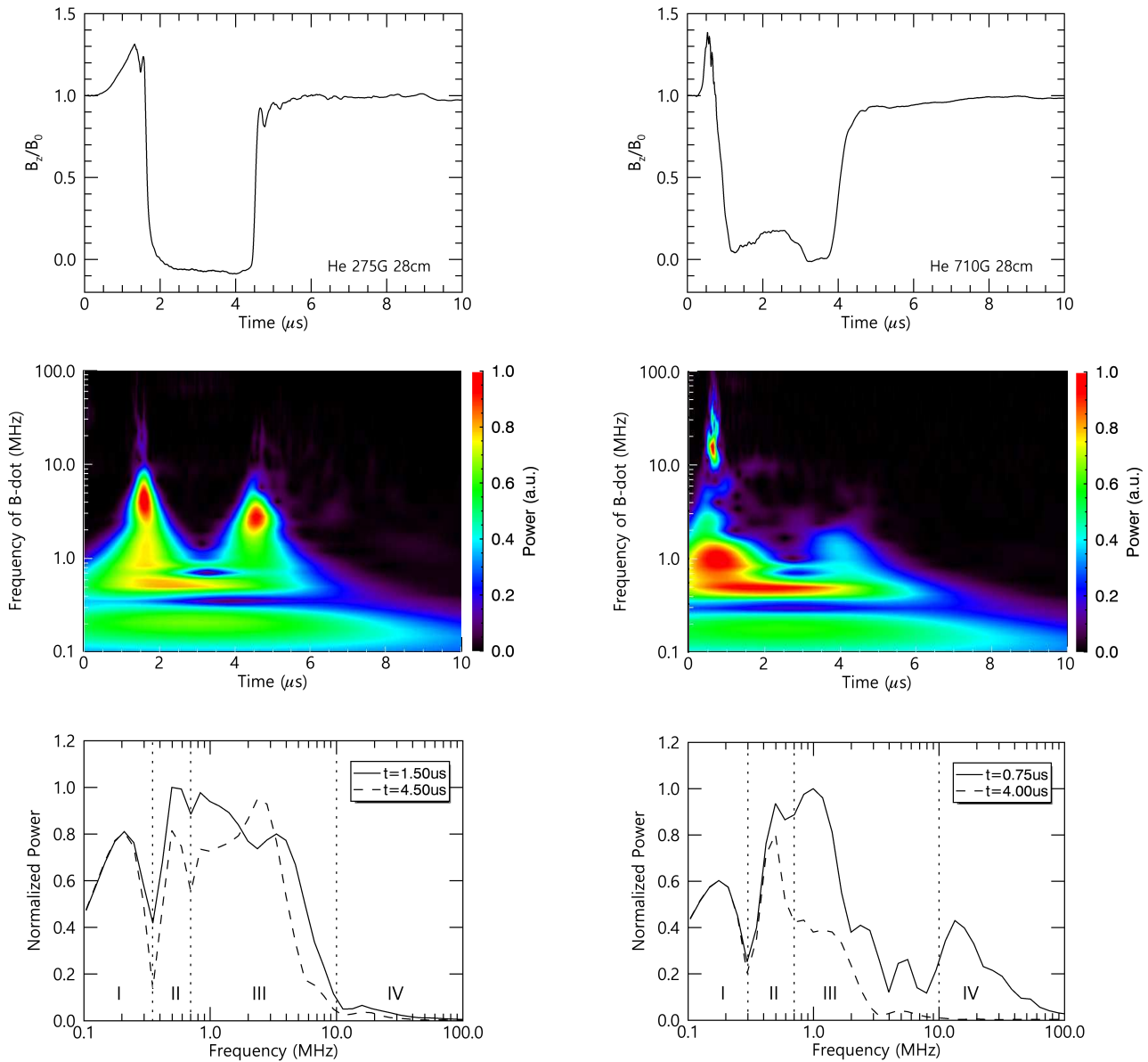


**Figure 4.6:** Upper panel: Temporal evolution of the time-integrated magnetic field fluctuations at  $x = 28$  cm with different external magnetic field strength and laser energy in a helium plasma - 275 G at 130 J (left) and 710 G at 160 J (right). Middle panel: Auto-spectrum for magnetic field fluctuations. Lower panel: I) the oscillations  $\leq \sim 300$  kHz seem to be present in the background regardless of the presence of the cavity while II) the fluctuations from  $\sim 300$  to  $\sim 700$  kHz are present inside the cavity. III) Those of  $\sim 700$  kHz  $\leq f \leq \sim 10$  MHz at the cavity edge and IV) high frequency oscillations  $\geq \sim 10$  MHz arise mostly at the magnetic compression.

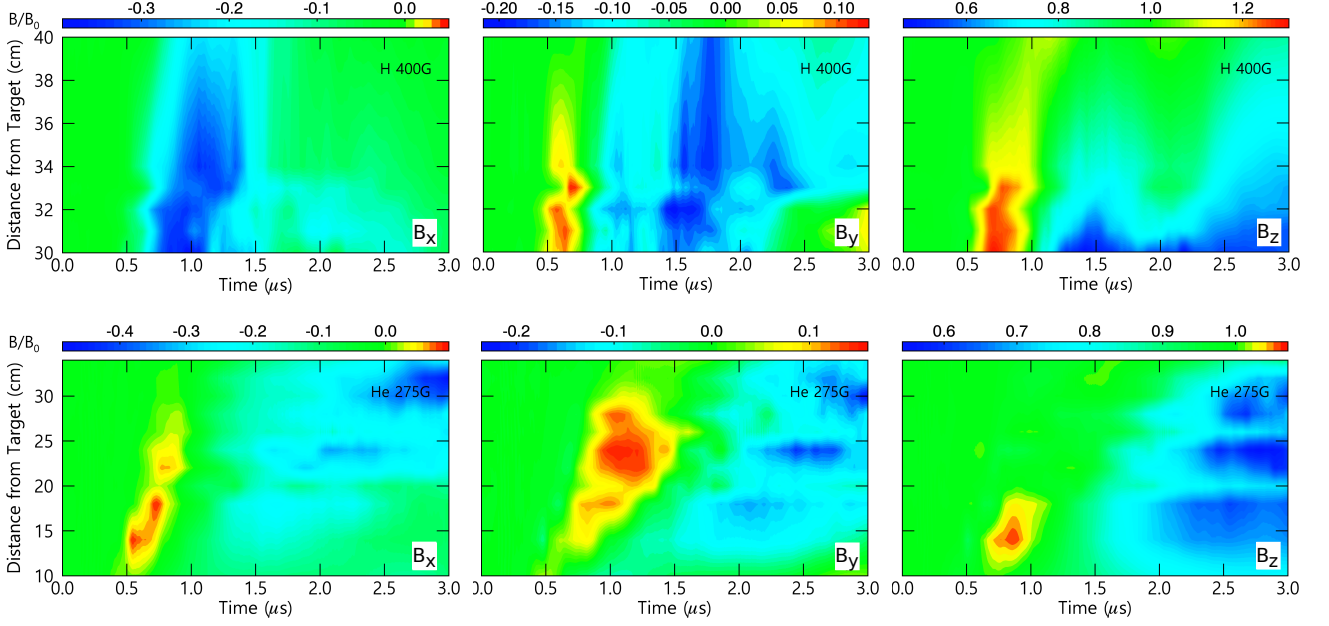


**Figure 4.7:** Magnetic field contour plots of diamagnetic cavity expanding in a hydrogen plasma at 400 G (upper) and helium plasma at 275 G (lower) measured at  $z = 28$  cm away from the target along the magnetic field. Despite the different magnetic field strength and the ambient plasma species, the only apparent disagreement is that the compression in  $B_x$  is negative in hydrogen plasma, which could be related to the different location of the probe along the  $x$ -axis. In contrast to the diamagnetic cavity measurement at  $z = 0$  cm, the cavity in  $B_z$  is not fully expelled.

III)  $\sim 1 \text{ MHz} \leq f \leq \sim 10 \text{ MHz}$  appeared at the cavity edge, both in the front and the back, and  
 IV)  $f \geq \sim 10 \text{ MHz}$  arose at the magnetic compression.

It is assumed that the low-frequency region (I and II) were caused by the background oscillations due to the ambient or debris particles ( $f_{ci,a,275G} = 105.5 \text{ kHz}$ ,  $f_{ci,d,275G} = 140.7 \text{ kHz}$  and  $f_{ci,a,710G} = 272.4 \text{ kHz}$ ,  $f_{ci,d,710G} = 363.2 \text{ kHz}$  where  $f_{ci,a}$  and  $f_{ci,d}$  are the cyclotron frequency of the ambient  $a$  and debris ions  $d$ ) and the high frequency regions (III and IV) by the lower-hybrid frequency ( $f_{LH,275G} = 9 \text{ MHz}$  and  $f_{LH,710G} = 23.2 \text{ MHz}$ ) indicating the existence of a strong cross-field current. But IV regime does not appear at every cavity edge for unknown reason.

Although the assumption of the spherical plasma expansion seems to match and is practically used in theory because of its simple shape, in reality, a deformed plasma is expected due to the non-uniformity of the laser spot on the target [Schaeffer, 2014], the effect of the applied magnetic field, and the magnetic confinement causing straight plasma flows [Plechaty et al., 2013]. To study the parallel expansion of the cavity, the magnetic field was measured along the  $x$ -axis at  $z = 28$  cm using a 3-axis magnetic flux probe to obtain other transverse components of the magnetic field, which were neglected for perpendicular propagation measurement at  $z = 0$  cm. The upper panel in Figure 4.7 is for hydrogen plasma at 400 G and the lower for helium at 275 G. The overall behavior of the field is the same, independent of the species or the strength of the magnetic field. As the diamagnetic cavity now expands obliquely at  $z = 28$  cm, the magnetic compression as well as the expulsion of the field can be detected in all three axes of the

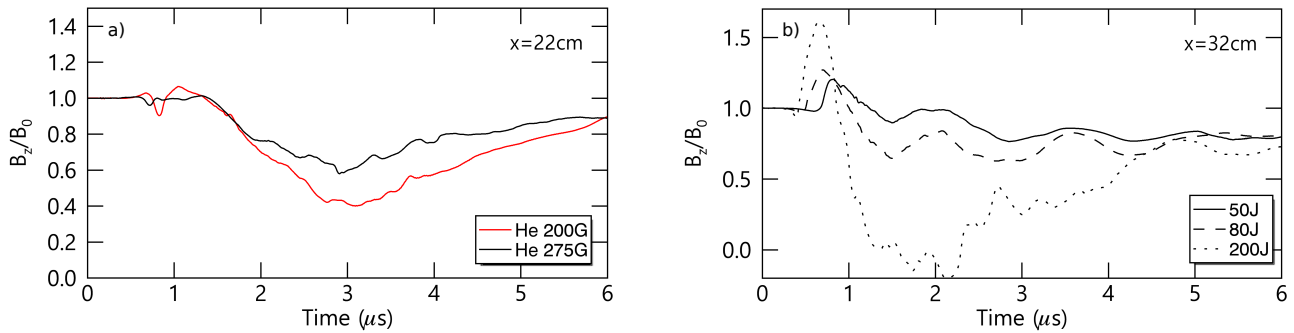


**Figure 4.8:** Depth of the diamagnetic cavity at  $z = 28$  cm seems to depend on a) the external magnetic field strength and b) the laser energy. b) is from the data measured at 400 G in a hydrogen plasma. Full expulsion of the field is only observed at laser energy above 160 J. The peak arrival occurs sooner for higher energy.

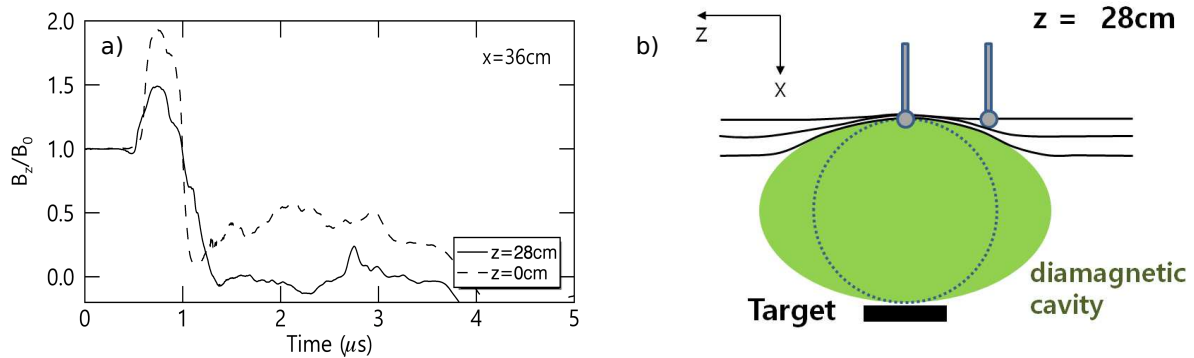


**Figure 4.9:** a) Temporal change of  $B_z$  at  $(x, z) = (36 \text{ cm}, 28 \text{ cm})$  and  $(x, z) = (36 \text{ cm}, 0 \text{ cm})$  are compared. The magnetic compression at  $z = 28$  cm arrives simultaneously with the pulse at  $z = 0$  cm despite the longer distance from the target. b) An elongated shape of the diamagnetic cavity in the  $x$ - $z$  plane is expected instead of a sphere.



probe. Similar to the magnetic field data ( $B_z$ ) at  $z = 0$  cm, the diamagnetic cavity is preceded by the magnetic compression. The negative trough in  $B_x$  is due to the position of the probe along the  $x$ -axis. For a large  $x$ ,  $B_x$  is compressed towards the negative  $x$  in the LAPD coordinates. In contrast to the perpendicular magnetic field measurement, the cavity depth seems to be affected by the magnetic field as well as the laser energy in this region. The cavity depth is anti-proportional to the applied magnetic field magnitude (Figure 4.8 a) and the full expulsion of the field is only observed for laser energy  $\geq 160$  J (Figure 4.8 b). Moreover, the arrival time of the compression for higher laser energy is also shorter, same as the case at  $z = 0$  cm. One interesting feature to be noted is that the arrival times of the compression between the different probe locations at the same  $x$  position do not differ much from each other despite the longer distance from the target (Figure 4.9 a). Only the decrease in the magnitude is observed for every measurement. This finding can be explained by the elongated cavity shape along the magnetic field instead of a sphere. While the pulse as well as the diamagnetic cavity propagates along the  $x$ -axis satisfying the spherical expansion as given by the Equation 2.4, it expands faster parallel to the magnetic field (Figure 4.9 b).

---

#### 4.1.2 Electric field measurements

---

The available energy in the shock is partitioned in ion and electron dynamics, but also in electromagnetic fields within the shock, which are known to provide the required deceleration and entropy change [Goodrich and Scudder, 1984, Bale and Mozer, 2007]. The magnetic field structure of shocks, e.g. the terrestrial bow shocks, has been studied thoroughly in the past [Ness and Wilcox, 1964, Scudder et al., 1986, Russell, 2005]. However, there have been only a few works done on the features that can be observed in the electric field despite its importance in controlling energization, the deceleration process, and particle acceleration [Shapiro and Üçer, 2003, Eastwood et al., 2007]. The main reason for this is the difficulties encountered when the electric field measurements are carried out. For example, the features such as short-lived spikes in the electric field are not observed at every shock crossing. Therefore, it is still not clearly understood how the cross-shock electric potential arises, how it scales with shock parameters, or how electrons and ions are heated in the shock. In this section, the results from the electric potential measurement using an electron emissive probe are presented. The measurement was done directly at the cavity edge, which is different from earlier work where the spectroscopic measurement detected the electric field oscillations indirectly. Here, the field oscillations were likely generated via electron beam-plasma instability in debris and ambient plasma interaction as a secondary effect and not directly caused by the relative drift current at the cavity edge [Bondarenko et al., 2014].

Figure 4.10 shows emissive probe data presenting the temporal development of the electric potential (upper left) and the field (upper right) at  $B = 710$  G. The contour plot is a combination of six laser shots at six different locations along the  $x$ -axis in the distance range of 30 to 50 cm from the target. For orientation, two contour lines from the magnetic flux probe measurement are overplotted. The black line represents the region where the magnetic field magnitude decreases to 80 % of its initial value showing the outer edge of the diamagnetic cavity and the red line is the compressed magnetic field area where the magnitude is increased at least a factor of 1.2. A super-Alfvénic pulse ( $\sim 400$  km/s  $\approx 1.3 M_A$ ) was generated, but it did not develop into a shock. The pulse started to slow down to  $\sim 190$  km/s  $\approx 0.7 M_A$  after  $0.5 \mu\text{s}$  and at  $t \approx 1 \mu\text{s}$ ,



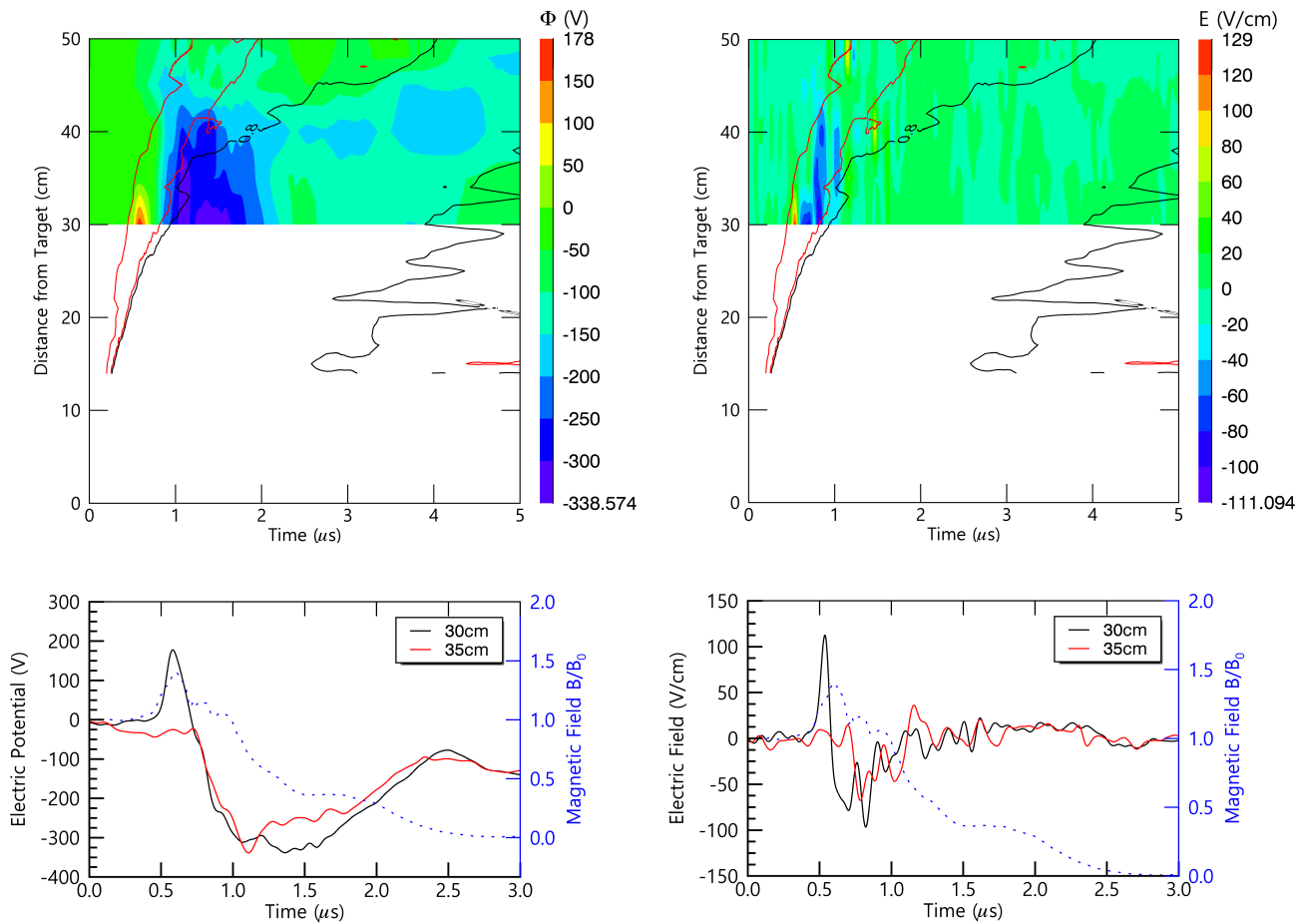


**Figure 4.10:** Upper panel: Contour plot from the electric potential measurement (left) and the calculated electrostatic field (right) with magnetic field contour lines overlotted for the magnetic compression (red) and the diamagnetic cavity edge (black). The figures are a composition of six laser shots measured 30 cm away from the target at a distance interval of about 3 cm. Lower panel: The peak in the electric potential (left) as well as in the radial electric field (right) is observed, consistent with the enhancement of the magnetic compression, but only at  $x = 30$  cm.

it separated from the diamagnetic cavity. One can see that the most interesting regime to look at is the position  $x = 30$  cm, where the electric potential peak is visible, consistent with the magnetic field compression. As already described in Chapter 2.2, the laminar electric field is supposed to be responsible for collisionless coupling mechanisms between debris and ambient ions. With the given experimental plasma parameters, the strongest laminar fields arise in the area of the magnetic compression and the diamagnetic cavity edge. To obtain the radial electric field, the following equation is used

$$E_r = E_x = -\frac{d\Phi_{pl}}{dt} \frac{1}{v_{\perp}} - \frac{dA_x}{dt} \quad \text{with} \quad \nabla^2 A_x = -\frac{\partial B}{\partial y} \quad (4.2)$$

assuming that the cavity moves radially with a constant velocity  $v_{\perp}$  at the position of the measurement. The second term is called the induced term and here, it is to be neglected because  $\partial B/\partial y$  was not measured in our experiment. Let us first assume that the induced term is small enough to be ignored, justifying our simplification. Later, it will be found out, however, that this simplification is to be validated. The lower panels in Figure 4.10 show the temporal development of the electric potential (left) and the electric field (right) at  $x = 30$  and  $35$  cm from the target compared to the magnetic field (dotted in blue). The increase of the potential as well as the electric field was seen shortly before the arrival of the magnetic field enhancement. It is similar to the space shock data from the *in situ* measurements at which the localized increase of the electric field within the magnetic field compression has been detected [Wygant et al., 1987].

Fast photography in Figure 4.11 shows the ion dynamics in the  $x$ - $y$  plane at different times after the laser incident at  $t = 0$  ns, where spatial profiles for the magnetic (yellow) and radial electric (red) fields have been overplotted. The target is located at  $(x, y) = (0 \text{ cm}, 0 \text{ cm})$ . In spectroscopic measurements performed in a related experiment, it was determined that  $C^{+4}$  from the debris plasma is the dominant charge state [Schaeffer et al., 2014] that transfers energy and momentum to the ambient plasma, and it was also confirmed in a numerical study using the two-dimensional hybrid simulation [Clark et al., 2013]. The charge species other than  $C^{+4}$  either free stream in the diamagnetic cavity or fly beyond the magnetic compression without being efficiently coupled to the ambient plasma. The spike in the electric field at the front of the quasi-perpendicular magnetic pulse observed at  $t = 500$  ns might come from the layer generated within the (strongest) magnetic field compression front as in astrophysical shocks [Walker et al., 2004]. This perpendicular electric field is supposed to slow down the upstream plasma [Bale and Mozer, 2007] and is more important in the deceleration process of debris ions than the magnetic forces [Goodrich and Scudder, 1984]. With the given experimental parameters, the laminar electric field magnitude is calculated to be a few hundred V/cm which is a few factors higher than the measured value. The reason could be that the emissive probe only picks up the electrostatic component and the induced term  $dA_x/dt$  is not to be neglected, contradicting our assumption. In future experiments, the magnetic field along the  $y$ -axis should be also measured to obtain the vector potential  $A_x$ . One also observes in the fast photography that the location of the fast debris ions is consistent with the formation of a magnetic compression and diamagnetic cavity. The ions inside the cavity also continue propagating radially. However, they do not contribute much to the production of the magnetosonic pulse. Instead, they might cause the fluctuations observed inside the diamagnetic cavity by the interaction with the ambient ions (Figure 4.6). Similar to the space data [Formisano, 1982, Walker et al., 2004],

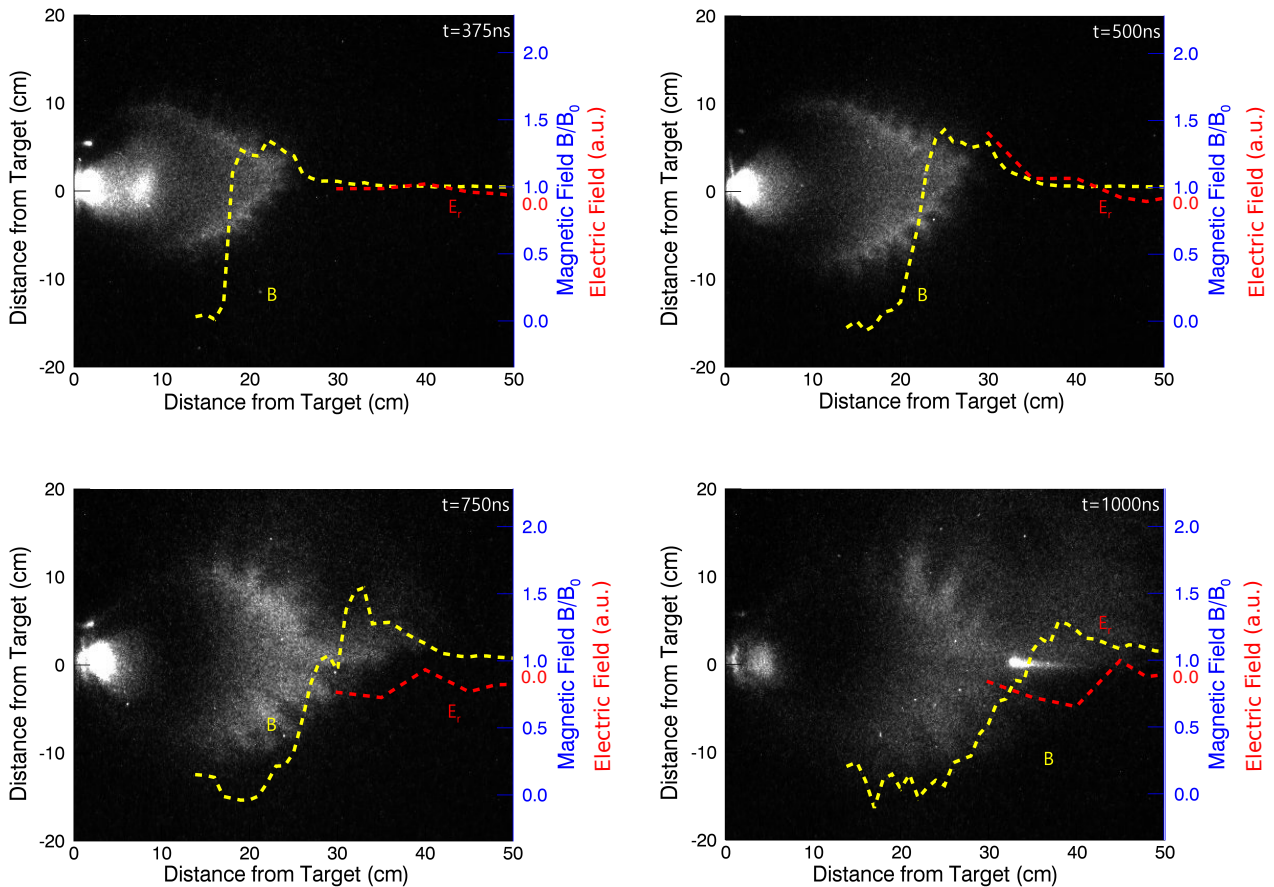


**Figure 4.11:** Spatial development of the radial electric field (red) compared to the magnetic field (yellow) along the x-axis and the ion dynamics ( $C^{+4}$ ) from the fast photography in x-y plane at four different times after the laser irradiation. The rise of the electric field in front of the magnetic ramp at  $t = 500$  ns is observed, consistent with the arrival of the debris ions at the cavity edge. At  $t = 1000$  ns, the debris plasma diffuses and the magnetic peak decreases almost to unity while the radial electric field shows fluctuations around 0 V/cm.

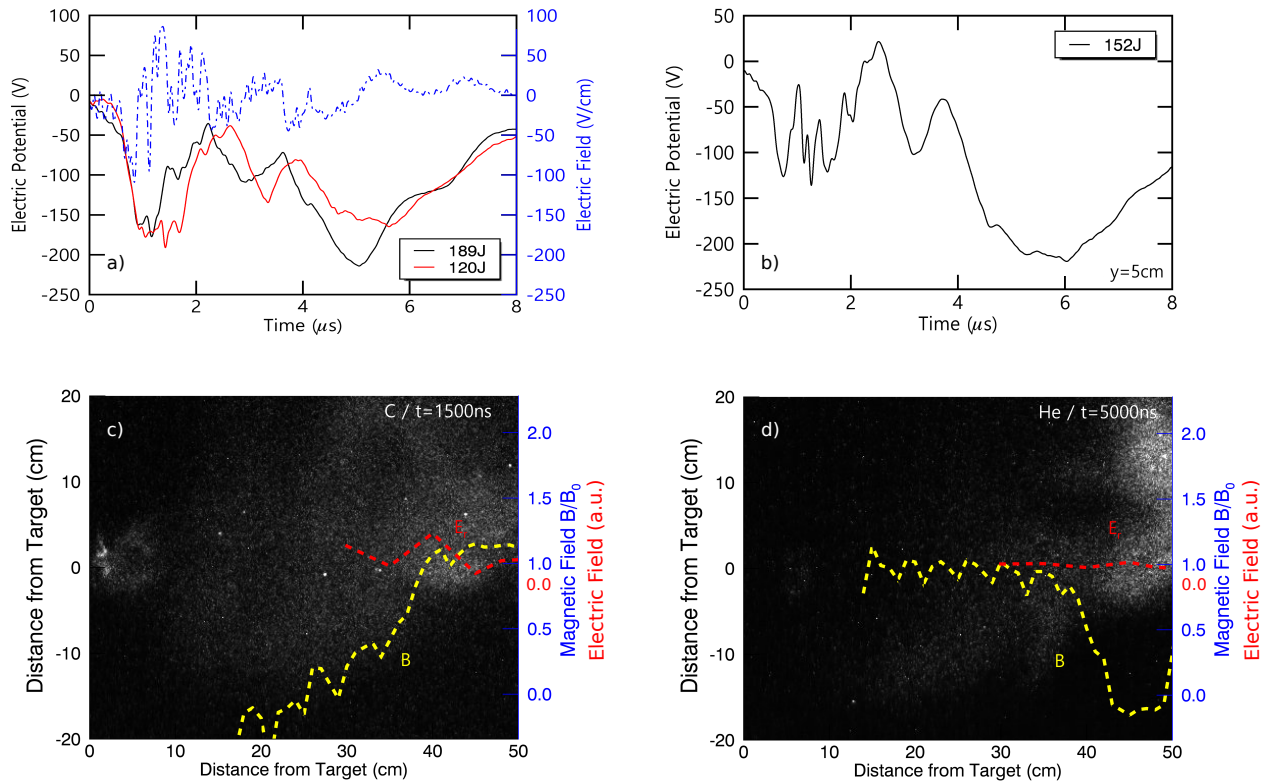


**Figure 4.12:** a) Despite the difference in the laser energy up to  $\sim 30\%$ , the overall structure of the temporal development in the electric potential (black and red) does not seem to be affected significantly. In the electric field (blue), only large fluctuations consistent with the first trough in the electric potential plot are apparent. b) At  $y = 5$  cm, the measured potential is similar to  $y = 0$  cm. The two troughs at  $t = 1500$  and  $5000$  ns observed in the electric potential measurements in perpendicular as well as in the azimuthal direction coincide with the arrival of the different ions. c) The debris ions ( $C^{+4}$ ) expand radially and reach the probe at  $1500$  ns while they slow down due to energy transfer to the ambient plasma through diverse coupling mechanisms. The ambient ions start to be heated and are pushed radially outwards. d) One observes the bulk of the helium ions flies up to about  $50$  cm radially and then moves azimuthally in upward direction causing a negative dip at  $t = 5000$  ns.

the radial electric field increase (red) occurs just upstream of the magnetic ramp. But in the given experiment, the peak of the electric field disappears immediately as it leaves this position. The electric field enhancement in space observations lasts longer than the ramp crossings. Due to the small number of measurements and the large distance between the probe locations, the scale or the duration of the electric field increase or the spatial size of the electric field structure compared to the magnetic ramp, which is known to cover only a few electron inertial lengths [Walker et al., 2004, Bale and Mozer, 2007], could not be confirmed with the given experimental data.

In the experimental campaign with  $B = 710$  and  $1420$  G where the electric field was to be measured, the BaO cathode did not work, but only the LaB<sub>6</sub> cathode. It created a small plasma which was located only in the center of the machine at  $20 \text{ cm} \leq x \leq 40 \text{ cm}$ . Outside the plasma, two characteristic troughs in the electric potential plot were seen (Figure 4.12 a). At  $x = 48 \text{ cm}$ , the first sink occurs about  $1 \mu\text{s}$ , consistent with the arrival of the fast debris ion bulk at the probe (Figure 4.12 c), and the second caused by the ambient ions a few  $\mu\text{s}$  later (Figure 4.12 d). It can be derived from the equation  $\nabla \cdot E = \rho/\epsilon_0$  that the charge density  $\rho$  generated by the bunch of ions is proportional to the electric field, thus the electric potential. In the electric field plot (blue line in Figure 4.12 a), large fluctuations occur only in the compressed magnetic field, similar to the electric field inside the plasma (lower right plot in Figure 4.10), but the overall magnitude of the potential is smaller. The different laser energy does not seem to affect the overall structure much because its decrease from  $189$  to  $120 \text{ J}$  ( $\sim 30 \%$ ) only reduces the blow-off ion velocity of  $10 \%$ , according to  $v_{\text{blow-off}} \propto (E_{\text{laser}})^{0.2}$  [Grun et al., 1981, Key et al., 1983, Meyer and Thiell, 1984]. It is a marginal amount to be visible in the plot. However, the measurement could be possibly considered as a direct evidence of collisionless coupling between the debris and ambient ions. As the ambient plasma density is very low, only the accumulation of moving ambient ions should be charged highly enough to be detected via emissive probes, which gained sufficient energy from the by-passing energetic debris particles.

Larmor coupling is known to be responsible for moving the ambient ions in the azimuthal direction. After a quarter of its gyroperiod, the particles are accelerated radially either with the same velocity of the debris ions or greater depending on the coupling efficiency. The azimuthal field is calculated as the difference of the electric potential at two different positions along the y-axis divided by its distance  $\Delta y$  from each other. In our experiments, all measurements off the axis, at  $y = 5 \text{ cm}$ , were done in a far distance away from the target, thus direct measurement of the Larmor field at the magnetic compression, which emerged near the target, was unfortunately not possible. But still, the two negative peaks in the potential were seen similar to the case at  $y = 0 \text{ cm}$  (Figure 4.12 b). Large fluctuations in the first trough (at  $\sim 1 \mu\text{s}$ ) could be attributed to the instability at the cavity edge driven by the cross-field current, which will be discussed more in detail in the next section, and the second trough (at  $\sim 6 \mu\text{s}$ ) which is deeper compared to the one at  $y = 0 \text{ cm}$  might have been caused by the ambient ions pushed along the positive y-axis as shown in the fast photography at  $t = 5000 \text{ ns}$  (Figure 4.12 d).

---

### 4.1.3 Instabilities

---

The surface features of the diamagnetic cavity are known to depend on the ratio of the ion gyroradius  $\rho_i$  to the magnetic stopping radius  $R_B$ . "Large" plasmas with  $\rho_i \gg R_B$  do not show any



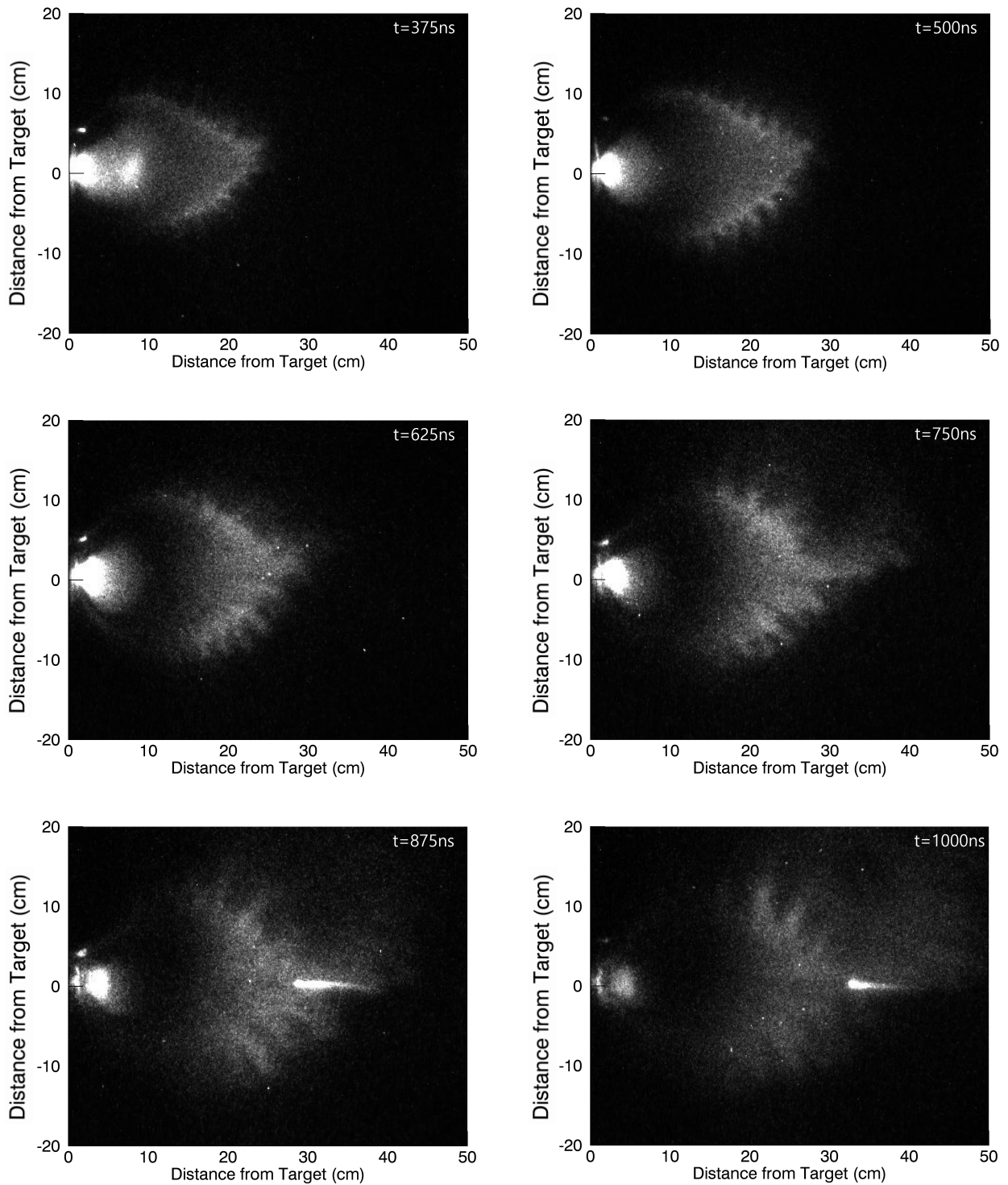


**Figure 4.13:** Debris ion dynamics ( $C^{+4}$ ) observed using a fast photography in x-y plane at different times. The flute-like fingers at the expanding plasma edge grow while the number of the fingers seems to be constant. The bright line in the middle at  $t = 875\text{ ns}$  and  $1000\text{ ns}$  is the reflection on the magnetic flux probe.

observable, field-aligned instabilities while "small" plasmas do [Winske, 1989]. Examples include Active Magnetospheric Particle Tracer Explorer (AMPTE) releases [Bernhardt et al., 1987] where ripples on the plasma surface appeared near the time of the maximum expansion  $\rho_i \sim R_B$  and laser experiments at Naval Research Laboratory [Ripin et al., 1993] where large flute fingers and small mode numbers were observed. In the presented laboratory setting, a low energy of 1 J produced a diamagnetic cavity and instability growth of large amplitudes at the cavity edge could be traced [Collette and Gekelman, 2010]. As it appeared on time-scales faster than  $\omega_{ci}^{-1}$  due to the population of fast debris ions with Larmor-radius larger than the stopping radius, the initiator of the instability was first attributed to Large-Larmor-Radius Rayleigh-Taylor instability (LLRI) [Huba et al., 1987], but the calculated growth time of the LLRI was much longer than the observation.

At the cavity edge, there exists a relative drift of unmagnetized ions and the magnetized electrons. When this cross-field current becomes strong, it provides the required dissipation and the source of free energy to generate a variety of instabilities. In the presented experiments, a flute-like density distribution at the expanding cavity edge could be observed using fast photography and the instability-like fluctuations in the magnetic field as well as in the electric field measurement were also detected. Although ripples on the debris plasma surface in the x-y plane for different charge states were observed, the tracking of the flute-development was best done with  $C^{+4}$ . The instability was observed already at the earliest time of the photography as shown in Figure 4.13. The modes do seem to change, but the flute-arms grew longer in the course of time. Although the tips of flutes appear to bend at  $t = 500$  ns, which might be related to rotation of the flutes along the cavity surface or movement of the flute tips, in the next shot at  $t = 625$  ns, the curve was not visible anymore, and the flute arms already free streamed and grew longer. At  $t = 750$  ns, a pointy end of the laser produced plasma increased in size. Some authors attributed it to the hydromagnetic effect [Plechaty et al., 2013]. At  $t = 1000$  ns, the debris ions lost energy due to the coupling to the surroundings and started to diffuse. The clear waterdrop shape of the debris ion plasma disappeared. The photographic measurements provide a nice optical observation of instability development, but it is not possible to track the movement of the flutes over time. By the time the flute structures can be seen in the particles, the spacing of the flutes along the cavity surface is already comparable to their length and the length scale of the plasma density gradient. The instability evolves with the same time scale in the nonlinear regime, similar to [Winske, 1989, Dimonte and Wiley, 1991, Ripin et al., 1993, Collette and Gekelman, 2010]. In numerical simulation studies, a large number of parameters such as gravitational effects, electromagnetic corrections, density profile, and charge states, are found to have also significant effects on the result [Winske, 1989]. But, often, some of these important local values are not known accurately in experiments so that the direct comparison is not straightforward.

In the high magnetic field with  $B = 1420$  G, peaks in the electric potential could be seen despite the absence of the magnetic field compression (Figure 4.14 a). In this region, an instability-like structure both in electric and magnetic field was observed at two different locations, 27 cm and 32 cm (Figure 4.14 b). In the wavelet analysis using Morlet basis [Torrence and Compo, 1998], the electric field and the z component of the magnetic field oscillations show that the fluctuation lies in a frequency range around 8 MHz. This high frequency region moves with a velocity of 100 km/s consistent with the cavity edge expansion velocity indicating that these fluctuations are generated at the cavity edge. It is known that the free energy for instability originates from the relative ion and electron drift at the



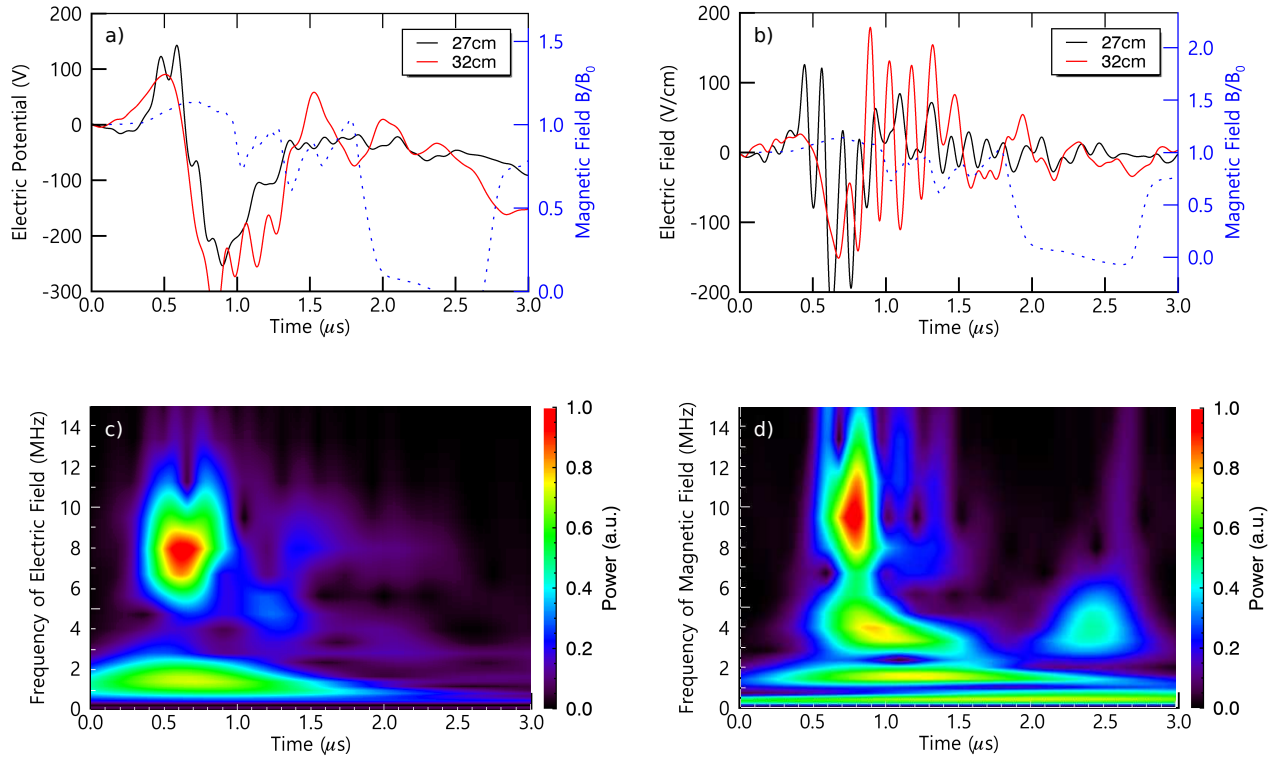


**Figure 4.14:** a) Temporal evolution of the electric potential at  $x = 27$  cm (black) and 32 cm (red) compared to the magnetic field (blue) from measurements at the laser energy  $\sim 160$  J and the magnetic field of 1420 G. b) The calculated electric field fluctuations from the measured electric potential. The peak fluctuations at different locations are about  $0.5 \mu\text{s}$  apart indicating a moving instability with a velocity of about 100 km/s which is consistent with the expansion velocity of the cavity. c) The wavelet analysis of the fluctuating electric and d) magnetic field ( $\dot{B}$ ) component at  $x = 27$  cm is given. The maximum frequency in both fields appears almost at the same time. The slight time difference ( $\sim 0.2 \mu\text{s}$ ) comes from the fact that these signals were taken from two different laser shots.

cavity edge and gives rise to dissipative wave-particle interactions [Wu, 1982]. In the low-frequency regime, the possible candidates for instability structures driven by the  $\vec{E} \times \vec{B}$  drift are the lower-hybrid-drift [McBride et al., 1972, Thomsen et al., 1985] and the modified two-streaming instability [Papadopoulos et al., 1971]. However, with their characteristic frequencies of  $f_{LHDI} \sim 46.3$  MHz and  $f_{MTSI} \sim 41.67$  MHz using the plasma parameters of our experiments, none of the frequency ranges of the proposed instabilities matches the measured frequency of  $\sim 8$  MHz. Another possible instability mechanism driven by the gravitational acceleration at the cavity edge, the Large-Larmor-Radius instability (LLRI), occurs where the ion Larmor-radius becomes large compared to the density gradient length  $L_n$  [Huba et al., 1987]. But the calculated frequency of LLRI of  $f_{LLRI} \approx 3.18$  MHz is about the half of what we measure.

According to the earlier numerical work done by Winske [Winske, 1989], the flute-arms and their wavelengths are known not to be affected by the magnitude of the external magnetic field. Based on this work, the observed instability using the fast photography at 710 G should be comparable to the measurements done at 1420 G. From the rough estimation of the flute patterns as shown in Figure 4.13, the frequency of the instability can be calculated from

$$f = \frac{v_{\perp}}{\lambda} \quad (4.3)$$

where  $\lambda$  is the observed flute wavelength and  $v_{\perp}$  the expansion velocity of the diamagnetic cavity. With  $\lambda \approx 5$  cm and  $v_{\perp} \approx 375$  km/s at  $t = 625$  ns when the dense plasma tip first arrives at the probe position  $x = 30$  cm, the calculated frequency is  $\sim 7.5$  MHz, consistent with the probe measurements. The fluctuations in this frequency range were also detected in the electric field measurement at the lower magnetic field, 710 G. The flute patterns appear to be consistent with the static -frozen into the plasma- flute-like modes passing the probe instead of growing out of the plasma edge region randomly. Huba et al. [Huba et al., 1987] indicates that, as the instability progresses, the longer-wavelength structures dominate over the fast growing modes with short wavelength and the unstable density profile disrupts more of the density profile, which might have an influence on our instability structure. The peak frequency of the magnetic field is found to be higher when measured closer to the target, probably due to the strong cross-field current, but as already mentioned in Chapter 4.1.1 (Figure 4.6), high frequency fluctuations are not detected at every probe measurement for unknown reasons. The excitation of the instabilities at the cavity edge is supposed to be one of the causes for the shorter cavity lifetime compared to the classical diffusion time. In previous experiments, a difference in lifetime for different ambient plasmas was observed and faster debris ions generated by reducing the laser focal size on target excited more instability and decreased the cavity lifetime [Niemann et al., 2013].

---

## 4.2 Excitation of shear Alfvén waves

---

The capability of Alfvén wave generation via a laser produced plasma expanding into an ambient magnetized plasma with the laser energy  $\leq 30$  J has been previously investigated in the present experimental setting [VanZeeland et al., 2003, Gekelman et al., 2003, Niemann et al., 2013]. In contrast to vacuum where the electrons are held back by large ambipolar fields, the background plasma electrons flow into the diamagnetic cavity while the electrons from the laser produced plasma escape down the magnetic field lines as a result of charge neutralization. The generated fast electron flows are known to launch shear Alfvén waves as an effect of Cherenkov

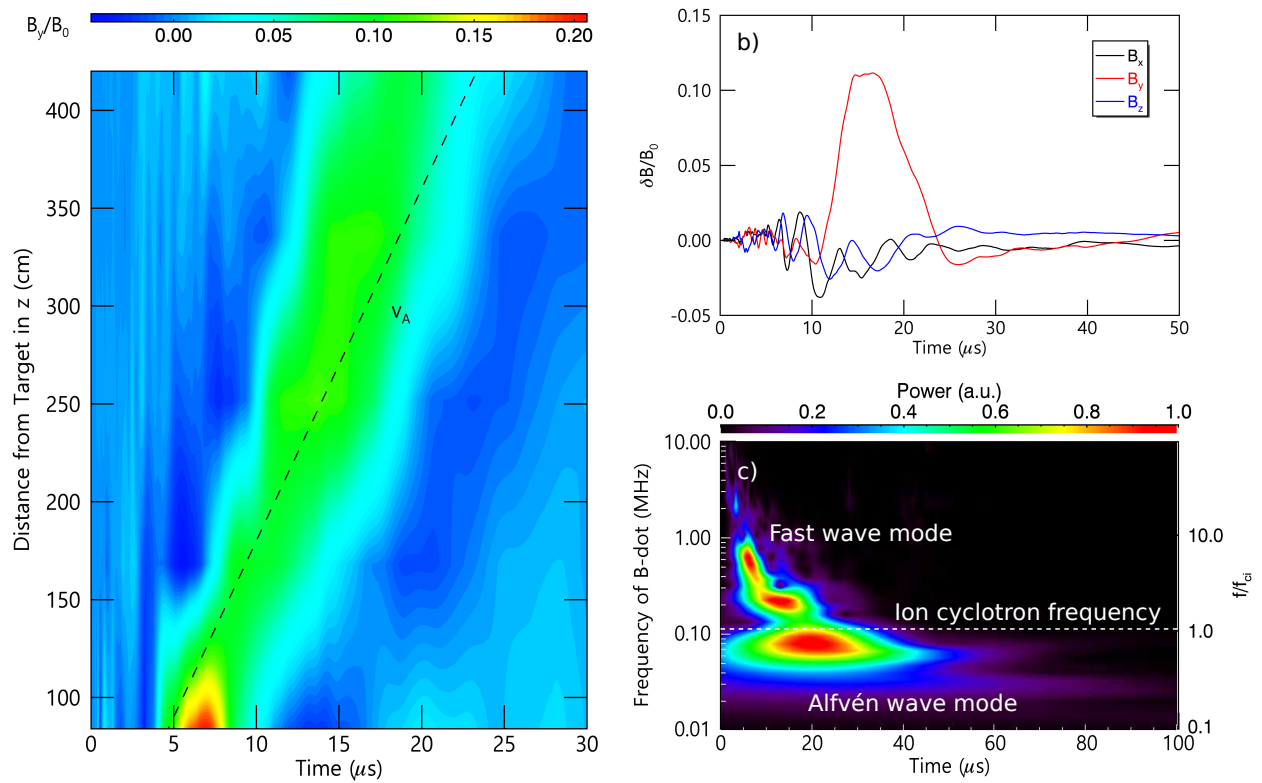
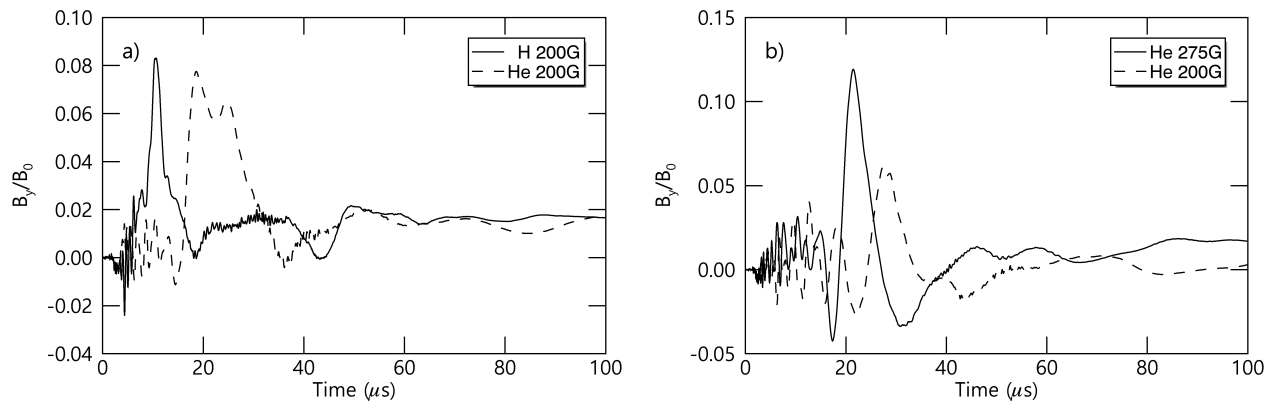


**Figure 4.15:** a) Contour plot of the transverse field component  $B_y$  as a function of time along the machine ( $z$ -axis) in a helium plasma with  $B = 275$  G obtained from five magnetic flux probes distributed along the magnetic field line at  $x = 10$  cm from a single laser shot. A shear Alfvén wave propagates with  $v_A = 180$  km/s preceded by the fast waves of  $\sim 1.67 v_A$  (blue area). b) Temporal development of the magnetic field at  $(x, y, z) = (10 \text{ cm}, 0 \text{ cm}, 336 \text{ cm})$  relative to the target position. Fast waves cause fluctuations of the magnetic field in all three axes while the shear Alfvén wave has a perturbed  $B_y$ , large compared to  $B_x$  and  $B_z$ . c) The auto-spectrum of  $B_y$ . The intense mode above the ambient ion Larmor-frequency  $f_{ci} \sim 110$  kHz indicates compressional fast waves followed by the shear Alfvén mode.

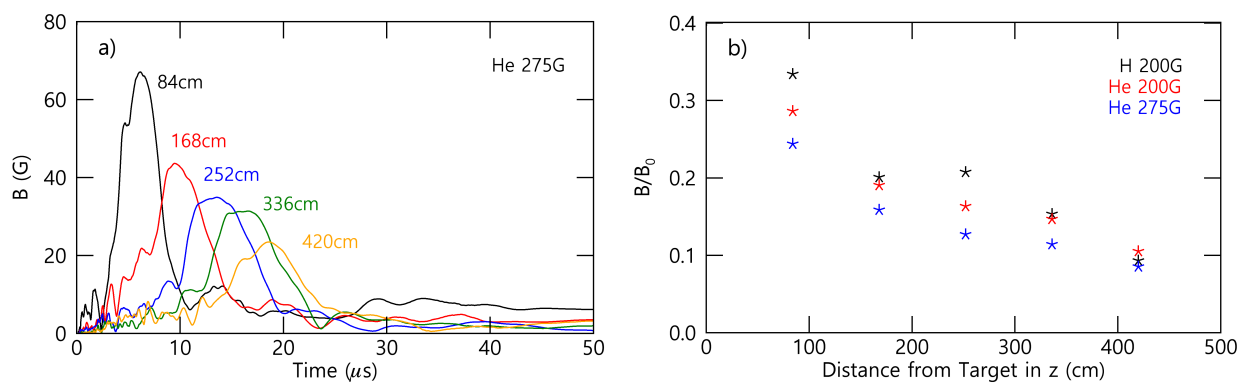
radiation [Van Compernelle et al., 2008] and other quasi-electrostatic waves such as whistlers have been also detected [Vincena et al., 2008]. In this section, the features of Alfvén waves generated by diamagnetic cavities at laser energies of 50 to 200 J are displayed and compared to the results of earlier works.

Figure 4.15 a) shows characteristic shear Alfvén wave features along the magnetic field propagating at the Alfvén speed  $v_A \approx 180$  km/s in a helium plasma at  $B = 275$  G,  $x = 10$  cm. The maximum amplitude of the perturbed magnetic field  $B_y$  is about 25 % of the external field near the target, but decreases with distance. In the course of time, one also observes its broadening due to the damping across the field. Before the Alfvén wave arrives, fast waves of small amplitudes precede it with a velocity higher than  $v_A$ . While the typical feature of the shear wave is the large fluctuation of  $B_y$  due to its dominant response to the magnetic field compared to  $B_z$ , the fast wave is a compressional mode with fluctuations in all three components. The compressional modes are found to be above the ambient ion cyclotron frequency  $f_{ci} = Z_i e B / 2\pi m_i \approx 110$  kHz (Figure 4.15 b) and must have been generated by high energetic electrons from the diamagnetic cavity edge in the early process with field fluctuations of a few Gauss. The shear Alfvén wave is in the low-frequency regime of about 100 kHz, below  $f_{ci}$  (Figure 4.15 c). One interesting feature is that the measured perturbation seems to be rather like a soliton than a wave, different than previous works at lower laser energy [VanZeeland et al., 2003, Niemann et al., 2013]. Finite-amplitude Alfvén waves are excited by, e.g. energetic charged particle beams, non-uniform background plasma parameters, or electromagnetic waves, and give rise to various nonlinear phenomena like wave-amplitude modulation, filamentation, and density profile modification. By combining the dispersive character of kinetic Alfvén waves and their nonlinear interaction with the ambient plasma or with themselves, a solitary kinetic Alfvén wave can be formed [Shukla and Stenflo, 1995]. The theory of the solitary Alfvén wave can be found using kinetic theory [Hasegawa and Mima, 1976]. In space, these waves were also detected from *in situ* measurements by satellites where the auroral plasma energization processes changed very rapidly due to Landau damping [Lundin et al., 1995]. One must first show, however, that the measured waves have the properties of solitary kinetic Alfvén waves. For example, the existence of solitary kinetic Alfvén waves are known to be accompanied by a hump or dip density soliton, as predicted theoretically in [Hasegawa and Mima, 1976, Shukla et al., 1982] and studied numerically in [Wu et al., 1996]. As we only measured the magnetic field changes along the machine and no data about the particle density or velocity measurements are available, the exact determination of the detected Alfvén waves is left for future work with an improved setup of diagnostics. For this reason, the hydromagnetic waves with the observed structure will be referred to as "soliton-like" Alfvén waves in this work.

Figure 4.16 shows the fluctuating y components of the magnetic field in different ambient plasmas as well as at different magnetic fields. The time delay of the peak arrival of the Alfvén wave is consistent with  $v_A \propto B / \sqrt{m_i}$ . The maximum magnetic field amplitude in helium plasma at 275 G is  $|\delta B| \approx 70$  G ( $\sim 25$  %) (Figure 4.17 a) and decreases with distance. The decrease of the maximum amplitude occurs linearly (Figure 4.17 b) regardless of the background plasma or the applied external field whereas the slightly different slope might be a function of these factors. The reduced magnetic field amplitude at  $z = 168$  cm is due to a misalignment of the magnetic flux probe. Broadening of the spectral peak due to the dispersion is also observed. This kind of behavior results from velocity dispersion of the particles or any other damping mecha-



**Figure 4.16:** a) Temporal evolution of  $B_y$  in hydrogen (straight) and helium (dashed) plasma scaled to the background magnetic field at 200 G at  $(x, y, z) = (10 \text{ cm}, 0 \text{ cm}, 336 \text{ cm})$ . b) The y component of the fluctuating magnetic field at  $B = 275 \text{ G}$  (straight) and 200 G (dashed),  $(x, y, z) = (18 \text{ cm}, 0 \text{ cm}, 336 \text{ cm})$  in a helium plasma. Both measurements were done at the laser energy of 100 J.



**Figure 4.17:** a) Temporal development of the shear Alfvén wave magnitude at different locations along the z-axis and b) the decrease of the amplitude as a function of the distance from the target. The dip at  $z = 168 \text{ cm}$  comes from a misalignment of the magnetic flux probe.

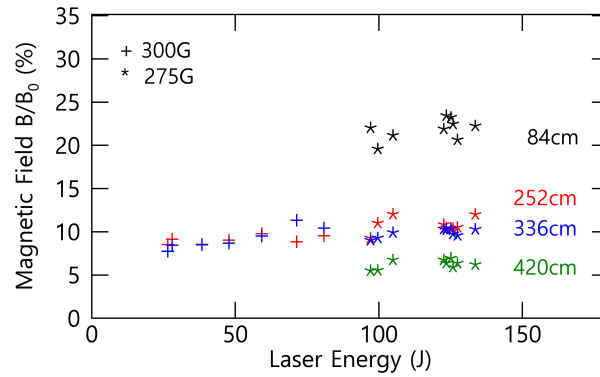
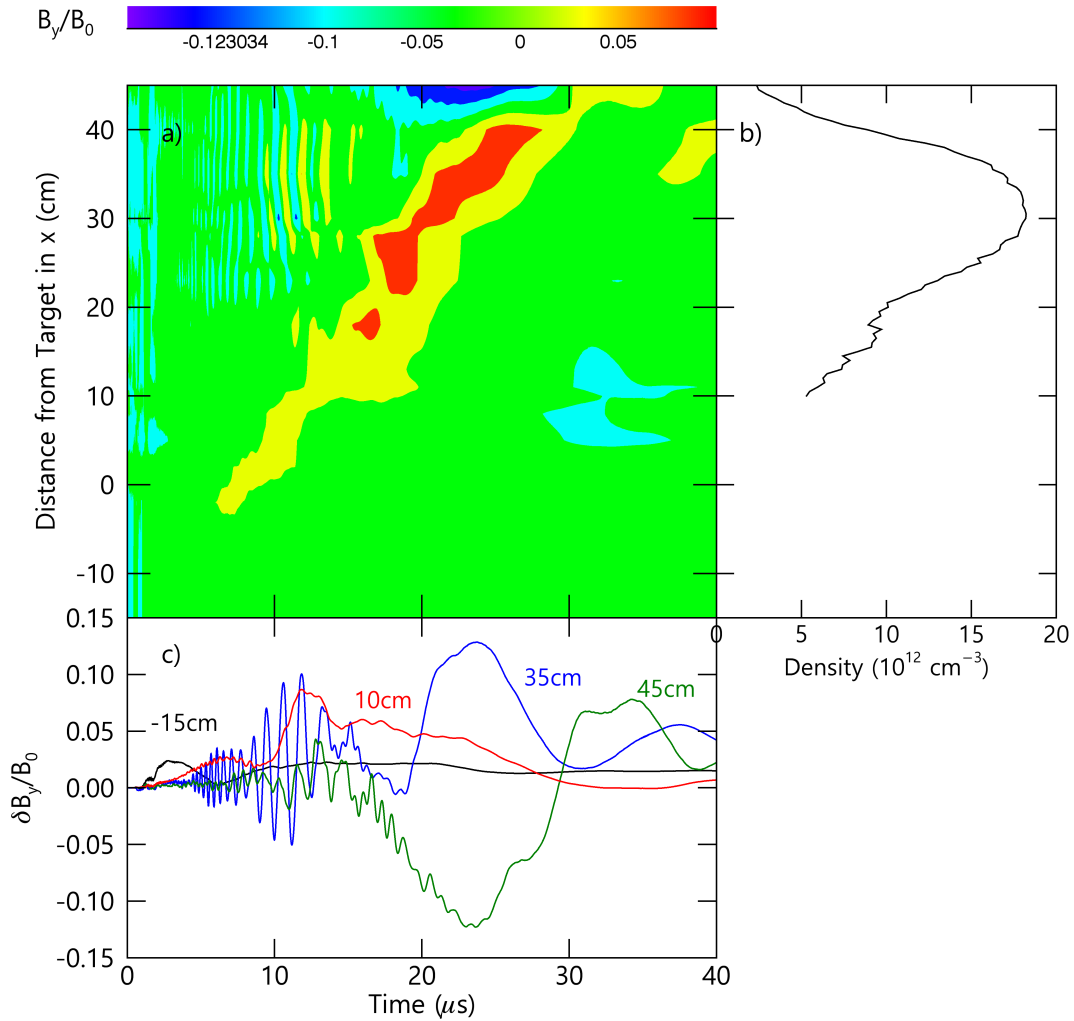


**Figure 4.18:** Amplitude of the shear wave as a function of the laser energy at different  $z$  positions in a helium plasma. The measurements are performed at 275 G (\*) and 300 G (+) in different energy regimes. The amplitude does not seem to be affected.

nisms. For example, in the kinetic regime where the thermal electron velocity  $v_{th,e}$  exceeds  $v_A$  corresponding to our experiment, Landau damping could take part in the damping process.

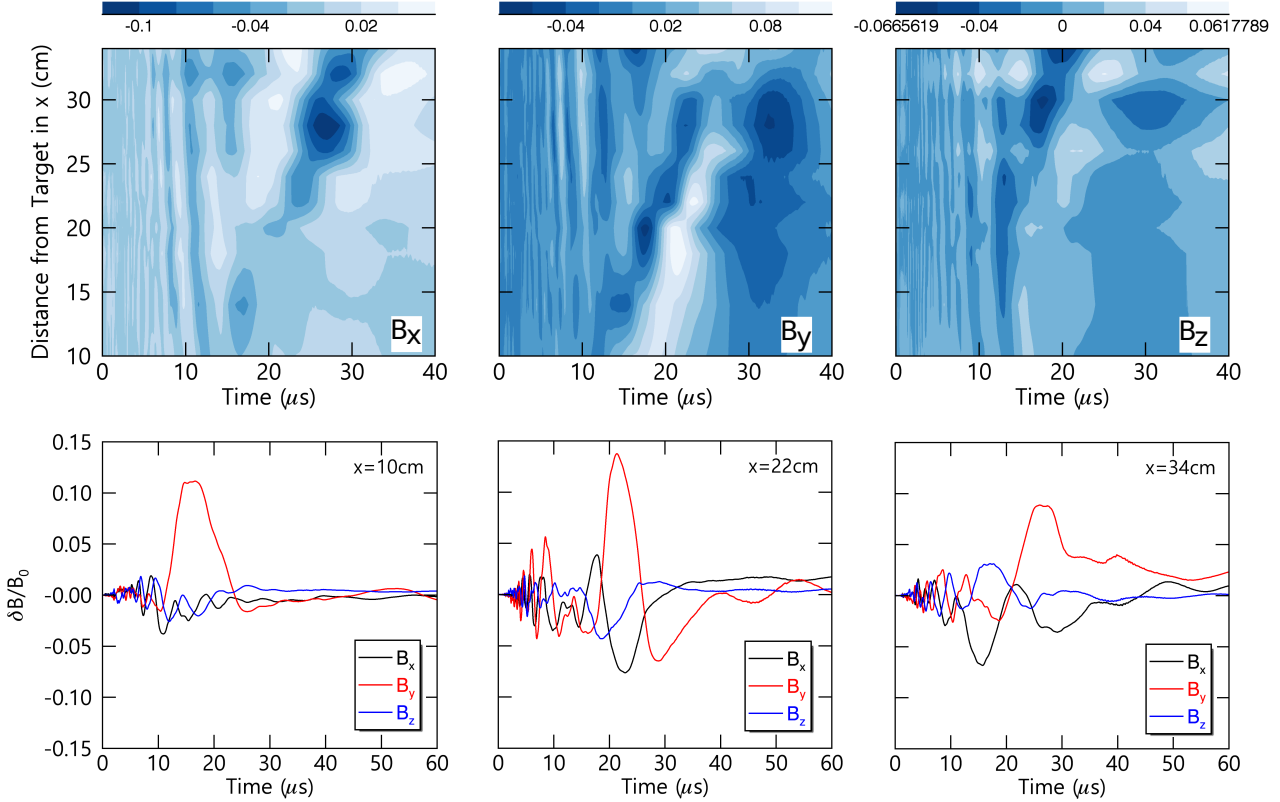
In contrast to the conclusion drawn in the lower energy case  $E_{laser} \leq 25$  J [Niemann et al., 2013] where the amplitudes of the shear waves at a fixed position are observed to increase linearly with laser energy, the amplitude of the Alfvén waves seems not to be influenced in the high laser energy regime. Figure 4.18 displays a result from two different runs, one at  $B = 275$  G (\*) and 300 G (+) both in a helium plasma. The maximum amplitude of the detected shear waves along the machine were plotted for the applied laser energy at different distances from the target. No significant increase of the amplitude for higher laser energy is observed. The decrease in magnitude with distance is consistent with the case caused by damping mechanisms as shown in Figure 4.17. The overlapping values for  $z = 252$  and 336 cm might be due to the changing magnetic field strengths along the field line, which affects the Alfvén wave propagation velocity accordingly. The overall character of the signal such as compressional mode frequency, arrival time, and the form of the Alfvén wave does not vary despite increasing laser energy.

Figure 4.19 a) is a contour plot of a composition of 15 laser shots and shows the generation of an Alfvén wave along the  $x$ -axis. The different arrival times of the Alfvén wave are attributed to the non-homogeneous density of the ambient plasma in the  $x$ - $y$  plane (Figure 4.19 b) causing slower propagation of the wave in the dense region. As  $v_A \propto 1/\sqrt{n_i}$ , the arrival time of the Alfvén wave in the most dense region ( $x = 30$  cm) is about 1.9 times later than that of the low-density region at  $x = 10$  cm, consistent with the measurement. The compressional mode arrives before the Alfvén wave and the large increase of the wave amplitudes was observed in the high-density area. The temporal magnetic fluctuation shapes differ according to the location at the  $x$ -axis (Figure 4.19 c). Niemann *et al.* proposed that a wide, quasi-coaxial current system is generated with its center close to the projection of the cavity edge at the time of peak diamagnetism  $\tau_{peak}$  along the  $z$ -axis [Niemann et al., 2013]. This is in contrast to the earlier work at much lower energy ( $\sim 1$  J) [VanZeeland et al., 2003] where two current flows were suggested in which the one flow is from the electrons escaping the cavity and the other is the return current from the background plasma at the cavity edge (Figure 2.8). In this work, the current density was not measured, so a direct comparison is not possible, but the



**Figure 4.19:** a) Contour plot of  $B_y$  at  $B = 300$  G in a hydrogen plasma along the x-axis, 420 cm away from the target in z. The large fluctuation before the arrival of the shear Alfvén wave at  $20 \text{ cm} \leq x \leq 40 \text{ cm}$  might have been caused by b) the dense plasma region with  $n_i \geq 10^{13} \text{ cm}^{-3}$ . c) Temporal development of  $B_y$  at different x positions is compared. The flipping of the shear wave peak at  $x = 45 \text{ cm}$  (green) may indicate the regime beyond the diamagnetic cavity with its size  $2R_c \sim 40 \text{ cm}$ .





**Figure 4.20:** Upper panel: Contour plot of the temporal development for  $B_x$ ,  $B_y$ , and  $B_z$  in a helium plasma at 275 G along the x-axis at  $z = 336$  cm. The different arrival times of the shear Alfvén wave are caused by non-uniform ambient plasma density distribution along the transverse axis. Different than in  $B_y$ ,  $B_x$  and  $B_z$  gain in amplitude for increasing  $x$ . Lower panel: The soliton-like structure disappears at farther distances from the target along the x-axis.

diamagnetic cavity expanded up to about  $x = 45$  cm along the blow-off axis, which is coincident with the location of the observed flipping of the Alfvén wave. This might support the argument of Niemann *et al.* [Niemann *et al.*, 2013] since the inverse signal was found to be at  $x$  positions beyond the maximum cavity size along the x-axis due to the generated current at the cavity edge which flows down along the magnetic field.

As one investigates the magnetic field components farther along the x-axis, the soliton-like feature of the Alfvén wave as shown in Figure 4.15 b) disappears. The magnitude of  $B_y$  decreases and becomes more wave-like while  $B_x$  and  $B_z$  gain in magnitude so that the shear wave characteristics ( $B_y \sim 10 \times B_z$ ) disappears (Figure 4.20). As the diamagnetic cavity expands, the escaping electrons can be depicted as a number of small sources. These multiple current channels interact with each other and spread throughout the magnetic field causing fluctuations in all three axes. Large and non-local wave fields might interfere constructively which are not directly connected to one current source [Gekelman *et al.*, 1997b, Gekelman, 1999]. Another explanation may be that the velocity distribution of the electrons varies along the x-axis from the diamagnetic cavity. In a numerical study [Van Compernelle *et al.*, 2008], a super-Alfvénic electron burst produces field-aligned current filaments, but when its velocity decreases, the pattern of the filaments changes and spreads more in the transverse direction. In the early propagation

Ambient	B	$E_{laser}$	$E_A$	$E_A/E_{laser}$	$E_A/E_c$
H	200 G	90 J	19.2 J	21.4 %	146.6 %
He	200 G	100 J	15.3 J	15.3 %	287.5 %
He	275 G	26 J	0.9 J	3.4 %	69.2 %
He	275 G	130 J	19.7 J	15.1 %	246.9 %

**Table 4.2:** Plasma parameters for experiments with different ambient plasma species, external magnetic field  $B$ , and laser energy  $E_{laser}$ . The Alfvén wave energy  $E_A$  is compared to  $E_{laser}$  and the diamagnetic cavity energy  $E_c$ . The data in the third row is from [Niemann et al., 2013].

process, the diamagnetic cavity itself expands with super-Alfvénic velocity, but starts soon to stagnate. Therefore, farther from the target, electrons generated at the cavity edge would no longer propagate strictly along the field, but interact with other particles or fields in the transverse direction resulting in field perturbations in every direction. This could be another possible explanation for the disappearance of the feature of the shear wave as one moves further from the target. More electron heating at the edge of the cavity with higher expansion speed was also observed experimentally [Niemann et al., 2013].

The energy of shear Alfvén waves is given by

$$E_A = \frac{1}{2\mu_0} \int B^2(r) dV \quad (4.4)$$

where  $dV = 2\pi r dr dz$  is the volume of the wave,  $r$  the radial distance from the center of the system, and  $dz$  the wavelength of the wave ignoring trailing oscillations of lower amplitudes. Here,  $r$  can be defined as the cavity size  $2R_c$ . Because the ion velocity was not measured, the kinetic energy of the flowing plasma is not taken into account. The laser energy coupling efficiency to shear Alfvén waves detected in our experiment is given in Table 4.2. Better coupling efficiencies are observed for lighter background plasma and for higher laser energy. In higher magnetic field, a smaller cavity size would induce a smaller current system width and therefore, the coupling efficiency to the shear Alfvén waves is expected to decrease [Niemann et al., 2013]. The energy ratio between the shear wave and the laser shows a significant effect of the laser energy increase. Compared to the previous work [VanZeeland et al., 2001] where only 0.5 % of the laser energy was used to generate Alfvén waves, here the coupling is a few factors higher. In the high laser energy regime  $\geq 90$  J, the shear wave energy exceeds the energy contained in the diamagnetic cavity.

### 4.3 Summary

Experiments were performed in a high laser energy regime  $\geq 50$  J, which had not been reached previously in the presented laboratory setting. A summary of the findings is given as follows:

- The diamagnetic cavity structure is similar to the case of  $E_{laser} \sim 30$  J. The inner magnetic field is fully expelled and the magnetic compression precedes the cavity with a super-Alfvénic velocity. But a stronger coupling to the ambient plasma is observed.
- The dependence of the diamagnetic cavity size on different ambient plasma species and the laser energy has been observed indicating a different coupling efficiency affected by these parameters. The ratio of laser energy to energy contained in a spherical cavity scales with  $B^2$ , similar to the previous works at lower laser energy.
- Better energy conversion efficiency as well as coupling efficiency to the background magnetic field of the diamagnetic cavity is derived for increasing magnetic field strength, consistent with experiments in vacuum.
- Propagation of a diamagnetic cavity fully separated from the target is only observed in high magnetic fields.
- The measured field oscillations can be divided into a variety of different frequency regimes. These might be generated by the slow debris ions which do not contribute to the generation of magnetosonic pulses at the cavity edge, but stay in the cavity interacting with ambient ions.
- A faster growth of the cavity in size along the magnetic field was detected and a differing cavity shape from a sphere was measured.
- For the first time in the present laboratory setting, the electric potential and the electric field were measured directly at the magnetic cavity edge using electron emissive probes. The enhancement of the radial electric field, which is consistent with the magnetic field compression, is similar to the space data and might be responsible for the collisionless coupling between particles, which accelerate the ambient ions into the radial direction.
- Flute-like instability features are observed using fast photography. Even at the earliest time of the dense plasma expansion, the flutes seem to have already reached the nonlinear regime. These features could be also seen in the magnetic and electric field measurements with the measured frequency of the fluctuations corresponding to the calculated frequency from fast photography. The observed instability might be responsible for energy dissipation at the subcritical shock ramp and is also considered as one of the causes for the short lifetime of the diamagnetic cavity compared to the classical diffusion time. The exact identification of these flute-like fluctuations was not possible.
- The Alfvén waves are known to be excited by high energetic electrons along the magnetic field via Cherenkov radiation, which are generated at the diamagnetic cavity edge. In this experiment, soliton-like kinetic Alfvén waves are observed, probably as a result of nonlinear interactions between finite-amplitude Alfvén waves and their surroundings.
- The magnitude of the Alfvén wave decreases with increasing distance from the target and the external field magnitude possibly due to Landau damping.
- The soliton-like feature of the Alfvén waves disappears when one moves away from the target along the x-axis. It might be caused either by the constructive interference of the waves along the field line or the transverse dispersion of the electric currents generated at the cavity edge with different velocity.

- 
- 
- In the laser energy regime  $\geq 30$  J, the energy conversion efficiency from the laser to the diamagnetic cavity seems to depend only on the magnetic field while the Alfvén waves gain more energy for  $E_{laser} \sim 100$  J compared to  $\sim 30$  J. This indicates that the diamagnetic cavity has already reached its saturation level in energy and the residual energy might be partitioned between the acceleration of ambient ions or generation of high energetic electrons resulting in nonlinear Alfvén waves along the magnetic field.



---

## 5 Two-dimensional hybrid simulation

---

Computer simulations serve to help develop and verify theoretical models and test the underlying assumptions with limited physics. Initially, cylindrical plasma expansion into a magnetized plasma in super-Alfvénic regime in one-dimensional simulation has been presented [Golubev et al., 1979], followed by a two-dimensional hybrid code developed by Bashurin [Bashurin et al., 1983] to model a spherical dense plasma expansion into the low-density magnetized background. The importance of this kind of numerical works gained on emphasis, especially when the man-made nuclear bomb explosion in the ionosphere [Bernhardt et al., 1987, Dyal, 2006] delivered interesting data, but failed to give accurate answers to specific questions concerning such as the mechanism by which the debris ions are stopped or the conditions under which a shock wave can be generated. It is still not fully understood how the properties of the shock scale with the plasma parameters or which are the underlying physical processes. Therefore, the attempts with numerical simulations led to shed some light on the field that was not easy to be studied experimentally [Thomas and Brecht, 1986, Winske, 1996, Hewett et al., 2011]. Numerical simulations are not only used to verify, e.g. high Mach number space and astrophysical shocks [Lembège et al., 2004, Winske and Gary, 2007], but also to provide insight into laboratory experiments and to study magnetosonic plasma expansion [Dimonte and Wiley, 1991, Ripin et al., 1993]. Recently, the shock formation conditions in a laboratory plasma were studied in a two-dimensional simulation [Clark et al., 2013] and the predicted shock generation was experimentally proven [Niemann et al., 2014, Schaeffer et al., 2014]. The experimental data are used, in turn, to benchmark the physics in the simulation models.

The hybrid simulation is extensively implemented for simulation of high Mach number shocks [Thomas and Brecht, 1986], nonlinear evolution of waves [Winske, 1989], or the development of the electromagnetic ion beam instability [Huba et al., 1987], where electrons are of second importance compared to the ions. Electromagnetic phenomena are treated in dependence on the ion time  $\omega_{ci}^{-1}$ , the inverse ambient ion gyrofrequency, and spatial scales of the ion inertial length  $c/\omega_{pi}$  (the speed of light  $c$  as the unit of velocity) which allows to model large-scale plasmas of several tens of cm comparable with the actual experiment. This scaling is also favorably used in space shock physics where the ion dissipation plays an important role at the shock compared to the electrons [Scudder et al., 1986]. Here, electrons are treated in quasi-neutral approximation meaning that it is in the limit in which the electric field connecting the electron to the ions is so strong that the electron density can be locally set equal to the effective charge density of all the ions. Where the electron density is needed in the momentum equation,  $n_i$  is used from ions. Therefore, the electric field in the simulation is rather the field needed to maintain the charge neutrality on the ion spatial scales than the electric field generated by the charge separation [Winske and Omid, 1993]. This assumption simplifies the physics of the electrons to the point so that the kinetic nature can be neglected. In this so-called Darwin-approximation or radiation-free limit, electrons are treated as massless fluid ignoring the thermal electron oscillations, gyrations, and thus the displacement current in Ampère's law according to the magnetostatic approximation [Winske and Gary, 2007, Clark et al., 2013]. For ions, the fluid approximation is not valid because the stopping distance and the gyroradii of the ions are assumed to be zero in

the MHD transport approximation [Hewett et al., 2011]. Therefore, the kinetic model with the particle-in-cell technique is used for ions. As the electron dynamics is neglected, the dissipation mechanism in the simulation is performed via ion reflection instead of electron instability. In the presented hybrid simulation, the coordinates are given in two Cartesian spatial dimensions while the velocities and the fields in three dimensions. The magnetic field is set to be in the z-direction, perpendicular to the plane of the simulation. To compare the simulation results to the experiment, the simulation can be run under the same condition as the experiment.

In the subsequent sections, two independent studies are given. First, a parameter study of magnetized collisionless shocks in a laboratory setting is presented in which the polytropic index and, thus, the electron pressure model is varied. The results are recently published in [Lee et al., 2015]. This study of the effect of the electron pressure  $\gamma_e$  emphasized the importance of electric field measurement in experiment, not only to understand the shock structure, but also to validate the accuracy of the simulation. Then, the simulation parameters are modified according to the recent experiment where the electrostatic field in the magnetic field compression has been measured for the first time (Chapter 4.1.2) using the electron emissive probe (Chapter 3.4). The experiment-like simulation results are given in Chapter 5.2. A summary of the simulation study follows in Chapter 5.3.

---

## 5.1 Effect of electron pressure $\gamma_e$

---

In this simulation, the laser irradiation on the target is demonstrated as an explosion of the debris ions into the ambient magnetized plasma, similar to the astrophysical explosions into tenuous background. As already mentioned, the application of the hybrid mode to subcritical shocks is limited by the fact that the dissipation in the model is only due to reflected ions, while the dissipation in subcritical shocks in space is believed to be mostly due to micro-instabilities driven by the cross-field current (Chapter 2.4). Moreover, the electron model is known to have a very small effect on the overall structure so that its temperature in the presented simulation is given as

$$T_e(x) = T_{e0} \left( \frac{n_e(x)}{n_0} \right)^{\gamma_e - 1} \quad (5.1)$$

where  $n_0$  is the initial ambient ion density and  $\gamma_e$  the polytropic coefficient. The only variable parameter of electrons in the simulation is the polytropic coefficient in the electron temperature equation. This can result in underestimating the electron temperature in the simulation affecting the dynamics of the ions and the magnetic field. To partially overcome this limitation,  $\gamma_e$  in the electron fluid equation can be modified so that the electron temperature increases faster than adiabatically.

Here, we compare two perpendicular plasma expansions that differ only in the polytropic coefficient. First, a two-fluid system is introduced so that varying  $\gamma_e$  does not impact the initial dynamics of the debris ions. The electrons are divided into two groups: one that is only affected by the ambient ions and the other by the debris ions. Here, the polytropic coefficient of the debris ions is 5/3, an adiabatic case, but that of the ambient electrons is varied so that the electrons and the ambient ions are heated nonadiabatically. The fluid model of electrons keeps the



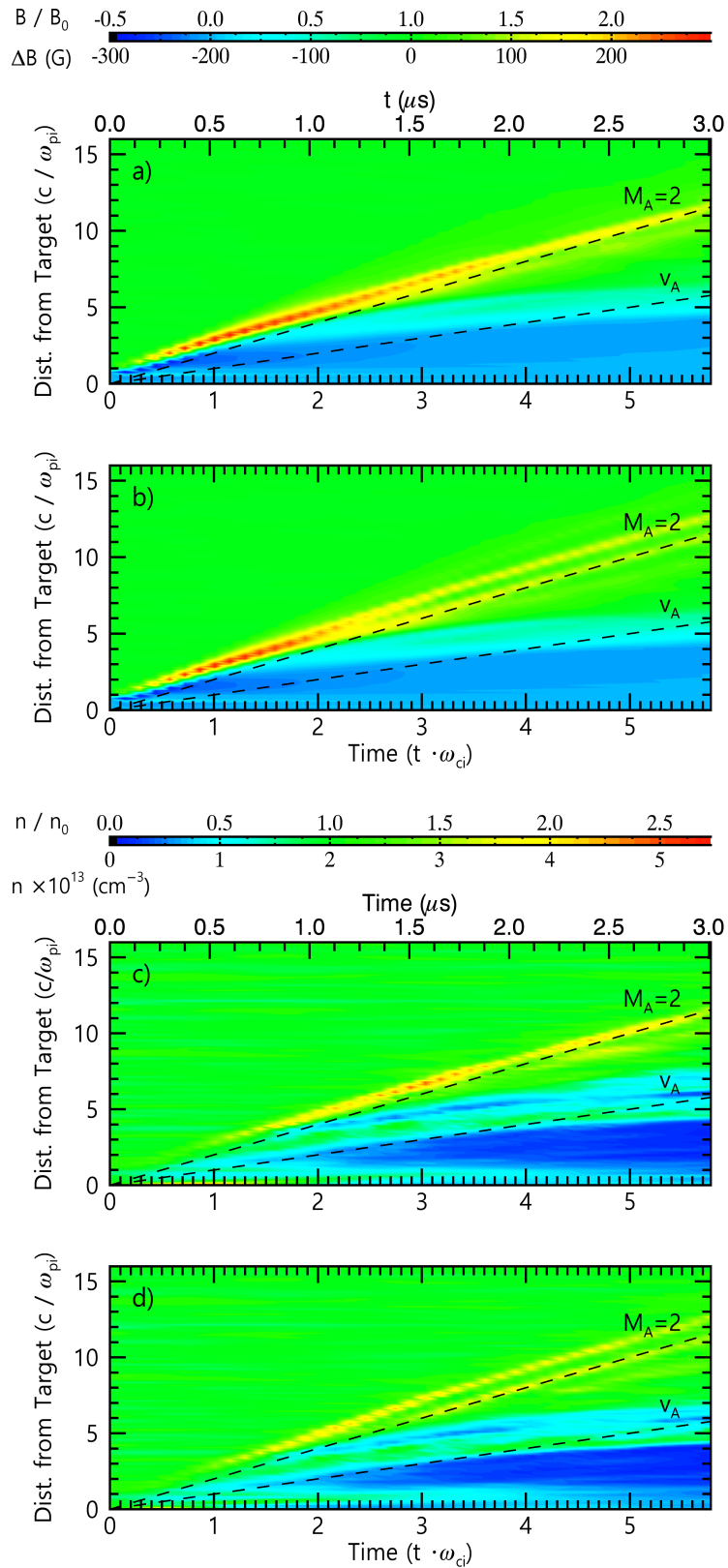


**Figure 5.1:** Temporal change in the magnetic field strength  $B_z$  is given for a)  $\gamma_e = 1.67$  and b)  $\gamma_e = 5$  and the ambient plasma density for c)  $\gamma_e = 1.67$  and d)  $\gamma_e = 5$  along the x-axis. Dashed lines are the expansion velocity.

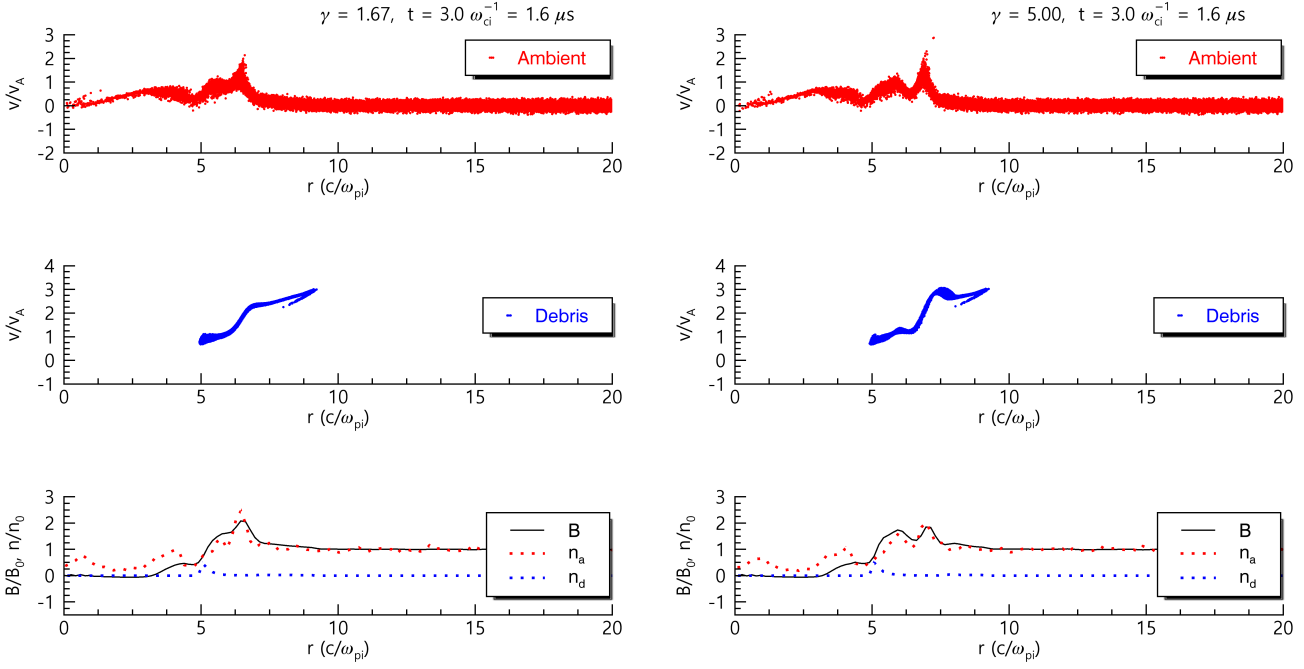


**Figure 5.2:** Phase space plots of ambient (red) and debris ions (blue) for  $\gamma_e = 1.67$  and  $5$  at  $t = 3 \omega_{ci}^{-1}$ . Spatial density distribution of the particles along x-axis is given in the lower panel compared to the magnetic field (black line).

code from simulating some instability phenomena explicitly. Hence, the higher pressure of electrons will influence the dynamics of the ions via the radial electric field. A direct comparison of the effects of the polytropic index in the simulation with the experimental results is not possible in the current setting as the kinetic treatment of the electrons in the simulation is neglected due to the MHD approximation.

The streak plots in Figure 5.1 show how the magnetic field and the ambient ion density in the plasma evolve along the x-direction, normal to the target. Figure 5.1 a) and b) show the magnetic field changes, and Figure 5.1 c) and d) show the ambient ion density changes as the ablated debris ions interact with the ambient plasma and the magnetic field with different polytropic coefficients. In both cases, the Rankine-Hugoniot conditions for a shock are fulfilled and the reflected ions are seen in the phase space (Figure 5.2). In both  $\gamma_e = 1.67$  and  $\gamma_e = 5$ , the field compression occurs shortly after the ablation of the debris ions when the bulk of debris ions starts to decelerate at  $t \sim 2 \omega_{ci}^{-1}$ . In computer simulations, one observes that most ablated debris ions stop at the cavity edge within a radius of  $10 c/\omega_{pi}$ , but still, a considerable amount of fast ions in front of the compression is pushed further away (Figure 5.4 a). A portion of the debris ion energy is transferred to the magnetic field during coupling, which is compressed and expands as a pulse, but the energy is also deposited in electrons, electric fields, and ambient ions, as well. The change in the magnetic field and the ion density compression are strongly connected to each other as these are caused by the ambient ion dynamics which, in turn, are affected by the change in the electric field and generate the electric current.

The magnetic pulse separates from the debris piston at  $t \sim 3 \omega_{ci}^{-1}$ . For higher  $\gamma_e$ , the velocity of the pulse is almost  $M_A \sim 2.3$ , which is the initial velocity of the debris ions, while, for the adiabatic expansion  $\gamma_e = 5/3$ , the maximum Mach number is about  $2 M_A$ . But it decreases shortly

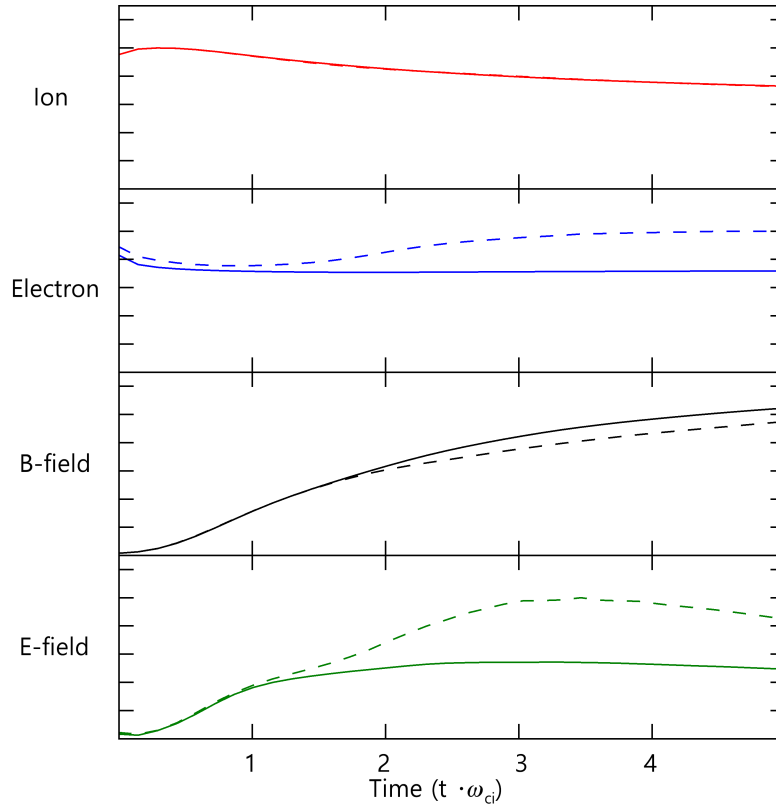


**Figure 5.3:** Temporal energy change of particles and the fields in the simulation for different  $\gamma_e$ . For  $\gamma_e = 5$  (dashed line), electrons and the electric field gain energy compared to  $\gamma_e = 1.67$  (bold line) while a slight decrease in the magnetic field energy is observable. The total ion energy is not affected by the polytropic coefficient.

after the separation of the magnetic pulse from the cavity, and then propagates with a constant velocity. As expected, the density distribution of the ambient ions almost coincides with the magnetic field strength because the Rankine-Hugoniot jump conditions apply not only to the magnetic field, but also to the ambient ion density (Equation 2.9). The energy of the electrons and ambient ions increases when the velocity of the debris ions starts to decrease, but the total ion energy in the simulation is conserved. During the plasma expansion, the ion energy does not change much with  $\gamma_e$ . A slight decrease in magnetic field energy and increase of electric field energy for higher  $\gamma_e$  as well as for the electrons are observed (Figure 5.3). Increasing  $\gamma_e$  has the most effect on the propagation velocity of the magnetic pulse and the ambient density, and makes the third (most inner) peak at the edge of the inner debris ion bulk visible from  $t \sim 4 \omega_{ci}^{-1}$  (Figure 5.4 a). For high  $\gamma_e$ , the outer pulse moves further than in the low  $\gamma_e$  case. As the modification of  $\gamma_e$  does not affect the velocity of the debris ions, one can observe that the fastest debris ions reach about the same distance at  $t = 6 \omega_{ci}^{-1}$  for both  $\gamma_e = 1.67$  and  $\gamma_e = 5$ . But the magnetic pulses separate the outer and inner bulks of these ions differently. In Figure 5.4 b), a double compression of the field is only observed for  $\gamma_e > 1.67$ , which supports our argument of increasing  $\gamma_e$  in the hybrid code because, in a recent experiment, super-Alfvénic, but subcritical collisionless shocks have been observed in a laboratory plasma [Niemann et al., 2014] as well as the double compression of the magnetic field. In space experiments, one observes not only double but also multiple ripples of the field strength in the downstream region. It might be due

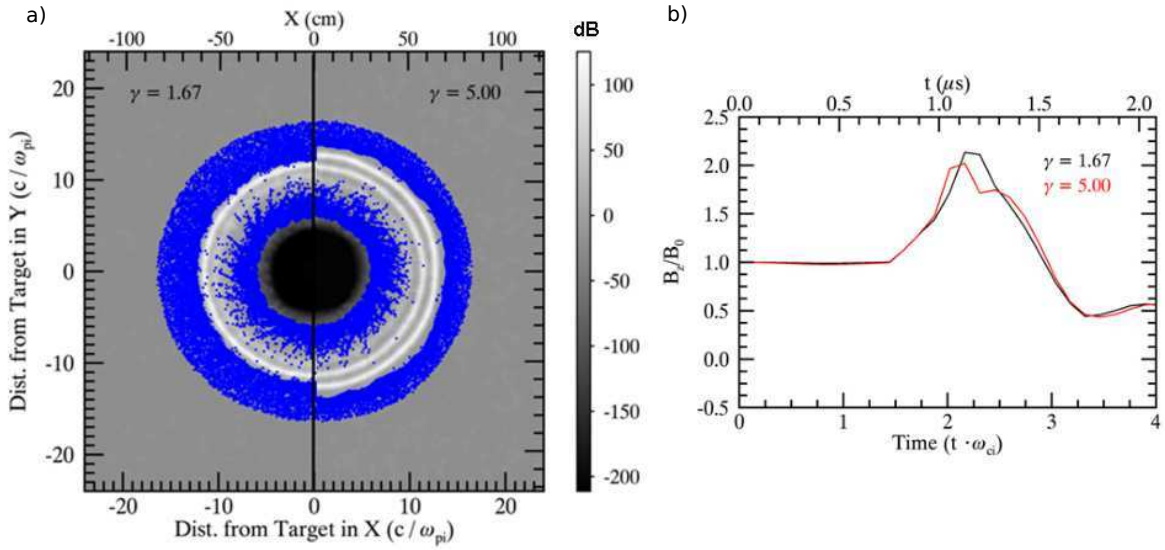


**Figure 5.4:** a) Magnetic field expansion (grayscale) and debris ion distribution (blue dots) for  $\gamma_e = 1.67$  (left) and  $\gamma_e = 5$  (right) at  $t = 6 \omega_{ci}^{-1}$ . b) Double compression of the magnetic field observed in the simulation for  $\gamma_e = 5$  (red).

to the high energy of the shock-wave sources in the supercritical regime, such as supernova remnants or the solar wind [Draine and McKee, 1993, Drury, 1995]. However, a clear explanation of generation of these kinds of double peaks is not given yet. It is still unknown under which condition it appears or what mechanism might cause it experimentally. The diamagnetic cavity size does not seem to be affected by the polytropic coefficient, and the flute-like instability in debris ion density starts to grow at the inner cavity edge in both cases.

Figure 5.5 a) and b) show the electric field peak magnitude change during plasma expansion normalized by the maximal value for  $\gamma_e = 1.67, 3,$  and  $5$  along the radial and azimuthal directions, respectively. Initially, there is almost no change until  $t \sim 2 \omega_{ci}^{-1}$  when the coupling between debris and background ions starts to occur. When the coupling begins and the energy of the debris ions is transferred to the ambient ions and the fields, the maximum value of the radial field increases and that of the azimuthal field decreases. While one can observe a considerable change of strength in the radial field, there is, overall, not much difference in the azimuthal field. The feature presented in the plot around  $t \sim 4 \omega_{ci}^{-1}$  in the azimuthal field plot is a result of the two peaks with alternating maximum values for  $\gamma_e = 5$  as the plot is set to give the maximum value in a given plasma expansion process.

Figure 5.5 c) shows the tendency of the maximum value in radial and azimuthal electric fields for increasing  $\gamma_e$  and the ratio of the two parameters. As already observed in Figure 5.5 a) and b), the strength in the azimuthal direction indicates a slight decrease, but stays mostly constant in the given  $\gamma_e$  range while the radial component increases and so does the ratio of these two magnitudes. One can observe from the electron momentum equation that, by assuming the hybrid approximations, only the radial electric field is affected by changing  $\gamma_e$  to first order. Nonadiabatic increase of electron heating in the shock has already been studied and published in various papers. It is known from space observations that electron heating occurs in the very narrow shock ramp region with large-scale electromagnetic field gradients

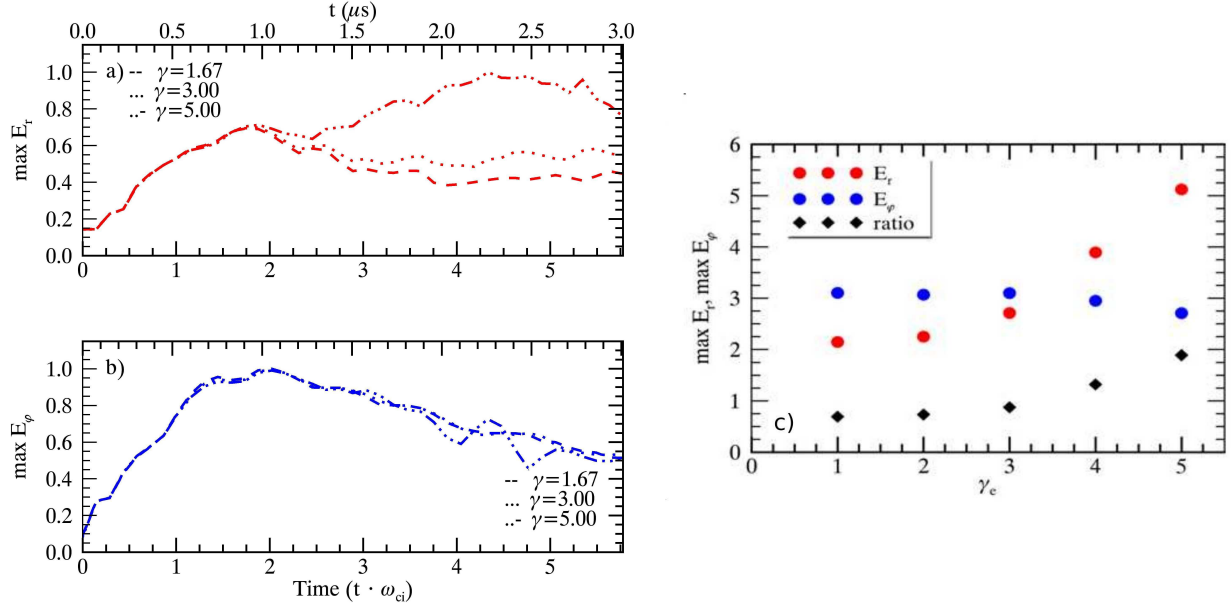


**Figure 5.5:** Evolution of the maximum electric field strength over time along a) radial and b) azimuthal directions, normalized by the maximum strength for  $\gamma_e = 1.67, 3$ , and  $5$ . c) Maximum electric field strength in radial and azimuthal directions and its ratio as a function of increasing  $\gamma_e$ .

[Balikhin and Gedalin, 1994], and the heating is isotropic and nearly adiabatic with  $\gamma_e \sim 2$  [Thomsen et al., 1985]. But it is also assumed that shock transitions might have a different polytropic relation, e.g., dependent on the shock strength. In laboratory experiments, the electron heating could be anisotropic [Feldman, 1985] and strongly nonadiabatic due to partial collisionality, finite lifetime, or different upstream geometries compared with space observations [Thomsen et al., 1985].

## 5.2 Simulation of the experiment

A hybrid simulation based on the LAPD experimental parameters has been run so that a direct comparison of the computational simulation to the experiment could be done. In this section, its results are presented and the deviations from the experimental findings are discussed.

For this purpose, a simulation domain has been set to have 180 cells which span  $16 c/\omega_{pi}$  in both x- and y-direction so that a cell grid has a size of  $0.09 c/\omega_{pi}$  in each dimension. In each cell, there are 100 particles, corresponding  $3.24 \times 10^6$  macro-particles for each species. Debris ions are initialized to be positioned at the center of the domain and expand towards the positive x-axis with their angular velocity  $v \sim \cos^2(\theta)$  where  $\theta$  is the propagation angle in respect to the blow-off axis. This explosion-like spread of particles simulates the laser ablation off the target in the experiment. Here, two groups of debris ions are present with different charge states,  $C^{+4}$  and  $C^{+5}$ , while in experiments, ions of other charge states exist, of course, and should play a role in the expansion dynamics. From the Doppler spectroscopic measurements [Schaeffer et al., 2014], it was found that ions with higher charge states come off the target with a greater velocity. From numerical calculations, the blow-off velocities are estimated to

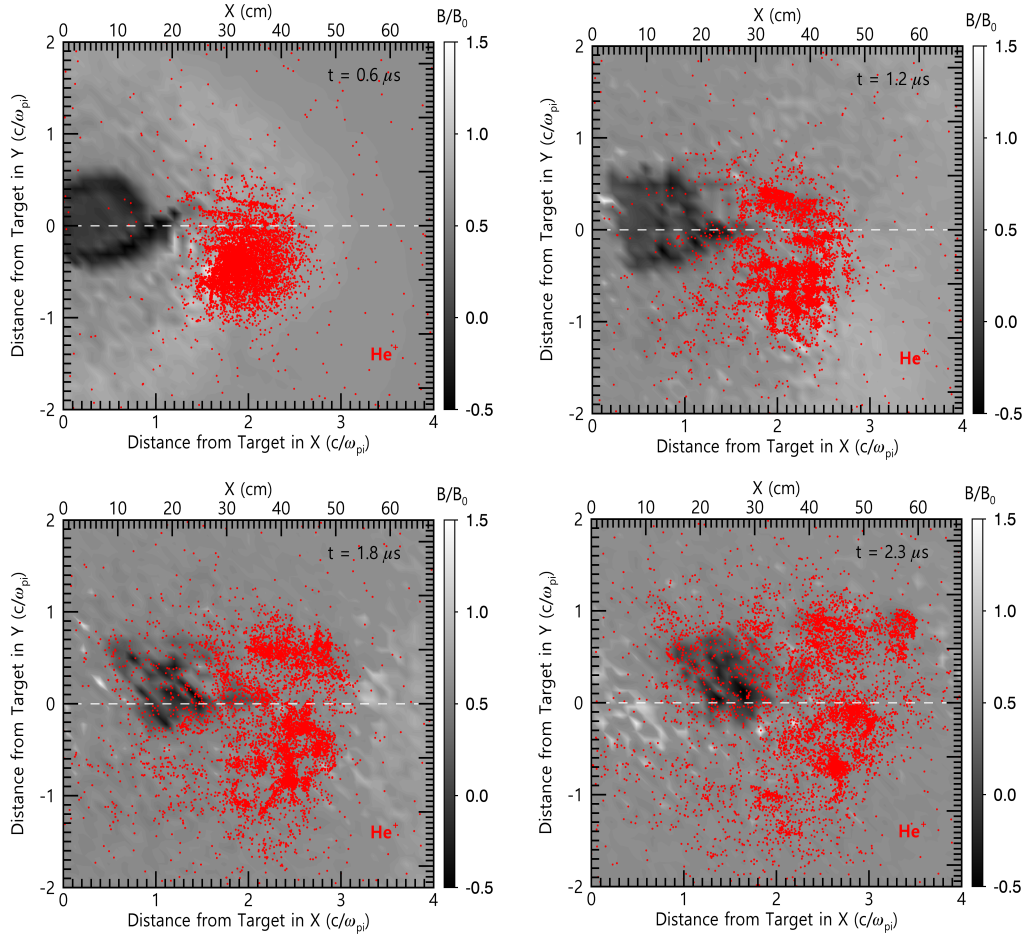


**Figure 5.6:** The temporal change of the ambient plasma distribution in x-y plane overplotted on the background magnetic field (grayscale). The explosion-like expansion of the debris plasma simulating the laser ablation in the real experiment occurs at  $(x, y) = (0, 0)$ . One observes that the background helium plasma ( $\text{He}^+$  - red) is pushed radially as a result of the collisionless coupling to the debris ions.

$0.5 M_A$  and  $2 M_A$ , and the thermal velocities 1250 eV and 1650 eV for  $\text{C}^{+4}$  and  $\text{C}^{+5}$  particles, respectively. Since the hybrid code does not tolerate vacuum, the simulation domain is filled first with a helium plasma ( $\text{He}^+$ ) at a low density of  $0.3 n_i$  where  $n_i$  is the peak density of about  $7.2 \times 10^{12} \text{ cm}^{-3}$ , then with a dense region where the density level reaches the peak value about  $2 c/\omega_{pi}$  ( $\sim 30 \text{ cm}$ ) away from the ablation center. This dense plasma is spread out in a circular shape with a radius of  $0.5 c/\omega_{pi}$  ( $\sim 10 \text{ cm}$ ) representing the small dense plasma region made by the  $\text{LaB}_6$  cathode in the experiment. The ambient ion and electron temperatures are initialized to  $T_i = 1 \text{ eV}$  and  $T_e = 3.2 \text{ eV}$ , the magnetic field to 710 G pointing out of the simulation domain, therefore perpendicular to the x-y plane, and the initial laser energy to 160 J.

Figure 5.6 shows two-dimensional spatial plots of the magnetic field overplotted with the ambient ions in red at four different times. A diamagnetic cavity has been created where its magnetic field is expelled fully from inside, and grows in size. At  $t \sim 1.2 \mu\text{s}$ , the cavity separates from the center of the simulation domain and keeps propagating along the x-axis up to a distance of  $x \sim 1.5 c/\omega_{pi}$ . In the meantime, the magnetic field has started to diffuse back into the cavity.



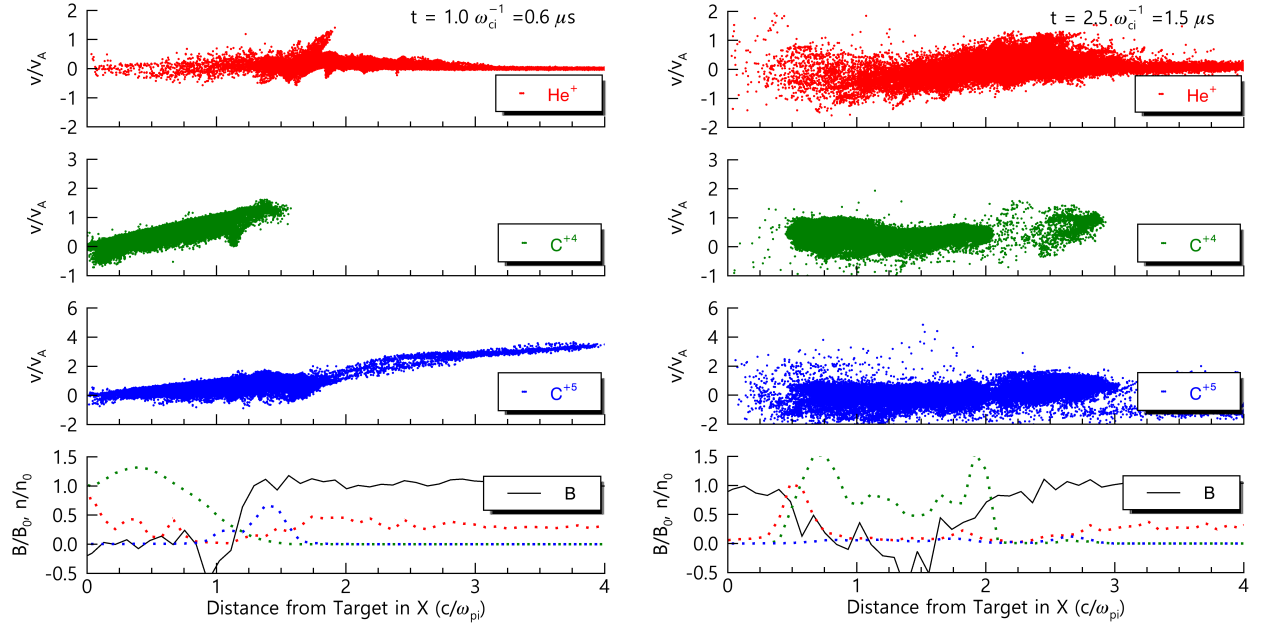


**Figure 5.7:** Diagram at  $t = 1 \omega_{ci}^{-1} = 0.6 \mu s$  (left) and  $t = 2.5 \omega_{ci}^{-1} = 1.5 \mu s$  (right) showing the phase space of the ambient helium ( $\text{He}^+$  - red) as well as the debris plasma with different charge states ( $\text{C}^{+4}$  - green and  $\text{C}^{+5}$  - blue). The heating of the ambient plasma is already seen in the early state of the expansion process as soon as the debris plasma flies throughout the background. The most efficient collisionless coupling occurs at the cavity edge. At later times, the debris plasma slows down while the ambient plasma gains energy and is accelerated towards the positive x-direction. The spatial density distribution plot of the particles along the x-axis is compared to the magnetic field (black line).

It is also displayed how the ambient plasma is pushed radially due to the collisionless energy transfer from the debris ions, similar to the experiment (Figure 4.12 d). Figure 5.7 is a phase space diagram of the distance in x versus the radial velocity of the ambient ( $\text{He}^+$  - red) as well as the debris particles ( $\text{C}^{+4}$  in green and  $\text{C}^{+5}$  in blue). It is noticeable that most of  $\text{C}^{+5}$  seem to escape the cavity without contributing much to the generation of the diamagnetic cavity although a small portion still stays in the cavity with a non-zero radial velocity. The majority of  $\text{C}^{+4}$  stays in the cavity, but as it is visible later at  $t = 2.5 \omega_{ci}^{-1}$ , a small portion which has initially moved slightly ahead of the cavity propagates beyond the edge. The phase space diagram shows that the ambient particles are heated mostly at or in front of the cavity edge. As the cavity advances and the moving  $\text{C}^{+4}$  and  $\text{C}^{+5}$  ions transfer their energy and momentum while they pass throughout the dense plasma region, the heated region expands and more ambient particles are accelerated. At  $t \sim 2.5 \omega_{ci}^{-1}$ , the debris ions have slowed down to  $v \leq v_A$ , compared to the earlier time where the highest velocity goes up to  $2v_A$ . In the meantime, more ambient ions gained in velocity, thus in energy. One interesting aspect to be noted from the simulation result is that there is a region where the magnetic field reaches a negative value as seen in the experiment (Figure 4.1 c). At first glance, it appears to be the area with an accumulation of the debris ions at the cavity edge (a small bump of  $\text{C}^{+5}$  in the density distribution plot at  $t = 1.0 \omega_{ci}^{-1}$ ), but this assumption does not correspond to the later time.



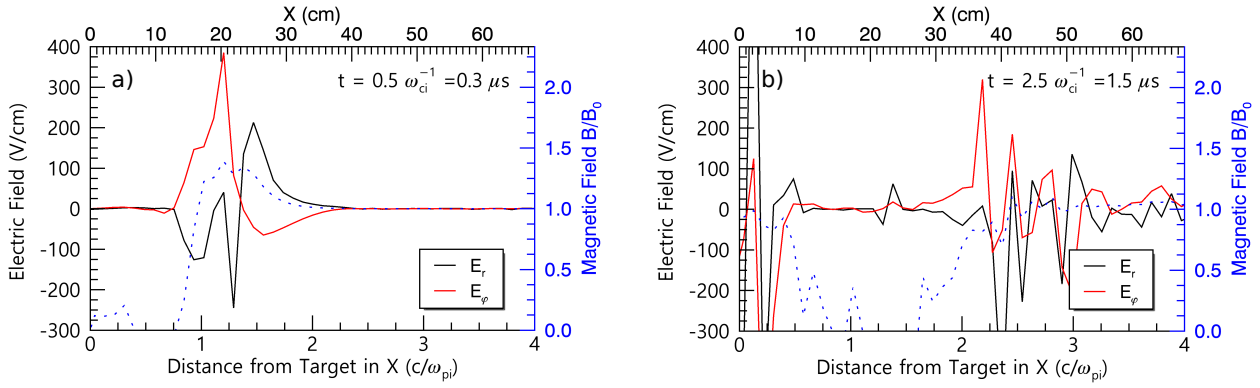


**Figure 5.8:** a) The peak in the radial electric field (black) observed at the front edge of the magnetic compression (blue). It is followed by the rise in the azimuthal electric field (red) which results from the azimuthal current of the debris ions expelling the magnetic field and creating a diamagnetic cavity behind. b) Complex fluctuations in both radial and azimuthal electric field exist at the front as well as the rear edge of the cavity.

Figure 5.8 displays the spatial development of the radial (black) and the azimuthal (red) electric field along the blow-off axis. At  $t \sim 0.5 \omega_{ci}^{-1}$ , a strong radial field in front of the magnetic compression is observed, which might be due to the large density and temperature gradient of the debris plasma accelerating a portion of debris ions into the azimuthal direction in conjunction with the background magnetic field. This radial peak is followed by a spike in the azimuthal field. This plot is similar to the experimental result shown in Figure 4.11. When the debris plasma penetrates the ambient plasma region, large and complex fluctuation patterns are observed in the electric field indicating a mutual interaction and coupling processes occurring between these two plasmas. While the magnetic field diffuses back into the cavity, this kind of large fluctuations can be also generated. At the rear cavity edge near the target, a region which is not measured experimentally, another peak in the electric fields is observed. It might affect or have been already affected by the particle dynamics. According to the phase space plot at  $t = 2.5 \omega_{ci}^{-1}$  (Figure 5.7 right), this fluctuation is accompanied by a density hump. These electric fields might drive the ambient and the debris particles to the cavity edge.

Although several features observed in experiments could be reproduced in the hybrid simulation such as the ion dynamics, the approximations in the simulation code always cause limitations as well as some deviations from the real experiments. Treating electrons as a fluid instead of kinetic particles does not only underestimate the electron temperature, but also changes the overall dynamics of the electric field because it is only generated once a particle is moved due to the charge neutralization. That the debris ions  $C^{+4}$  are confined in the diamagnetic cavity in the simulation is different than the experimental observation as well, indicating the preprogrammed angular velocity distribution has a significant influence on the debris plasmas, thus the cavity dynamics. Although the overall diamagnetic cavity structure is similar to the experiment, the assumed angular velocity might be still differentiate from the reality. Besides, the effect of change in  $\gamma_e$ , as studied in the previous section, is found to be only crucial in a simple cylindrical expansion. In the simulational run as proposed here, the change of the polytropic coefficient did not show any other differences in the results. In future, a better

---

---

understanding about the charge states, proportion, angular velocity distribution of the debris plasma will lead to better simulation results.

---

### 5.3 Summary

---

The two-dimensional hybrid simulations are used to compare numerical predictions to experimental observations. First, a study on the effect of the polytropic coefficient  $\gamma_e$  has been conducted with the goal to compensate the inherent drawback of the simulation due to the neglected electron dynamics. The debris plasma is set to expand cylindrically and is not influenced by changing  $\gamma_e$ . Then a simulation based on experimental parameters has been run. A summary of the findings from these studies is given as follows:

- A super-Alfvénic shock has been created in both cases,  $\gamma_e = 1.67$  and 5, but the high  $\gamma_e$  pushes the pulse as well as the bulk of ambient ions radially further out.
- The structure of the diamagnetic cavity edge and the cavity dynamics are affected by the change of  $\gamma_e$ . For a higher value, a double compression in the magnetic field as well as in the density distribution of the ambient ions is visible, which is a feature also observed occasionally in experiments.
- Significant enhancement of the energy in the electric field and increase of the radial electric field in time are observed while  $E_\varphi$  stays constant even for different  $\gamma_e$ . Experimental electric field measurement will help test the electron model in the hybrid code.
- The ambient ions that are pushed radially outward in experiment were reproduced and their dynamics was observed in the same manner in the simulation, as a result of the collisionless coupling between the ambient and debris plasma.
- The increase of the radial electric field at the front of the magnetic compression followed by the large azimuthal field generated by the debris plasma at an earlier time is similar to the experimental observations. Later, large field fluctuations outside and at the edge of the cavity were seen.
- With a different angular velocity distribution of the debris plasma than a cylindrical expansion,  $\gamma_e$  does not affect the overall dynamics in the simulation much.



---

## 6 Conclusions

---

In this work, a laboratory setting in which a dense laser produced plasma interacts with a pre-formed low-density surrounding plasma under an external magnetic influence is presented. As a result, a diamagnetic cavity is created in which the magnetic field and ambient plasma ions have been expelled and compressed at the edge of the expanding cavity. As the dense plasma expands, the diamagnetic cavity also grows and pushes the compressed magnetic field radially. Its velocity exceeds the magnetosonic speed and, in this experiment, also the Alfvén velocity. One can observe the generated magnetosonic or super-Alfvénic pulse propagating across the magnetic field. The scope of this dissertation was to discuss the structure of diamagnetic cavities produced at different plasma parameters and magnetic field strengths. And the electromagnetic fields generated perpendicular to the applied magnetic field were investigated where the collisionless coupling between the debris and ambient ions takes place.

The basic structure of the diamagnetic cavities produced in the laser energy regime above 50 J is similar to the previous work done at lower energy ( $\sim 30$  J) [Niemann et al., 2013]. The energy conversion efficiency from the laser to the cavity is on the same order of magnitude and found to depend more on the background magnetic field strength. One might conclude that in this laser energy regime, the energy of the diamagnetic cavity has reached its saturation level so that the remaining energy affects the energy dissipation processes differently, leads to a stronger coupling to ambient ions, and gives rise to nonlinear phenomena parallel to the magnetic field. To gain more insight about the micro-physics at the cavity edge, electron emissive probes were used to measure the electric field perpendicular to the applied magnetic field. It is also expected that the electric field measurements in radial and azimuthal direction deliver some experimental evidence of the collisionless coupling between the debris and ambient plasmas due to the laminar ( $E_r$ ) and Larmor ( $E_\varphi$ ) coupling mechanisms as predicted theoretically [Berezin et al., 1998]. In the experiment, the enhancement of the radial electric field at the front edge of the magnetic field compression could be detected near the target, which was also one of the features observed in space [Formisano, 1982, Walker et al., 2004]. The large fluctuations in the electric field measurement at the cavity front were found and are believed to be responsible for the energy dissipation at the ramp of the subcritical shocks. Parallel to the magnetic field, some additional magnetic flux probes were installed to detect Alfvén waves which are also excited by high energetic electrons at the cavity edge via Cherenkov radiation [Van Compernelle et al., 2008]. Different than in previous experiments ( $E_{laser} < 30$  J), the observed Alfvén waves display soliton-like features near the target. It is supposed to be a result from the nonlinear interaction between the energetic electrons and the surrounding magnetized plasma, but this soliton-like feature and the shear wave characteristics ( $\delta B_y > \delta B_z$ ) disappear as one moves further from the target along the blow-off axis, probably via the constructive interference of the waves along the field line or the dispersion of the electric currents in transverse direction. Regarding the diamagnetic cavity, the energy conversion efficiency does not change much despite the seven times higher laser energy. The loss energy might have been distributed to the particle acceleration or the electromagnetic field development as one can see the generation of stronger pulses across the magnetic field, possibly causing a better coupling efficiency to the ambient ions. The soliton-like property of the Alfvén waves can be also described in this

---

---

manner. A better energy conversion efficiency to the Alfvén wave for higher energy has been calculated.

The two-dimensional hybrid simulation can reproduce some features observed in the experiment, such as the diamagnetic cavity expansion, the compressed magnetic field, and the rise of the electric field in this region. The ion dynamics, which is difficult to determine from experiments without the ion density and velocity measurements, can be studied in detail as well as the azimuthal electric field which is responsible for the collisionless coupling for high Mach number shocks. The energy transfer between the debris and ambient particles without collisional effects is observed and also the generated super-Alfvénic pulse which is carried by the ambient ions across the field. Additionally, the effect of the polytropic coefficient  $\gamma_e$  in the hybrid code has been examined for subcritical collisionless shocks to investigate its impact on the ion dynamics and the magnetic field. It has been shown that the nonadiabatic increase in electron temperature induces a double compression of the magnetic field at the edge of the cavity, which has also been observed in experiments. It significantly affects the radial electric field at late times, but has virtually no effect on the azimuthal field.

Although interesting phenomena could be observed in the present experiments, there are still a number of effects such as micro-turbulence at the diamagnetic cavity edges, which need further studies. Even though we observe that the charge state contributing most to the pulse generation is  $C^{+4}$ , it is not known how the debris ions with different charge states affect the process, in which proportion they are ablated from the target surface, or in which angular distribution. The differentially wound magnetic flux probes are accurate within a few percent error and the target misalignment is not a great source of errors due to the long focal length of the final focusing lens used for the laser beam ( $f = 180$  cm). However, the LAPD plasma density in these experiments was determined with an error bar of 25 %. Moreover, the hybrid code is more suited for high Mach number shocks. Because the electron kinetics is neglected, the energy dissipation mechanism occurs via reflected ions instead of the micro-instabilities even in low Mach number regimes. Instabilities in the lower-hybrid frequency range, which are observed in experiments, cannot be demonstrated in the simulation. In addition to that, the shape of the diamagnetic cavity depends on the angular velocity distribution of the debris plasma, which is, as already mentioned, not exactly known.

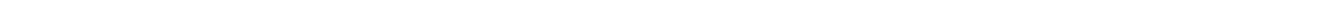
In future, stronger shocks will be launched using the kJ-laser at energies of 500 J and higher in similar experimental configurations. Once a supercritical shock is generated in the laboratory, a variety of questions should be answered such as the dynamics of the reflected ions, which are only known from computational simulations. A direct comparison of laboratory experiments to the *in situ* space data will be possible because stronger shocks are mostly detected in space. Furthermore, diverse diagnostic tools are planned to be applied. For a further study on the electric field, a two-tip electromagnetic probe will be made so that the electric field in the radial and azimuthal direction can be measured simultaneously. The spectroscopy for the Doppler-shift measurements or the Thomson scattering are to be utilized to obtain information about the heating and the flow of the plasma. According to [Wu et al., 1996], a soliton Alfvén wave is accompanied either by a density hump or dip, and this feature also could be verified experimentally in future. Finally, a Thomson parabola might be used to trace the different charge states of the ablated ions from the target and help understand the debris plasma characteristics. When more debris ions are ablated along the magnetic field with sufficient energy, a quasi-parallel shock might be also launched.

---

---

In the introduction, the importance of the study on the interaction between a dense plasma and a low-density magnetized plasma has been emphasized, which has also a connection to the energy science, particularly the nuclear fusion reaction in a magnetic confinement system. In the field of the ignition confinement fusion experiments, which is a different type of nuclear fusion experiments, the magnetic field is found to play an important role, as well. Recently, Perkins *et al.* have proposed in their work on the two-dimensional radiation-hydrodynamic implosion simulation a new ignition experiment in a very high magnetic field of  $\sim 20$  to 100 T in which the compressed magnetic field suppresses the transverse electron heat conduction and inhibits the alpha-particle range so that the alpha particles can couple their energy into the hot spot [Perkins et al., 2013]. As a result, the burning efficiency increased by about 50 % and it has lead to a more efficient ion heating process. They expect that the applied magnetic field will enable the fusion ignition research to progress further.

Although the experimental parameters presented in this work differ from the works on the ITER or the inertial fusion experiments, there are similarities between the physics. These can and will fill the gaps of unknown fields contributing to the advance of this scientific research.





---

---

## Bibliography

---

- [Abel et al., 1997] Abel, G. et al. (1997). Measurements of edge density profiles on TdeV using the injection of laser-ablated lithium atoms. *Review of Scientific Instruments*, 68(1):994–997.
- [Alfvén, 1942] Alfvén, H. (1942). Existence of electromagnetic-hydrodynamic waves. *Nature*, 150:405–406.
- [Balan et al., 2003] Balan, P. et al. (2003). Emissive probe measurements of plasma potential fluctuations in the edge plasma regions of tokamaks. *Review of Scientific Instruments*, 74(3):1583–1587.
- [Bale and Mozer, 2007] Bale, S. and Mozer, F. (2007). Measurement of large parallel and perpendicular electric fields on electron spatial scales in the terrestrial bow shock. *Physical Review Letters*, 98(20):205001.
- [Balikhin and Gedalin, 1994] Balikhin, M. and Gedalin, M. (1994). Kinematic mechanism of electron heating in shocks: Theory vs observations. *Geophysical Research Letters*, 21(9):841–844.
- [Bashurin et al., 1983] Bashurin, V. et al. (1983). The collisionless deceleration of an ionized cloud dispersing in a uniform plasma in a magnetic field. *Journal of Applied Mechanics and Technical Physics*, 24(5):614–620.
- [Berezin et al., 1998] Berezin, Y. et al. (1998). Explosion phenomena in collisionless plasmas at super-Alfvénic speed. *International Journal of Computational Fluid Dynamics*, 10(20):117–126.
- [Bernhardt et al., 1987] Bernhardt, P. et al. (1987). Observations and theory of the AMPTE magnetotail barium releases. *Journal of Geophysical Research: Space Physics (1978–2012)*, 92(A6):5777–5794.
- [Bernstein et al., 1958] Bernstein, I. et al. (1958). An energy principle for hydromagnetic stability problems. *Proceedings of the Royal Society of London. Series A, Mathematical and Physical Sciences*, 244(1236):17–40.
- [Bobin, 1974] Bobin, J. (1974). Nuclear fusion reactions in fronts propagating in solid DT. *Laser Interaction and Related Plasma Phenomena*, pages 465–494.
- [Bobin, 1978] Bobin, T. (1978). Shock waves in collisionless plasmas. *Shock Tube and Shock Wave Research*, 1:156–171.
- [Bodner, 1974] Bodner, S. (1974). Rayleigh-Taylor instability and laser-pellet fusion. *Physical Review Letters*, 33(13):761.
- [Bondarenko et al., 2014] Bondarenko, A. et al. (2014). Spectroscopic measurement of high-frequency electric fields in the interaction of explosive debris plasma with magnetized background plasma. *Physics of Plasmas (1994-present)*, 21(12):122112.

- 
- [Brueckner and Jorna, 1974] Brueckner, K. and Jorna, S. (1974). Laser-driven fusion. *Reviews of Modern Physics*, 46(2):325.
- [Buneman, 1962] Buneman, O. (1962). Instability of electrons drifting through ions across a magnetic field. *Journal of Nuclear Energy. Part C, Plasma Physics, Accelerators, Thermonuclear Research*, 4(2):111.
- [Burgess, 1995] Burgess, D. (1995). Collisionless shocks. In Kivelson, M. and Russel, C., editors, *Introduction to Space Physics*, pages 129–163. Cambridge University Press.
- [Chen, 1984] Chen, F. (1984). *Introduction to Plasma Physics and Controlled Fusion*, volume 1: Plasma Physics. Springer US, 2 edition.
- [Clark et al., 2013] Clark, S. et al. (2013). Hybrid simulation of shock formation for super-Alfvénic expansion of laser ablated debris through an ambient, magnetized plasma. *Physics of Plasmas (1994-present)*, 20(8):082129.
- [Collette and Gekelman, 2010] Collette, A. and Gekelman, W. (2010). Structure of an exploding laser-produced plasma. *Physical Review Letters*, 105(19):195003.
- [Constantin et al., 2009] Constantin, C. et al. (2009). Collisionless interaction of an energetic laser produced plasma with a large magnetoplasma. *Astrophysics and Space Science*, 322(1-4):155–159.
- [Cooper et al., 2010] Cooper, C. et al. (2010). A new large area lanthanum hexaboride plasma source. *Review of Scientific Instruments*, 81(8):083503.
- [Cramer, 2011] Cramer, N. (2011). *The Physics of Alfvén Waves*. John Wiley & Sons.
- [Davidson and Ogden, 1975] Davidson, R. and Ogden, J. (1975). Electromagnetic ion cyclotron instability driven by ion energy anisotropy in high-beta plasmas. *Physics of Fluids (1958-1988)*, 18(8):1045–1050.
- [Dawson, 1964] Dawson, J. (1964). On the production of plasma by giant pulse lasers. *Physics of Fluids (1958-1988)*, 7(7):981–987.
- [Dimonte and Wiley, 1991] Dimonte, G. and Wiley, L. (1991). Dynamics of exploding plasmas in a magnetic field. *Physical Review Letters*, 67(13):1755.
- [Draine and McKee, 1993] Draine, B. T. and McKee, C. F. (1993). Theory of interstellar shocks. *Annual Review of Astronomy and Astrophysics*, 31:373–432.
- [Drake, 2000] Drake, R. (2000). The design of laboratory experiments to produce collisionless shocks of cosmic relevance. *Physics of Plasmas (1994-present)*, 7(11):4690–4698.
- [Drury, 1995] Drury, L. (1995). Supernova remnant shocks. *Advances in Space Research*, 15(8):481–487.
- [Dyal, 2006] Dyal, P. (2006). Particle and field measurements of the Starfish diamagnetic cavity. *Journal of Geophysical Research: Space Physics (1978–2012)*, 111(A12).
- [Eastwood et al., 2007] Eastwood, J. et al. (2007). Contributions to the cross shock electric field at a quasiperpendicular collisionless shock. *Geophysical Research Letters*, 34(17).

- 
- 
- [Everson et al., 2009] Everson, E. et al. (2009). Design, construction, and calibration of a three-axis, high-frequency magnetic probe (B-dot probe) as a diagnostic for exploding plasmas. *Review of Scientific Instruments*, 80(11):113505.
- [Feldman, 1985] Feldman, W. C. (1985). Electron velocity distributions near collisionless shocks. *Collisionless Shocks in the Heliosphere: Reviews of Current Research*, pages 195–205.
- [Fishman et al., 1960] Fishman, F. et al. (1960). Magnetohydrodynamic shock wave in a collision-free plasma. *Reviews of Modern Physics*, 32(4):959.
- [Formisano, 1982] Formisano, V. (1982). Measurement of the potential drop across the Earth's collisionless bow shock. *Geophysical Research Letters*, 9(9):1033–1036.
- [Freidberg, 1987] Freidberg, J. (1987). *Ideal Magnetohydrodynamics*. Modern Perspectives in Energy. Prentice Hall.
- [Gary and Sgro, 1990] Gary, S. and Sgro, A. (1990). The lower hybrid drift instability at the magnetopause. *Geophysical Research Letters*, 17(7):909–912.
- [Gekelman, 1999] Gekelman, W. (1999). Review of laboratory experiments on Alfvén waves and their relationship to space observations. *Journal of Geophysical Research: Space Physics (1978–2012)*, 104(A7):14417–14435.
- [Gekelman et al., 1991] Gekelman, W. et al. (1991). Design, construction, and properties of the large plasma research device - The LAPD at UCLA. *Review of Scientific Instruments*, 62(12):2875–2883.
- [Gekelman et al., 1997a] Gekelman, W. et al. (1997a). Experimental observations of shear Alfvén waves generated by narrow current channels. *Plasma Physics and Controlled Fusion*, 39(5A):A101.
- [Gekelman et al., 1997b] Gekelman, W. et al. (1997b). Laboratory experiments on shear Alfvén waves and their relationship to space plasmas. *Journal of Geophysical Research: Space Physics (1978–2012)*, 102(A4):7225–7236.
- [Gekelman et al., 2003] Gekelman, W. et al. (2003). Laboratory experiments on Alfvén waves caused by rapidly expanding plasmas and their relationship to space phenomena. *Journal of Geophysical Research: Space Physics (1978–2012)*, 108(A7).
- [Gekelman et al., 2011] Gekelman, W. et al. (2011). The many faces of shear Alfvén waves. *Physics of Plasmas (1994-present)*, 18(5):055501.
- [Golubev et al., 1979] Golubev, A. et al. (1979). Collisionless dispersion of an ionized cloud into a homogeneous magnetized plasma. *PMTF Zhurnal Prikladnoi Mekhaniki i Tekhnicheskoi Fiziki*, 19:33–42.
- [Goodrich and Scudder, 1984] Goodrich, C. and Scudder, J. (1984). The adiabatic energy change of plasma electrons and the frame dependence of the cross-shock potential at collisionless magnetosonic shock waves. *Journal of Geophysical Research: Space Physics (1978–2012)*, 89(A8):6654–6662.

- 
- [Greenstadt and Mellott, 1987] Greenstadt, E. and Mellott, M. (1987). Plasma wave evidence for reflected ions in front of subcritical shocks: ISEE 1 and 2 observations. *Journal of Geophysical Research: Space Physics (1978–2012)*, 92(A5):4730–4734.
- [Grun et al., 1981] Grun, J. et al. (1981). Characteristics of ablation plasma from planar, laser-driven targets. *Applied Physics Letters*, 39(7):545–547.
- [Hasegawa and Mima, 1976] Hasegawa, A. and Mima, K. (1976). Exact solitary Alfvén wave. *Physical Review Letters*, 37(11):690.
- [Heidbrink, 2008] Heidbrink, W. (2008). Basic physics of Alfvén instabilities driven by energetic particles in toroidally confined plasmas. *Physics of Plasmas (1994–present)*, 15(5):055501.
- [Hershkowitz et al., 1983] Hershkowitz, N. et al. (1983). Self-emissive probes. *Review of Scientific Instruments*, 54(1):29–34.
- [Hewett et al., 2011] Hewett, D. W. et al. (2011). The physics of ion decoupling in magnetized plasma expansions. *Journal of Geophysical Research: Space Physics (1978–2012)*, 116(A11).
- [Huba, 2004] Huba, J. (2004). Naval Reserach Laboratory: Plasma formulary.
- [Huba et al., 1987] Huba, J. et al. (1987). Theory and simulation of the Rayleigh-Taylor instability in the limit of large Larmor radius. *Physical Review Letters*, 59(26):2971.
- [ITER, 2013] ITER (2013). [www.iter.org](http://www.iter.org). *International Thermonuclear Experimental Reactor*.
- [Jackson, 1962] Jackson, J. (1962). *Classical Electrodynamics*, volume 3. Wiley New York.
- [Kacenjar et al., 1986] Kacenjar, S. et al. (1986). Magnetic field compression and evolution in laser-produced plasma expansions. *Physics of Fluids (1958-1988)*, 29(6):2007–2012.
- [Kemp and Sellen, 1966] Kemp, R. and Sellen, J. J. (1966). Plasma potential measurements by electron emissive probes. *Review of Scientific Instruments*, 37(4):455–461.
- [Key et al., 1983] Key, M. et al. (1983). A study of ablation by laser irradiation of plane targets at wavelengths 1.05, 0.53, and 0.35  $\mu\text{m}$ . *Physics of Fluids (1958-1988)*, 26(7):2011–2026.
- [Krall et al., 1971] Krall, N. et al. (1971). Low-frequency instabilities in magnetic pulses. *Physical Review A*, 4(5):2094.
- [Krimigis et al., 1982] Krimigis, S. et al. (1982). The Active Magnetospheric Particle Tracer Explorers (AMPTE) program. *Eos, Transactions American Geophysical Union*, 63(45):843–850.
- [Langmuir, 1923] Langmuir, I. (1923). The pressure effect and other phenomena in gaseous discharges. *Journal of the Franklin Institute*, 196(751):6.
- [Lee et al., 2015] Lee, B. et al. (2015). Effect of electron pressure on debris-ambient coupling in a magnetized collisionless shock. *Plasma Science, IEEE Transactions on*, 43(5):1815–1819.
- [Lembège et al., 2004] Lembège, B. et al. (2004). Selected problems in collisionless-shock physics. *Space Science Reviews*, 110(3-4):161–226.

- 
- [Leneman et al., 1999] Leneman, D. et al. (1999). Laboratory observations of shear Alfvén waves launched from a small source. *Physical Review Letters*, 82(13):2673.
- [Leneman et al., 2006] Leneman, D. et al. (2006). The plasma source of the large plasma device at University of California, Los Angeles. *Review of Scientific Instruments*, 77(1):015108.
- [Leroy, 1983] Leroy, M. (1983). Structure of perpendicular shocks in collisionless plasma. *Physics of Fluids (1958-1988)*, 26(9):2742–2753.
- [Louarn et al., 1994] Louarn, P et al. (1994). Observation of kinetic Alfvén waves by the FREJA spacecraft. *Geophysical Research Letters*, 21(17):1847–1850.
- [Lühr et al., 1986] Lühr, H. et al. (1986). In situ magnetic field measurements during AMPTE solar wind Li<sup>+</sup> releases. *Journal of Geophysical Research: Space Physics (1978–2012)*, 91(A2):1261–1270.
- [Lundin et al., 1995] Lundin, R. et al. (1995). *The Freja Science Mission*. Springer.
- [Marshall, 1955] Marshall, W. (1955). The structure of magneto-hydrodynamic shock waves. *Proceedings of the Royal Society of London A: Mathematical, Physical and Engineering Sciences*, 233(1194):367–376.
- [Martin et al., 2015] Martin, M., Bonde, J., et al. (2015). A resistively heated CeB<sub>6</sub> emissive probe. *Review of Scientific Instruments*, 86(5):053507.
- [McBride et al., 1972] McBride, J. et al. (1972). Theory and simulation of turbulent heating by the modified two-stream instability. *Physics of Fluids (1958-1988)*, 15(12):2367–2383.
- [Meister et al., 2014] Meister, C.-V. et al. (2014). The influence of boundary conditions on the excitation of instabilities in magnetohydrodynamic systems. *Journal of Physics: Conference Series*, 529(1):012018.
- [Meyer and Thiell, 1984] Meyer, B. and Thiell, B. (1984). Experimental scaling laws for ablation parameters in plane target–laser interaction with 1.06  $\mu\text{m}$  and 0.35  $\mu\text{m}$  laser wavelengths. *Physics of Fluids (1958-1988)*, 27(1):302–311.
- [Mikhailovskii, 1974] Mikhailovskii, A. (1974). *Theory of Plasma Instabilities (Consultants Bureau, New York, 1974)*, volume 1.
- [Miura, 2007] Miura, A. (2007). A magnetospheric energy principle for hydromagnetic stability problem. *Journal of Geophysical Research -All Series-*, 112(A06234).
- [Miura, 2011] Miura, A. (2011). A magnetospheric energy principle extended to include neutral atmosphere. *Physics of Plasmas*, 18(032904).
- [Miura, 2013] Miura, A. (2013). Magnetospheric energy principle for spherically symmetric monopolar magnetospheres. *Physical Review Letters*, 110(21):215001.
- [Mjølhus and Wyller, 1986] Mjølhus, E. and Wyller, J. (1986). Alfvén solitons. *Physica Scripta*, 33(5):442.
- [Mundt et al., 1987] Mundt, R. et al. (1987). Jets from young stars-CCD imaging, long-slit spectroscopy, and interpretation of existing data. *The Astrophysical Journal*, 319:275–303.



- 
- [Ness and Wilcox, 1964] Ness, N. F. and Wilcox, J. M. (1964). Solar origin of the interplanetary magnetic field. *Physical Review Letters*, 13(15):461.
- [NFRI, 2015] NFRI (2015). [www.nfri.re.kr](http://www.nfri.re.kr). *Nuclear Fusion Research Institute (KSTAR project)*.
- [Niemann et al., 2012] Niemann, C. et al. (2012). High-energy Nd: glass laser facility for collisionless laboratory astrophysics. *Journal of Instrumentation*, 7(03):P03010.
- [Niemann et al., 2013] Niemann, C. et al. (2013). Dynamics of exploding plasmas in a large magnetized plasma. *Physics of Plasmas (1994-present)*, 20(1):012108.
- [Niemann et al., 2014] Niemann, C. et al. (2014). Observation of collisionless shocks in a large current-free laboratory plasma. *Geophysical Research Letters*, 41(21):7413–7418.
- [Papadopoulos et al., 1971] Papadopoulos, K. et al. (1971). Heating of counterstreaming ion beams in an external magnetic field. *Physics of Fluids (1958-1988)*, 14(4):849–857.
- [Perkins et al., 2013] Perkins, L. et al. (2013). Two-dimensional simulations of thermonuclear burn in ignition-scale inertial confinement fusion targets under compressed axial magnetic fields. *Physics of Plasmas (1994-present)*, 20(7):072708.
- [Petschek, 1958] Petschek, H. (1958). Aerodynamic dissipation. *Reviews of Modern Physics*, 30(3):966.
- [Plechaty et al., 2013] Plechaty, C. et al. (2013). Focusing of an explosive plasma expansion in a transverse magnetic field. *Physical Review Letters*, 111(18):185002.
- [Princeton\_Instruments, 2015] Princeton\_Instruments (2015). <http://www.princetoninstruments.com/products/imcam/pimax/>. *Princeton Instruments Acton*.
- [Richardson et al., 2000] Richardson, I. et al. (2000). Sources of geomagnetic activity over the solar cycle: Relative importance of coronal mass ejections, high-speed streams, and slow solar wind. *Journal of Geophysical Research -All Series-*, 105(A8):18–203.
- [Ripin et al., 1993] Ripin, B. et al. (1993). Sub-Alfvénic plasma expansion. *Physics of Fluids B: Plasma Physics (1989-1993)*, 5(10):3491–3506.
- [Rose and Clark, 1961] Rose, D. and Clark, M. (1961). *Plasmas and Controlled Fusion*. MIT Press.
- [Russell, 2005] Russell, C. (2005). An introduction to the physics of collisionless shocks. *The Physics of Collisionless Shocks*, 781:3–14.
- [Sagdeev, 1966] Sagdeev, R. (1966). Cooperative phenomena and shock waves in collisionless plasmas. *Reviews of Plasma Physics*, 4(23).
- [Schaeffer, 2014] Schaeffer, D. (2014). *Generation of quasi-perpendicular collisionless shocks by a laser-driven magnetic piston*. PhD thesis, University of California, Los Angeles.
- [Schaeffer et al., 2014] Schaeffer, D. et al. (2014). Laser-driven, magnetized quasi-perpendicular collisionless shocks on the Large Plasma Device. *Physics of Plasmas (1994-present)*, 21(5):056312.

- 
- [Schrittwieser et al., 2008] Schrittwieser, R. et al. (2008). Laser-heated emissive plasma probe. *Review of Scientific Instruments*, 79(8):083508.
- [Scudder et al., 1986] Scudder, J. et al. (1986). The resolved layer of a collisionless, high  $\beta$ , supercritical, quasi-perpendicular shock wave: 1. Rankine-Hugoniot geometry, currents, and stationarity. *Journal of Geophysical Research: Space Physics (1978–2012)*, 91(A10):11019–11052.
- [Shapiro and Üçer, 2003] Shapiro, V. and Üçer, D. (2003). Shock surfing acceleration. *Planetary and Space Science*, 51(11):665–680.
- [Shukla et al., 1982] Shukla, P. et al. (1982). Alfvén soliton in a low-beta plasma. *Journal of Plasma Physics*, 28(01):125–131.
- [Shukla and Stenflo, 1995] Shukla, P. and Stenflo, L. (1995). Nonlinear Alfvén waves. *Physica Scripta*, 1995(T60):32.
- [Singh et al., 1990] Singh, R. et al. (1990). Theoretical model for deposition of superconducting thin films using pulsed laser evaporation technique. *Journal of Applied Physics*, 68(1):233–247.
- [Spatschek, 1990] Spatschek, K. (1990). *Theoretische Plasmaphysik*. Teubner Studienbücher.
- [Stasiewicz et al., 1997] Stasiewicz, K. et al. (1997). Cavity resonators and Alfvén resonance cones observed on Freja. *Journal of Geophysical Research: Space Physics (1978–2012)*, 102(A2):2565–2575.
- [Stasiewicz et al., 2000] Stasiewicz, K. et al. (2000). Small scale Alfvénic structure in the aurora. *Space Science Reviews*, 92(3-4):423–533.
- [Stix, 1978] Stix, T. (1978). Plasma transport across a braided magnetic field. *Nuclear Fusion*, 18(3):353.
- [Stringer, 1964] Stringer, T. (1964). Electrostatic instabilities in current-carrying and counter-streaming plasmas. *Journal of Nuclear Energy. Part C, Plasma Physics, Accelerators, Thermonuclear Research*, 6(3):267.
- [Sturrock, 1996] Sturrock, P. (1996). *Plasma Physics*. Cambridge University Press.
- [Taylor et al., 1999] Taylor, P. et al. (1999). Disruption mitigation studies in DIII-D. *Physics of Plasmas (1994-present)*, 6(5):1872–1879.
- [Thomas and Brecht, 1986] Thomas, V. and Brecht, S. (1986). Two-dimensional simulation of high Mach number plasma interactions. *Physics of Fluids (1958-1988)*, 29(8):2444–2454.
- [Thomsen et al., 1985] Thomsen, M. et al. (1985). Ion and electron heating at collisionless shocks near the critical Mach number. *Journal of Geophysical Research: Space Physics (1978–2012)*, 90(A1):137–148.
- [Tidman and Krall, 1971] Tidman, D. and Krall, N. (1971). *Shock waves in collisionless plasmas*. Wiley-Interscience New York.



- 
- [Tonks and Langmuir, 1929] Tonks, L. and Langmuir, I. (1929). A general theory of the plasma of an arc. *Physical Review*, 34(6):876.
- [Torrence and Compo, 1998] Torrence, C. and Compo, G. (1998). A practical guide to wavelet analysis. *Bulletin of the American Meteorological Society*, 79(1):61–78.
- [Treumann, 2009] Treumann, R. (2009). Fundamentals of collisionless shocks for astrophysical application, 1. Non-relativistic shocks. *The Astronomy and Astrophysics Review*, 17(4):409–535.
- [Vampola, 1992] Vampola, A. (1992). Combined release and radiation effects satellite. *Journal of Spacecraft and Rockets*, 29(4):555.
- [Van Compernelle et al., 2005] Van Compernelle, B. et al. (2005). Generation of Alfvén waves by high power pulse at the electron plasma frequency. *Geophysical Research Letters*, 32(8).
- [Van Compernelle et al., 2008] Van Compernelle, B. et al. (2008). Cherenkov radiation of shear Alfvén waves. *Physics of Plasmas (1994-present)*, 15(8):082101.
- [VanZeeland, 2003] VanZeeland, M. (2003). *Generation of shear Alfvén waves by expanding plasmas*. PhD thesis, University of California, Los Angeles.
- [VanZeeland et al., 2001] VanZeeland, M. et al. (2001). Production of Alfvén waves by a rapidly expanding dense plasma. *Physical Review Letters*, 87(10):105001.
- [VanZeeland et al., 2003] VanZeeland, M. et al. (2003). Currents and shear Alfvén wave radiation generated by an exploding laser-produced plasma: Perpendicular incidence. *Physics of Plasmas (1994-present)*, 10(5):1243–1252.
- [VanZeeland and Gekelman, 2004] VanZeeland, M. and Gekelman, W. (2004). Laser-plasma diamagnetism in the presence of an ambient magnetized plasma. *Physics of Plasmas (1994-present)*, 11(1):320–323.
- [Vincena et al., 2008] Vincena, S. et al. (2008). Quasielectrostatic whistler wave radiation from the hot electron emission of a laser-produced plasma. *Physics of Plasmas (1994-present)*, 15(7):072114.
- [Wahlund et al., 1994] Wahlund, J.-E. et al. (1994). Observations of ion acoustic fluctuations in the auroral topside ionosphere by the FREJA S/C. *Geophysical Research Letters*, 21(17):1835–1838.
- [Walker et al., 2004] Walker, S. et al. (2004). Electric field scales at quasi-perpendicular shocks. *Annales Geophysicae*, 22(7):2291–2300.
- [Wilkinson, 2003] Wilkinson, W. (2003). The Earth’s quasi-parallel bow shock: Review of observations and perspectives for Cluster. *Planetary and Space Science*, 51(11):629–647.
- [Winske, 1989] Winske, D. (1989). Development of flute modes on expanding plasma clouds. *Physics of Fluids B: Plasma Physics (1989-1993)*, 1(9):1900–1910.
- [Winske, 1996] Winske, D. (1996). Regimes of the magnetized Rayleigh–Taylor instability. *Physics of Plasmas (1994-present)*, 3(11):3966–3974.

- 
- 
- [Winske et al., 1985] Winske, D. et al. (1985). Plasma heating at collisionless shocks due to the kinetic cross-field streaming instability. *Journal of Geophysical Research: Space Physics (1978–2012)*, 90(A1):123–136.
- [Winske and Gary, 2007] Winske, D. and Gary, S. (2007). Hybrid simulations of debris-ambient ion interactions in astrophysical explosions. *Journal of Geophysical Research: Space Physics (1978–2012)*, 112(A10).
- [Winske and Omid, 1993] Winske, D. and Omid, N. (1993). Hybrid codes. *Computer Space Plasma Physics: Simulation Techniques and Software*, pages 103–160.
- [Wong, 1970] Wong, H. (1970). Electrostatic Electron-Ion Streaming Instability. *Physics of Fluids (1958-1988)*, 13(3):757–760.
- [Wright, 1971] Wright, T. (1971). Early-time model of laser plasma expansion. *Physics of Fluids (1958-1988)*, 14(9):1905–1910.
- [Wu, 1982] Wu, C. (1982). Physical mechanisms for turbulent dissipation in collisionless shock waves. *Space Science Reviews*, 32(1-2):83–97.
- [Wu et al., 1984] Wu, C. et al. (1984). Microinstabilities associated with a high Mach number, perpendicular bow shock. *Space Science Reviews*, 37(1-2):63–109.
- [Wu et al., 1996] Wu, D. et al. (1996). Solitary kinetic Alfvén waves in the two-fluid model. *Physics of Plasmas (1994-present)*, 3(8):2879–2884.
- [Wygant et al., 1987] Wygant, J. et al. (1987). Electric field measurements at subcritical, oblique bow shock crossings. *Journal of Geophysical Research: Space Physics (1978–2012)*, 92(A10):11109–11121.
- [Zakharov, 2003] Zakharov, Y. P. (2003). Collisionless laboratory astrophysics with lasers. *Plasma Science, IEEE Transactions on*, 31(6):1243–1251.
- [Zakharov et al., 1986] Zakharov, Y. P. et al. (1986). Effectiveness of slowing of expanding clouds of diamagnetic plasma by magnetic field (experimental). *Soviet Journal of Plasma Physics*, 12.
- [Zakharov et al., 2003] Zakharov, Y. P. et al. (2003). Laboratory simulation of the dynamics and instabilities of space plasma clouds exploding in magnetized background. *Proc. 3rd Int. Conf. Inertial Fusion Sciences and Applications*.



---

---

## Publications

---

---

### Peer-reviewed

---

- 1) B.R. Lee, S.E. Clark, D.H.H. Hoffmann, C. Niemann, *Effect of electron pressure on debris-ambient coupling in a magnetized collisionless shock*, IEEE Transactions on Plasma Science (2015), 43, 5, 1815-1819
- 2) C.V. Meister, B.R. Lee, D.H.H. Hoffmann, *The influence of boundary conditions on the excitation of instabilities in magnetohydrodynamic systems*, Journal of Physics: Conference Series 529 (2014), 012018
- 3) B.R. Lee, A. Bondarenko, S.E. Clark, C. Constantin, E. Everson, D. Schaeffer, D.H.H. Hoffmann, C. Niemann, *Collisionless interactions of a laser produced plasma with a magnetized low-density plasma* (in preparation)

---

### Reports

---

- 1) B.R. Lee, S.E. Clark, A. Bondarenko, C. Constantin, E. Everson, D.H.H. Hoffmann, D. Schaeffer, C. Niemann, *Electric field measurement of laser-produced plasma in a tenuous, current-free, large plasma*, New Annual Report News and Reports from High Energy Density generated by Heavy iOn and Laser Beams 2013-2014, GSI-2015-2 Report, (Apr. 2015)
- 2) C.-V. Meister, T. Haase, B.R. Lee, D.H.H. Hoffmann, *Application of the energy principle of magnetohydrodynamics to fusion and lightning plasmas*, New Annual Report News and Reports from High Energy Density generated by Heavy iOn and Laser Beams 2013-2014, GSI-2015-2 Report, (Apr. 2015)

---

## Konferenzbesuche

---

---

### Vortrag

---

- 1) The 9th International Conference on Inertial Fusion Sciences and Applications in Seattle, Washington, USA (20.-25. Sep. 2015)  
*Magnetic and electric field measurement of a laser produced plasma expanding through a magnetized background plasma*
- 2) DPG Frühjahrstagung 2015 in Bochum (2.-5. Mär. 2015)  
*Electric field development and ion dynamics at the magnetic cavity edge of laser produced plasma expansion*
- 3) 35th International Workshop on Physics of High Energy Density in Matter in Hirschegg, Österreich (26.-30. Jan. 2015)  
*Generation of magnetized collisionless shock in a large laboratory plasma*
- 4) 56th Annual Meeting of the APS Division of Plasma Physics in New Orleans, LA, USA (27.-31. Okt. 2014)  
*Effect of the polytropic coefficient in 2D hybrid simulations of laser-produced plasma expansion*

---

### Postervortrag

---

- 1) The 41st IEEE International Conference on Plasma Science and the 20th International Conference on High-Power Particle Beams in Washington DC, USA (25.-29. Mai 2014)  
*Effects of different electron pressure on plasma expansion*
- 2) 17th international conference on recent progress in many-body theories in Rostock (08.-13. Sep. 2013)  
*Magnetohydrodynamic energy principle for fusion plasmas and magnetospheres*
- 3) European Geosciences Union General Assembly 2013 in Wien, Österreich (07.-12. Apr. 2013)  
*Detection of variations of VLF/LF signals generated by lightning strokes and its analysis*
- 4) 5. Darmstädter Energiekonferenz-Komplexität der Energiewende in Darmstadt (28. Feb. 2013)  
*Magnetohydrodynamic energy principle for nuclear fusion matter and the plasma of the Earth's ionosphere*
- 5) 33rd International Workshop on Physics of High Energy Density in Matter in Hirschegg, Österreich (13.-18. Jan. 2013)  
*VLF signals influenced by meteorological effects*

---

---

## Danksagung

---

An dieser Stelle möchte ich die Gelegenheit nutzen allen zu danken, die mir bei der Durchführung dieser Promotionsarbeit eine große Hilfe waren.

Mein erster Dank gilt Herrn Prof. Dr. Dr. h.c./RUS Dieter H.H. Hoffmann für die Aufnahme in seine Arbeitsgruppe seit dem Masterstudium, die Überlassung dieser Arbeit und die wissenschaftliche, aber auch seelische Unterstützung, ohne die ich diese Arbeit überhaupt nicht fertigstellen konnte.

Großer Dank geht auch an Herrn Prof. Dr. Christoph Niemann, der mich gerne als seine zusätzliche Doktorandin aufgenommen und mir durch das sehr gut gelungene Experiment (trotz einiger unerwarteten Ereignissen mit den Magnetfeldern oder mit der Kathode am LAPD) das interessanteste Jahr während der Promotionsphase ermöglicht hat.

Hiermit danke ich auch Frau Prof. Dr. Barbara Drossel und Herrn Prof. Dr. Walther, die sich gerne als Prüfer eingesetzt haben.

Bei den beiden Wissenschaftlerinnen, Frau Dr. habil. C.-V. Meister und Dr. Carmen Constantin, möchte ich mich bedanken, die mir nicht nur bei der Arbeit geholfen haben, sondern auch zeigten, wie man sich als eine Frau in der Wissenschaft präsentieren soll.

Besonderer Dank geht an die Darmstädter Exzellenz-Graduiertenschule Energiewissenschaft und Energietechnik für die finanzielle Unterstützung in den letzten drei Jahren. Nicht nur die Forschung, sondern auch die „Pflichten und Rechten“ der Stipendiaten haben zu einer persönlichen Weiterentwicklung geführt. Hiermit danke ich Herrn Prof. Dr. Volker Hinrichsen für sein Engagement als mein Zweitbetreuer und Frau Dr. Tanja Drobek und Frau Heide Rinnert, die nicht nur jeder Zeit mir alles zur Verfügung stellten, die ich brauchte, sondern auch sehr viel Interesse sowohl an meiner Arbeit als auch an meiner persönlichen Karriere gezeigt haben.

Frau Prof. Sung-Ock Sohn von der University of California, Los Angeles, möchte ich mich auch herzlich bedanken für ihre wissenschaftlichen und geistlichen Ratschläge und Ermutigungen, durch die ich einen weiteren Wendepunkt meiner wissenschaftlichen Bahn erlebt habe.

Alle Mitglieder der AG Hoffmann, AG Niemann und Mitpromovierende der Graduiertenschule ESE danke ich für die gemeinsame Arbeit und wertvollen Erfahrungen in einer Zeit voller Höhen und Tiefen.

Technischen Mitarbeitern der University of California, Los Angeles, deren Namen ich leider nicht alle kenne, danke ich für ihre Hilfe, da ohne sie die Experimente und diese Arbeit nicht zustande gekommen wären.

Hiermit danke ich auch meinen Freunden, die immer für mich beteten und geistlich ermutigt haben, insbesondere Yi-Rang, meiner besten Freundin, die zusammen mit mir diesen Weg lief.

Ohne meine Familie hätte ich die Promotion nicht bis zum Ende schaffen können. Ich danke meinen Eltern, Hyun Sook und Kwang Sun, die mich in all den Jahren auf vielfältige Art unterstützt und mir dieses Studium und diverse Erfahrungen ermöglicht haben. Ohne die mannigfaltigen Kochkünste meiner Schwester, Joo Hee, hätte ich die letzten paar Monaten nicht überlebt und ich danke meinem Bruder, Sung Hyuk, dass er nie aufhörte, auf mich stolz zu

---

---

sein. Meine deutschen Großeltern, Ruth Dietz, Otto Dietz und Oma Uschi Kastalio, kann ich auch nicht vergessen zu erwähnen, die mit ihrer Liebe und Ermutigung mein Leben noch mehr bereicherten.

Mein aller letzter, aber größter Dank geht an meinen himmlischen Vater, meinen Gott, der durch sein Versprechen, Gnade, Weisheit und Ermutigung mich trotz meiner Schwäche auf Seinem Weg hielt und bis zum Ziel führte. So wie Er versprach, bin ich jetzt (hoffentlich) bereit und kompetent genug, „dem König richtig dienen zu können“ (Daniel 1,5b).

*Soli Deo Gloria!*



---

## Lebenslauf

---

### Persönliche Daten

---

Name: Bo Ram Lee

Geburstag: 25.07.1986 in Seoul, Korea

Nationalität: deutsch

Familienstand: ledig

---

### Ausbildung

---

11.2012-12.2015 Promotion an der Technischen Universität Darmstadt  
Stipendiatin der Darmstädter Exzellenz-Graduiertenschule  
für Energiewissenschaft und Energietechnik

10.2010-10.2012 Masterstudiengang an der Technischen Universität Darmstadt  
Masterarbeit: *Influence of meteorological effects on VLF/LF signals detected  
by the Darmstadt radio-physical station VADar*

10.2006-10.2010 Bachelorstudiengang an der Technischen Universität Darmstadt  
Bachelorarbeit: *Kalibrierung einer Thomson-Parabel zur Detektion  
der laserbeschleunigten Protonen*

09.1998-07.2006 Albert-Einstein Gymnasium, Schwalbach

---

### Auslandsaufenthalt

---

01.2014-12.2014 Visiting Graduate Researcher an der University of California, Los Angeles,  
Los Angeles, CA, USA  
*High Energy Density Plasma Physics Research Group* (Prof. Niemann)

09.2008-06.2009 Auslandsstudium an der Seoul National University, Seoul, Korea

08.2003-06.2004 Schüleraustausch in Hale High School, Hale, MI, USA

---

## Auszeichnungen

---

- 01.2015 Laser and Particle Beams Nachwuchswissenschaftlerpreis  
35th International Workshop on Physics of High Energy Density in Matter  
in Hirschegg, Österreich  
Vortrag: *Generation of magnetized collisionless shock in a large laboratory plasma*
- 02.2013 5. Darmstädter Energiekonferenz - Posterpreis  
Postervortrag: *Magnetohydrodynamic energy principle for nuclear fusion matter and the plasma of the Earth's ionosphere*
- 01.2013 Laser and Particle Beams Nachwuchswissenschaftlerpreis - Posterpreis  
33rd International Workshop on Physics of High Energy Density in Matter  
in Hirschegg, Österreich  
Postervortrag: *VLF signals influenced by meteorological effects*

---

## Workshops

---

- 06.-13.09.2015 4th International Facility for Antiproton and Ion Research (FAIR)  
Summerschool in Castiglione della Pescaia, Italien
- 29.-30.05.2014 Mini-Course at the 41st IEEE International Conference on Plasma Science  
in Washington DC, USA  
*Low Temperature Atmospheric Pressure Plasmas: Physics, Diagnostics, and Applications*
- 27.-29.11.2013 Doktorandentagung der Darmstädter Exzellenz-Graduiertenschule  
für Energiewissenschaft und Energietechnik in Heidelberg  
*Energieversorgung der Zukunft - Neue Technologien und ihre Anwendung*
- 11.2012-10.2015 Ingenium-Kurse: Erwerbung von Soft-Skills  
*Zeitmanagement und Selbstmotivation; Effective Teaching; Selbstmarketing;  
Scientific Writing in English; Wissenschaftliches Vortragen; Führungskompetenz*

---

## Arbeitserfahrung

---

- 2013 Doktorandensprecherin der Darmstädter Exzellenz-Graduiertenschule  
für Energiewissenschaft und Energietechnik
- 2012-2013 Betreuung des Physikalischen Praktikums für Fortgeschrittene
- 2009-2010 Betreuung des Physikalischen Grundpraktikums

---

---

## Erklärung zur Dissertation

---

Hiermit versichere ich, die vorliegende Dissertation ohne Hilfe Dritter nur mit den angegebenen Quellen und Hilfsmitteln angefertigt zu haben. Alle Stellen, die aus Quellen entnommen wurden, sind als solche kenntlich gemacht. Diese Arbeit hat in gleicher oder ähnlicher Form noch keiner Prüfungsbehörde vorgelegen.

Darmstadt, den 18.12.2015

---

(Bo Ram Lee)

